THE DETECTION AND CHARACTERISATION OF EXTRASOLAR PLANETS

Christopher Leigh

A Thesis Submitted for the Degree of PhD
at the
University of St Andrews

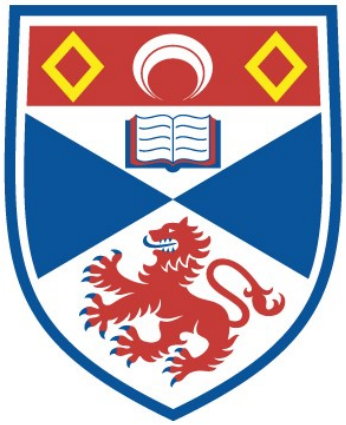

2004

THE UNIVERSITY OF ST. ANDREWS

The Detection and Characterisation of Extrasolar Planets

Christopher Leigh

Submitted for the degree of Ph.D.

December 2003

ProQuest LLC.
789 East Eisenhower Parkway
P.O. Box 1346
Ann Arbor, MI 48106 – 1346

DECLARATION

I, Christopher Jason Leigh, hereby certify that this thesis, which is approximately 40,000 words in length, has been written by me, that it is the record of work carried out by me and that it has not been submitted in any previous application for a higher degree.

Date ...1/8/04.... Signature of candidate .....

I was admitted as a research student in October 2000 and as a candidate for the degree of Ph.D. in October 2000; the higher study for which this is a record was carried out at the University of St. Andrews between 2000 and 2003.

Date ...1/8/04.... Signature of candidate .....

I hereby certify that the candidate has fulfilled the conditions of the Resolution and Regulations appropriate for the degree of Ph.D. in the University of St. Andrews and that the candidate is qualified to submit this thesis in application for that degree.

Date 19 August 2004 Signature of supervisor .....

DECLARATION

In submitting this thesis to the University of St. Andrews I understand that I am giving permission for it to be made available for use in accordance with the regulations of the University Library for the time being in force, subject to any copyright vested in the work not being affected thereby. I also understand that the title and abstract will be published, and that a copy of the work may be made and supplied to any bona fide library or research worker.

Date ...1/8/04.... Signature of candidate .....

THE UNIVERSITY OF ST. ANDREWS

The Detection and Characterisation of Extrasolar Planets

Submitted for the degree of Ph.D.

December 2003

Christopher Leigh

ABSTRACT

Since the discovery of 51 Pegasi b in 1995, continued observations have indirectly identified over 110 planetary objects. These Jupiter-mass objects cause their host star to "wobble" slightly about the common centre-of-mass of the system, which is detectable as radial motion in high-precision Doppler spectroscopy. Of the known planets, approximately 20% are found to orbit within 0.1 AU of the star, whilst the transit of HD209458 has inferred the gas-giant nature of these close-in extrasolar giant planets (CEGPs). The discovery of CEGPs has produced a wave of speculative theory as to the exact nature of these objects, and how they came to exist so close to their parent star. Our spectroscopic technique provides a method of achieving the direct detection of a CEGP atmosphere, the results of which will allow us to test emerging models that aim to predict the atmospheric nature of CEGPs and may provide additional information on the orbital inclination and mass of the planet.

We start with a historical review of the field of extrasolar planets, followed by an introduction to the fundamental concepts which underpin the reflection of starlight from a planet's surface. We then investigate the prospects of detecting such a reflection, before detailing the technique we have devised and applied here to two known CEGP hosts.

In the first instance, τ Bootis, we combined observations at the 4.2-m William Herschel telescope in 1998, 1999 and 2000. The dataset comprised 893 high-resolution échelle spectra with a total integration time of $75^{hr}32^{min}$ spanning 17 nights. We establish an upper limit on the planet's geometric albedo $p < 0.39$ (at the 99.9% significance level) at the most probable orbital inclination $i \simeq 36°$, assuming a grey albedo, a Venus-like phase function and a planetary radius $R_p = 1.2R_{Jup}$. Although a weak candidate signal appears near to the most probable radial velocity amplitude, its statistical significance is insufficient for us to claim a detection with any confidence. In the second instance, HD75289, 4 nights of VLT(UT2)/UVES observations were secured in 2003 Jan, yielding 684 high-resolution spectra with a total integration time of 26 hours. We establish an upper limit on the planet's geometric albedo $p < 0.12$ (to the 99.9% significance level) at the most probable orbital inclination $i \simeq 60°$, assuming a grey albedo, a Venus-like phase function and a planetary radius $R_p = 1.6R_{Jup}$. In both cases, we are able to rule out some combinations of the predicted planetary radius and atmospheric albedo models with high, reflective cloud decks.

ACKNOWLEDGEMENTS

There are a great many people to whom I am grateful for the past three years of my research studentship and who have had a profound and positive influence on my life. On a general level, I would like to thank my family and friends, together with staff and students in the department, and indeed in the wider university, who have made my time here in St Andrews one of the most enjoyable and productive times of my life.

On a professional level, I would firstly like to thank my supervisor, Professor Andrew Collier Cameron, for his support, guidance, patience and enthusiasm throughout the course of my research. I greatly appreciate that no matter how much work was piled in front of him, he always made time to discuss my concerns and answer my questions. I would also like to thank John Barnes for his willingness to answer the many questions fired in his direction. Sandra and I were very fortunate to share an office with such an eager and generous font of knowledge. Special thanks also go to Tim Lister who was my armour in the ever present battles against computers. Without his guidance, support and great patience, not only would there be a serious dent in both the desk and my forehead, but I highly doubt I would have been able to achieve what I have done in the time. In addition, there are a number of people in the wider astronomical community to whom I also offer thanks. For the valuable comments, contributions and suggestions towards the work presented here, I am grateful to Keith Horne, Alan Penny, David James, Tristan Guillot, Stephane Udry, Jean-François Donati and David Charbonneau.

On a personal level, I would like to thank John and Sandra for being such wonderful officemates. I will forever remember the fun and laughter, the friendly banter, the interesting aromas, the lessons on how not to grow plants, the practical demonstrations of projectile motion, but most of all for their kindness and support. I also thank Toni for her cheery visits and for numerous chats over a cup of Earl Grey.

Finally, I would like to pay tribute to the three most important people in my life. To my parents, I am truly thankful for the moral, financial and emotional support you have provided throughout my life. I am especially grateful for a carefree and happy childhood, and in your support for my decision to leave a secure career to follow my dreams. To Jenny, I am much indebted for your love, friendship and support over the course of my research, and I eagerly look forward to facing our futures together.

CONTENTS

LIST OF FIGURES

LIST OF TABLES

CHAPTER 1

Introduction

1.1 Introduction

The concept that worlds exist, other than our own, is not a new one. The ancient Greeks mooted the idea of other worlds in the context of their philosophy on an infinite Universe. Indeed, well into the 20th century, the reality of extrasolar planets existed only in the minds of philosophers and theoreticians. It was only in the final decade of the last century that technology had advanced sufficiently to allow the detection of these distant worlds. We now live in an exciting and dynamic age of discovery, where information from the stars will help us to refine theories about the formation of our own solar system and may lead to our ultimate goal of discovering a terrestrial planet, much like our own, capable of sustaining life.

In the remainder of this chapter, we set the stage for the work that follows. Chapter 1.2 details some of the more significant events in the search for extrasolar planets from their conception to their discovery and beyond. In Chapter 1.3, we summarise the modern view for the formation of stars and planets, whilst Chapter 1.4 discusses the many detection techniques currently being employed in the ongoing planet searches.

1.2 A review of the history of extrasolar planets

The first person accredited with the concept of "other worlds" is thought to be Anaximander of Miletus (c. 610-546 BC), who talked about the boundless nature of the heavens and the worlds within them. Anaximander was a student of Thales, who is considered to be

the first true astronomer, and taught that the stars and the Earth were composed of the same material. The Greeks believed that the Universe was infinite, an idea which influenced many of their early thoughts about its nature. When the famous Greek philosopher Epicurus (c. 341-271 BC) wrote of his ideas, it was based on this notion. In a letter he wrote;

> *" There is an infinite number of worlds, some like this world, others unlike it. For the atoms being infinite in number are borne ever further in their course. For the atoms out of which a world might arise, or by which a world might be formed, have not all been expended on one world or a finite number of worlds, whether like or unlike this one. Hence there will be nothing to hinder an infinity of worlds."*

In later years, however, there came a shift towards Aristotle's (c. 384-322 BC) vision of a geocentric solar system. These ideas were embodied in the writings of St. Thomas Aquinas, which became the foundation of Church doctrine and university teaching during medieval times, stifling debate on the issue for many centuries. Indeed, daring to argue against the doctrine of the Church was generally punishable by death, as was the case for Fillipo Bruno (c. 1548 - 1600 AD) of Naples who was burnt at the stake, in part due to his work "On the Infinite Universe and Worlds" in which he wrote;

> *" Innumerable suns exist; innumerable earths revolve around these suns in a manner similar to the way the planets revolve around our sun. Living beings inhabit these worlds."*

However, Bruno lived in an age of monumental change following the publication, by Copernicus in 1543, of a book entitled "On the Revolutions of the Celestial Orbs", in which he set out the case for a heliocentric system. This work, together with the discovery by Galileo Galilei (c. 1564-1642 AD) of moons around Jupiter, led to a fundamental shift back to the ideas of earth existing within an infinite Universe. It is said that this shift heralded the birth of modern astronomy and led in part to the foundation of the physical laws of Johannes Kepler (1571-1630) and Isaac Newton (1642-1727), which we still use to this day.

In 1686, Bernard de Fontenelle published his book "Conversations on the Plurality of the Worlds" in which he used the scientific knowledge of the time to put forward his view that other planets orbited other stars. Immanuel Kant, in his 1781 book "The Critique of Pure Reason" expressed his philosophical viewpoint on the habitation of other worlds by stating;

" I should not hesitate to stake my all on the truth of the proposition - if there were any possibility of bringing it to the test of experience - that at least some of the other planets which we see are inhabited. Hence I say that I have not merely the opinion, but the strong belief that there are inhabitants in other worlds."

Without any real chance of detecting extrasolar planets, hereafter ESPs, the best the astronomers of the time could do was to express their philosophical views on the existence or otherwise of other worlds. It was not until the 20th Century, with the continuing advances in astronomical instrumentation, that this expression of belief gradually moved into the scientific arena.

The first reports for the detection of an ESP came in the 1930s and 1940s, from observers using astrometric methods (see Chapter 1.4.1) to determine the orbital parameters of binary star systems. On occasion, these astronomers invoked additional planetary mass objects (Reuyl & Holmberg 1943; Strand 1943) to explain the stellar motions apparent in their results. None of these detections, however, were ever confirmed, with a more likely explanation for the unusual motion resting with the self-declared uncertainties in their measurements.

One of the more notable reports of an ESP came in the mid-twentieth century when van de Kamp (1969) analysed 30 years of photographic plates to chart the proper motion of Barnard's Star. By monitoring the astrometric progress of the star he identified a slight wobble in its path. After further calculations, he concluded that the wobble was caused by a planet of around 1.6 times the mass of Jupiter in an eccentric orbit. Over the next 12 years van de Kamp refined his calculations such that, by 1982 (van de Kamp 1982), he was convinced of the presence of two planets in circular orbits around Barnard's Star with masses 0.7 and 0.5 that of Jupiter (M_{Jup}). Although many astronomers have tried to verify his work, none were ever able to confirm the detection (Gatewood & Eichhorn 1973; Harrington & Harrington 1987) with some citing discrepancies in the observational method over the years (Hershey 1973). Peter van de Kamp died in 1995 firm in his belief that the planets were genuine. However, more recent astrometric observations by Benedict et al. (1999) using the fine guiding sensors on the Hubble Space Telescope (HST), and by Kuerster et al. (2003) with high-precision radial velocity measurements on the VLT, have once again failed to obtain any detections.

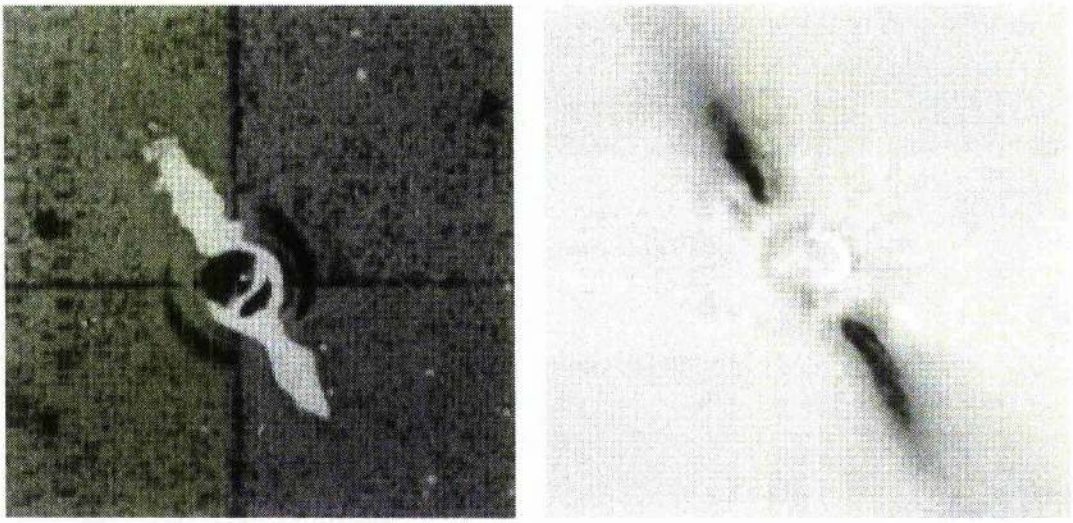

Figure 1.1: Original Smith & Terrile (1984) observations (left) and more recent VLT observations (Mouillet et al. 1997) of the circumstellar disk surrounding β Pictoris.

A fundamental step in the search for distant worlds came with the discovery by Smith & Terrile (1984) of a circumstellar disk around the nearby A5V star β Pictoris. To this point, we only had indirect evidence for the existence of ESPs, in the form of the nine solar planets. With the infrared observations of β Pictoris, shown at Fig. 1.1, we had the first unambiguous proof that flattened disks of material exist around stars other than our sun. The disk appears to be a young proto-planetary system, lending support to the standard model of solar system formation where planets emerge from a disk of dust and gas surrounding a new star.

Since stars and giant planets are thought to accrete gas in much the same way, the question arises as to the exact definition of a planet. We define a planet as an object that has formed within the circumstellar disk of its host star, however, if that object accretes enough mass then it moves into the realm of existing as a 'Brown Dwarf'. A brown dwarf is a failed star where the core temperatures and pressures were not sufficient for hydrogen thermonuclear reactions to begin. Spectroscopic observations (Geballe et al. 1996; Saumon et al. 1996b) of the famous Gliese 229 brown dwarf suggest they are very similar in nature to our own gas-giant planets, but exhibit stronger emission in the infrared through heat generated during their gravitational collapse. Therefore to distinguish between planets and brown dwarfs for the purposes of this thesis, I adopt an upper limit to the mass of an ESP at $M_p \simeq 12\ M_{Jup}$, the point at which deuterium burning within its core is predicted to become important (Milsom & Burrows 2002).

The first true discovery of an ESP came from an unexpected source in 1992, when Wolszczan & Frail (1992) announced the discovery of terrestrial mass objects orbiting the 6.2 ms pulsar PSR B1257+12. Small periodic variations ($\pm$ 3 μs) in the pulse arrival times suggested the existence of at least two planets, of mass $\sim$ 3 times that of Earth, in circular orbits with periods of 66 and 98 days. The origin of objects in such a hostile environment remains a matter of much debate, but it was not long before the significance of these discoveries was overshadowed by the emerging radial velocity searches of the early 1990s, directed towards nearby stars similar to the Sun.

The most significant discovery in the history of ESPs came with the identification by Mayor & Queloz (1995) of a Jupiter-mass object in orbit around the solar-type star 51 Pegasi. The planet was identified using radial velocity techniques, as described in Chapter 1.4.1, and found to orbit surprisingly close to its stellar host, at an orbital distance only one-tenth that of Mercury. Within weeks the discovery was confirmed by Marcy & Butler (1995) who were conducting a similar radial velocity search, but had failed to appreciate that planets might be found with such short orbital periods ($\sim$ 3.5 days). In the months following there was a burst of planetary detections (Marcy & Butler 1996; Butler & Marcy 1996; Butler et al. 1997) as groups re-analysed their datasets. The announcements have continued at a steady rate ever since, with well over 100 ESPs now known from radial velocity studies. CCPS (2003) and Schneider (2003) both maintain up-to-date catalogues of the known ESPs together with basic parameters determined by radial velocity and transit observations. Within this crop there are a number of interesting discoveries worthy of further note.

In 1997, Butler et al. (1997) announced the discovery of a planet orbiting υ Andromedae. The data revealed a planet orbiting only 0.059 AU from the host star with approximately three-quarters the mass of Jupiter. Follow-up observations (Butler et al. 1999) showed an unusual amount of scatter in the radial velocity profile, which after much investigation was attributed to the presence of two additional planets orbiting at 0.83 and 2.5 AU. The discovery suggested that planetary systems may form easily and are more commonplace than one might expect. Subsequent multiple system identifications have followed and we currently know of 13 such systems besides our own.

The next significant event represented a major step forward in our understanding of ESPs. In late 1999, the STARE transit search group started observing the G0V star

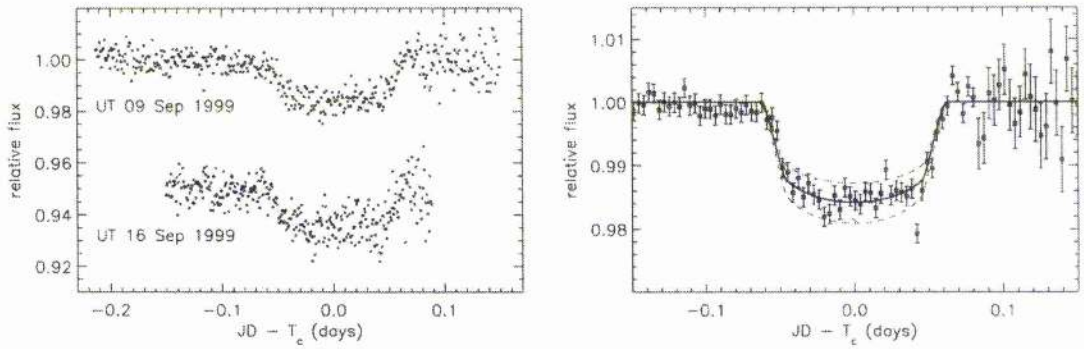

Figure 1.2: Shown (left) are the photometric time series for the Charbonneau et al. (2000) observations plotted as a function of time from the centre of tranist Tc and (right) are the data binned into 5 minute averages. The slope of the transit ingress is a function of the finite size of the planet, thus yielding an estimate of its radius.

HD209458 on the suggestion of Mazeh et al. (2000), who had recently identified a new close-orbiting 51 Pegasi type planet. On analysing their September data, the team identified a characteristic dimming of the light that co-incided exactly with the inferior transit times predicted by the radial velocity (RV) results. Charbonneau et al. (2000) formally announced their transit detection in January 2000, which was confirmed simultaneously by Henry et al. (2000b) following independent observations in November 1999. The combined RV and transit results suggested a planet of mass $M_p = 0.62\ M_{Jup}$ in an 3.52 day (0.047 AU) edge-on orbit ($i \simeq 87°$). The depth and shape of the transit suggested the intervening object had a radius $R_p \simeq 1.3\ R_{Jup}$. This larger than expected size suggested an object of lower density than Jupiter and provided the first direct evidence for the gas-giant nature of these close-orbiting ESPs, hereafter "Pegasi planets". The recent detection of a second transiting planet about the star OGLE-TR-56 by Konacki et al. (2003) reinforces this idea with a 0.9 M_{Jup}, 1.3 R_{Jup} planet in a blisteringly close 1.2 day orbit.

This is a brief review of the history of extrasolar planets, which aims to cover the majority of the important steps achieved in the field. The searches continue apace, and should unearth many more interesting discoveries on the road towards the discovery of a terrestrial earth-like planet. A target which will hopefully be realised within our lifetime.

1.3 Star and Planet Formation

In the 18th Century, German philosopher Immanuel Kant and French scientist Pierre-Simon de Laplace independently suggested that the motion of the planets in the same direction and plane could not be coincidence. They both suggested that the entire solar system formed out of a vast rotating dust cloud or 'solar nebula'. This formed the basis for the modern theory (or paradigm) for the formation of the solar system, where mutual gravitation within the nebula caused material to contract towards and accrete onto a central proto-sun. Through the gravitational contraction of gas, the proto-sun begins to heat up until eventually nuclear reactions begin, forming the new star. The slowly rotating disk of gas now has a chance to accrete, delivering material that evolves into the solar system we see today. Here we detail many ideas which contribute to the emerging consensus on the formation of planets around solar-type stars, although the picture is far from being complete with many aspects still the topic of much debate.

1.3.1 Star Formation

In the standard model of star formation, density perturbations within regions of interstellar gas and dust clouds cause the gravitational binding energy of that region to exceed its thermal energy, whereupon we see the onset of contraction (Shu, Adams & Lizano 1987; Boss 1988). The more massive stars evolve quickly and create newer and heavier elements through nucleosynthesis. These elements are subsequently dispersed into the surrounding vicinity by way of stellar outflows and supernovae. Some of the chemically enriched material remains in gaseous form, whilst some condenses into solid dust grains. Together these provide the building blocks for subsequent generations of star and planet formation.

Where the collapsing cloud possesses some initial rotation, the conservation of angular momentum requires that the gravitational collapse will lead to a flattened system, with a high proportion of binary and multiple star systems arising from the fragmentation process (Nelson et al. 1992). The formation of a single star is thought to evolve through three distinct stages, the natural consequence of which appears to be a flattened circumstellar disk.

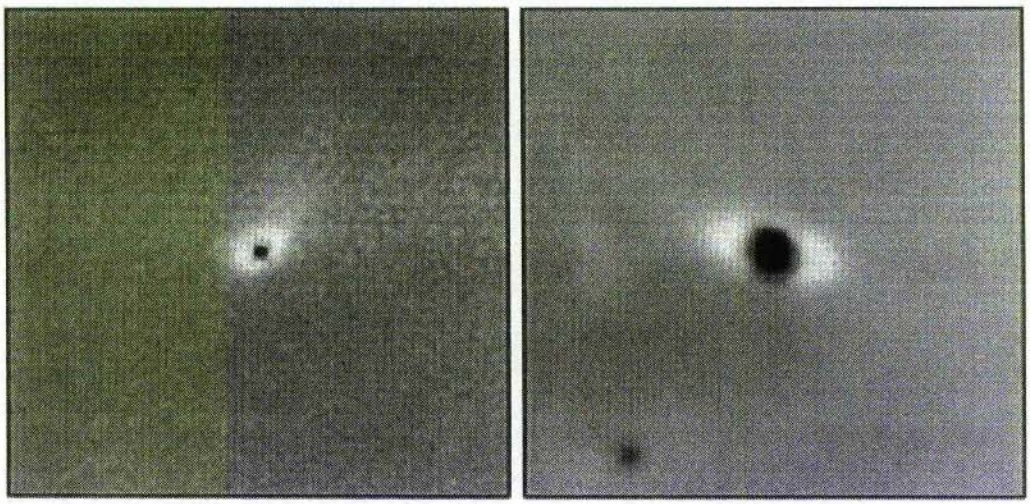

Figure 1.3: Hubble Space Telescope (HST) images of proto-planetary disks surrounding young stars in the Orion nebula, located some 450 parsecs away.

1. Collapse, under self-gravity, of an extended cloud of gas and dust composed of hydrogen and helium remaining from the early Universe, together with the debris of processed stars. This material quickly accumulates towards a central proto-star but maintains enough residual motion to prevent total inward collapse. The average angular momentum of the contracting region defines the rotation axis of the resulting circumstellar disk. After a period of about $10^5 - 10^6$ years following the onset of gravitational collapse, we see the formation of a relatively stable disk extending out to about 1000 AU. Such a circumstellar disk has been observed around β Pictoris (Fig 1.1) with more identified by McCaughrean & O'dell (1996) around a number of proto-stars within the Orion Nebula (Fig 1.3).

2. The inflow of gas and dust from the disk onto the central object by self-gravitation, compressing and thus heating the centrally condensed object until temperatures in the core of the proto-star become hot enough to trigger nucleosynthesis.

3. Through the redistribution of mass and angular momentum within the disk, a centrifugally supported stellar nebula is formed containing the material that accumulates over time to form planets. Residual gas in the nebula dissipates slowly, either by accretion onto the central star or by escaping into interstellar space with the help of stellar outflows.

1.3.2 Planet Formation

The most widely held theory on planet formation follows on directly from the star formation process, with the agglomeration of residual material to form a proto-planetary disk, as seen clearly around β Pictoris. In this view, planetary formation proceeds through several sub-stages of evolution, each involving a different form of particle interaction (Safronov 1969; Lissauer 1993; Lissauer 1995). First, dust grains within the stellar nebula settle into a dense layer in the mid-plane of the disk and begin to stick together as they collide, forming macroscopic objects with sizes of order 0.01 - 10 m. Over the following $10^4 - 10^5$ years, the second stage of evolution sees further collisions, leading to the formation of *planetesimal* objects of up to a km or so in size. Driven by gravitational interactions between each other and the parent proto-star, concentrations of objects form in particular resonant orbits with nearly empty gaps between. Subsequent stages of gravitational interaction see mutual collisions and mergers between these planetesimals and the runaway growth of the resultant planetary embryos, with terrestrial size planets forming over timescales of between 10^7 to a few times 10^8 years (Wetherill 1990). These mergers continue until the spacing of planetary orbits becomes large enough that the configuration of the system is stable in the long term.

Within the solar system, a few rocky cores in the outer parts of the proto-solar disk became massive enough ($> 15\ M_{\oplus}$, i.e. Earth masses) to slowly accrete residual H and He, thus giving rise to the gas giants. The generalised version of Jovian planet formation pictures gas accretion (Pollock 1984; Boss 1995) far from the central proto-star, where temperatures are cool enough to allow the formation of an 'ice' (water, methane and ammonia in solid or liquid form) core. Today our solar system continues to evolve in a slower and more stable manner, with meteoroids and comets thought to be the remnant planetesimals and collisional debris from a more active period in our history.

1.3.3 Planetary Dynamics

The discovery of Pegasi planets in such close proximity to their stellar hosts requires us to invoke some mechanism that allows gas-giants to form beyond the "iceline" (Boss 1995), and then 'migrate' inward to arrive in the hotter regions where they are found today. Here we detail some of the ideas put forward to explain the mechanisms behind

this orbital migration and the subsequent halt adjacent to the star.

Planet-disk interactions

Interactions between the planet and the gas disk from which it is forming, provide one of the more commonly held viewpoints on planetary migration. Initially suggested by Goldreich & Tremaine (1980) well before the discovery of 51 Pegasi b, the idea has been further extended by Lin & Papaloizou (1986); Ward & Hourigan (1989); Lin, Bodenheimer & Richardson (1996). In short, the presence of the newly forming planet within the proto-planetary disk generates spiral density waves and triggers a tidal coupling with the resulting Lindblad resonances. The planet gains angular momentum from interactions with the inner disk, whilst imparting angular momentum to the outer disk. The exchange of angular momentum leads to the possibility of the planet undergoing orbital migration if an imbalance exists between the torques exerted by the inner and outer disks. The migration that results may be described by one of two mechanisms, depending on whether the disk response is linear or non-linear (Nelson et al. 2000).

In Type I migration, smaller proto-planets ($< 15\ M_{\oplus}$) evoke a linear disk response where the outer disk torques dominate those of the inner disk and result in the rapid inward migration of the planet, independent of disk movement. Ward (1997) calculated that for 1 and 10 $M_{\oplus}$ proto-planets, initially at 5 AU, migration would occur over 10^5 and 10^4 years respectively. Proto-planet embryos large enough to precipitate the onset of gas accretion are thought to undergo Type II migration. Here the disk response becomes non-linear and a clear gap is formed around the vicinity of the planet. Provided the planet mass is less than or comparable to the local disk mass, the migration occurs on the viscous evolution time-scale of the disk (Lin & Papaloizou 1986; Trilling et al. 1998). Where the mass of the planet exceeds the local disk mass, the inertia of the planet sets the migration rate. Both Type I and Type II migration are thought to be important at different stages of the planet-formation process. For example, a small core may undergo Type I migration until it accretes enough solid material to initiate gas accretion. Type II processes then ensue with the continued formation of a gas-giant at radii closer than 4 AU (Papaloizou & Terquem 1999), possibly in situ close to the central star. Trilling et al. (1998) explored mechanisms for halting migration near the central star, such as the existence of an outward torque due to mass transfer from the planet to the star via Roche lobe overflow. They used

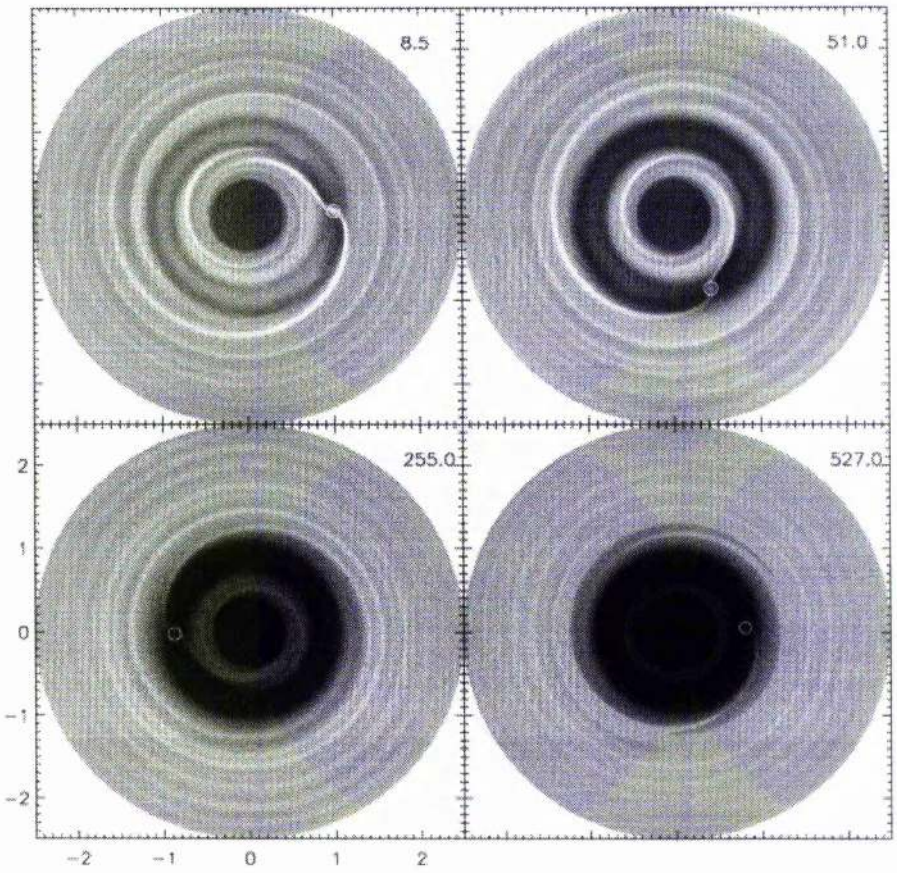

Figure 1.4: Time-sequence of Nelson et al. (2000) showing the surface density of a young circumstellar disk in which a proto-planet is forming. The circle around the proto-planet in each case has a radius equal to the Roche radius.

numerical simulations to show that Jupiter-mass planets can stably arrive and survive at small heliocentric distances.

Nelson et al. (2000) used simulations to investigate the tidal interaction between the planet and disk, with the consequent gap formation and orbital migration of the proto-planet. They found that the direction of the orbital migration is always inwards, independent of whether the proto-planet is allowed to accrete or not, such that the proto-planet reaches the central star in a near-circular orbit after a characteristic viscous time-scale of $\sim$ 104 initial orbital periods (Fig. 1.4). Inward migration is helped by the disappearance of the inner disk, and therefore the positive torque it would exert, because of accretion on to the central star. They place an upper limit on the masses of close-orbiting Pegasi planets at $\sim$ $5M_{Jup}$, assuming they originate in proto-planetary disks similar to the solar nebula.

Planet-planetesimal interactions

An alternative approach has been proposed by Murray et al. (1998), who suggest that inward migration may occur as the result of gravitational interaction with a disk of planetesimals. Resonant interactions between the planet and planetesimals act to remove angular momentum from the planetesimals. As a result, the planetesimals orbit with increased eccentricity and are subsequently ejected by or collide with the planet. The transfer of momentum works to reduce the semimajor axis of the planet, although to achieve migration over large distances by this process would require a very massive planetesimal disk ($M_{disk} > 0.3\ M_{\odot}$). Migration stops when attrition of the local planetesimal population removes the energy available to the planet. Del Popolo, Yeşilyurt & Ercan (2003) contend that large migrations in the orbital distance, due to dynamical friction with planetesimals, can be achieved with a significantly smaller disk mass, $10^{-3} M_{\odot} < M_{disk} < 10^{-1} M_{\odot}$.

Planet-planet interactions

In a system containing two Jupiter-like planets, Rasio & Ford (1996) identify the possibility that a dynamical instability may develop, which subsequently leads to the ejection of one planet while the other is left in a smaller, eccentric orbit. In extreme cases, the periastron distance of the eccentric orbit may be small enough that the planet circularises to a short-period orbit through tidal dissipation with the central star.

Stellar consumption of planets

Whilst the migration scenario is becoming more widely accepted, many astronomers believe that the halting mechanisms are too inefficient, and that many of the observed Pegasi planets are en route to being consumed by their stellar host. Trilling, Lunine & Benz (2002) modelled the evolution of giant planet orbits under the influence of disk, stellar, and mass loss torques. Although their results suggested the formation efficiency of giant planets was high, the majority migrated too fast and were destroyed via mass transfer onto the central star. Sandquist et al. (1998) investigated whether the consumption of planets could be responsible for the increased metallicity observed in the parent stars of known ESPs. From 3D hydrodynamical simulations, they concluded that the partial or total dissolution of giant planets, due to the impact of stellar matter, can result in significant enhance-

ments in the metallicity of host stars with masses in the range $1.0M_{\odot} < M_{*} < 1.3M_{\odot}$. In later work, Sandquist et al. (2002) found that heated giant planets would be efficiently destroyed near the surface of the star. They suggest that while tidal interaction between proto-planets and their nascent disks may have led them to the proximity of their host stars, post-formation star-planet interaction can lead to orbital decay or the tidal disruption of the planet, and subsequent accretion of its material. The stellar enrichment argument is one disputed by Hole et al. (2001), whose model was unable to reproduce the observed distribution of metallicity enhancement seen in ESP host stars.

The planet attrition scenario is one supported by Armitage et al. (2002), although they believe the stellar consumption of small terrestrial planets is likely to be more significant than that of gas-giants. It is also suggested (Armitage 2003) that the migration of giant planets through the inner orbits causes a reduction in the density of solid material (by ejection or consumption) and with it, the probability of forming terrestrial planets at radii of order $\sim$ 1 AU. As a result, terrestrial planets may exist only in a modest fraction of systems, where a single generation of massive planets formed and did not migrate significantly.

Whatever the truth behind the formation processes and dynamical interactions of ESPs, the fact remains that they do exist, and have been found to orbit incredibly close to their stellar hosts. We now turn our attention to the detail of known detections and how science has helped to shed new light on these previously unseen objects.

1.4 Methods of planet detection

In general, we can separate planetary detection methods into three broad categories, those looking for the dynamical influence of the planet on its stellar host, those looking for some form of attenuation to the photometric signal and finally those looking for anomalies in microlensing events. To date, nearly all of the planetary systems known have been detected via high-precision radial velocity observations. However, the information radial velocity studies provide on the physical properties of any particular object is limited to its minimum mass $M_p \sin i$, and the ellipticity, period and radius of its orbit. Alternative methods of detection that currently exist, or are in the process of being developed, will allow us to determine many additional properties for each system. With time they will

provide us with a much clearer picture as to the nature of these previously unseen worlds.

1.4.1 Dynamical Effects

The circular motion of a planet around its stellar host causes the star to undergo a rotational reflex motion or "wobble" about the centre-of-mass (Barycentre) of the star-planet system. This results in the periodic variation of three observable parameters, namely the radial velocity of the star, its angular or astrometric position and in the arrival time of some periodic reference signal.

Radial Velocity

Radial velocity searches use very slight shifts in the spectrum of a star to determine that it is under the influence of an orbiting planet. The technique has so far discovered the vast majority of ESPs around typical main-sequence stars, starting with the discovery of the planet around 51 Pegasi by Mayor & Queloz (1995). The reflex velocity amplitude, K_*, of a star of mass M_* due to a planetary companion of mass $M_p \sin i$ (minimum mass due to an unknown orbital inclination) is given by

$$K_* = \left(\frac{2\pi G}{P_{orb}}\right)^{1/3} \frac{M_p \sin i}{(M_p + M_*)^{2/3}} \frac{1}{(1-e^2)^{1/2}} \tag{1.1}$$

where P_{orb} is the orbital period of the planet and e its eccentricity. The effect of a typical Jovian system is in the region of $K_* \simeq 12.5$ m s^{-1}, whereas a close-in Jovian planet in a 3 day orbit results in $K_* \simeq 115$ m s^{-1}.

Many large-scale radial velocity surveys, such as the California & Carnegie (Marcy & Butler 1993) and Coralie (Queloz et al. 2000b) projects, continue to systematically monitor bright stars (typically less than 9^{th} magnitude due to signal-to-noise limitations) at accuracies close to 3 m s^{-1}. Such accuracies are achieved using a simultaneous wavelength calibration approach to superimpose high-resolution reference spectra onto the target spectrum, thereby negating the effects of instrumental shifts over the course of the observation. A Thorium (Th) spectrum is used in the case of the Coralie search, whereas the California & Carnegie team use an Iodine (I) cell. New technology enhancements, such as HARPS (Pepe et al. 2000) on the 3.6m telescope at La Silla, combines the siting of optical instrumentation within a vacuum chamber with the availability of both Th or

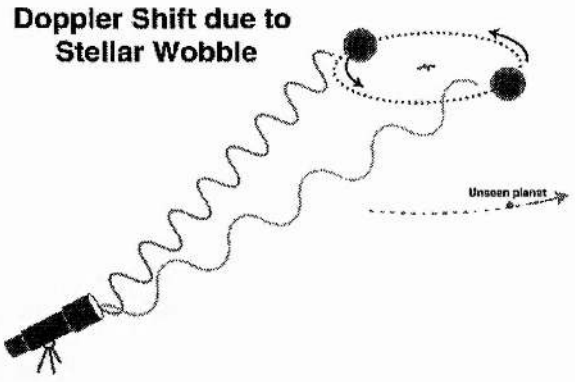

Figure 1.5: Detecting the wobble of the parent star about the barycentre.

I reference spectra, and is already yielding accuracies close to 1 m s^{-1}. As the amplitude of the radial velocity variation scales with the mass of the planetary companion, a 1 m s^{-1} precision will allow the detection of very "light" giant planets (mass a few tenths that of Saturn), although terrestrial planets will unfortunately stay beyond reach. At present there are no plans to conduct high-precision radial velocity measurements from space.

Astrometric Position

In addition to being detected radially, the barycentric motion of a star can appear as a transverse photometric displacement on the plane of the sky. Once allowances have been made for proper and parallax motion, small variations in the path traced out by the host star can be attributed to the presence of an orbiting planet, according to

$$\alpha = \frac{M_p}{M_*} . \frac{a}{d} \tag{1.2}$$

where α is the displacement in arcseconds, a the orbital distance (AU) and d is in parsecs. Jupiter viewed from a distance of 10 parsecs would result in a solar astrometric displacement amplitude of 500 microarcsecs, whilst the reflex motion of a close-in gas giant would produce signatures of no more than a few milliarcsecs. The requirement for such precise positional measurements is incredibly challenging for ground based optical observations, although current plans to construct working interferometers on the VLT and Keck telescopes within the next few years should see resolutions brought down to the 1 milliarcsec domain; an astrometric resolution comparable to that currently being achieved using the fine guiding sensors on the HST (Benedict et al. 1999). In the long term the launch of

the Space Interferometry Mission (SIM) and GAIA (ESO) will push those resolutions towards ~ 1 microarcsec, which should allow the detection of gas giants and large terrestrial planets orbiting nearby solar-type stars.

Although no confirmed detections have yet been observed using this technique, it does have the dividend that if a, d and M_* are known from spectroscopic measurements, parallax motion and spectral models, then the astrometric displacement yields M_p directly rather than $M_p \sin i$.

Event Timing

This method takes advantage of the extremely accurate radio emission frequency of millisecond pulsars to provide a reference for detecting periodic changes in pulse arrival times, due to reflex motion in the system caused by orbiting planets. Radio pulsars are rapidly spinning, highly magnetised neutron stars, formed from the collapsed cores of massive stars ($8 - 20 M_\odot$) following a supernova explosion. Due to a misalignment in their magnetic and spin axes, these objects emit intense beams of radio photons parallel to the magnetic dipole axis that, if the geometry is right, can appear as periodic radio pulses at the rotational frequency of the pulsar.

For a circular, edge-on orbit around a standard 1.35 $M_\odot$ mass pulsar, the amplitude of timing residuals due to planetary motion is given by the expression

$$\tau_p = 1.2 \left(\frac{M_p}{M_\oplus} \right) \left(\frac{P}{1\text{yr}} \right)^{2/3} \text{ms} \tag{1.3}$$

The accuracy of pulsar timing, with typical spin down rates as low as 10^{-19} s s^{-1} should theoretically allow the detection of orbiting bodies smaller than Mercury around millisecond pulsars. Indeed the first detection of an extrasolar planet is credited as that by Wolszczan & Frail (1992) around the 6.2 ms pulsar PSR 1257+12 at a distance of ~ 500 pc.

Whilst the search for habitable planets may not focus on pulsar systems, they do offer interesting ground with regard to models for the existence and stability of planets in such a hostile environment.

1.4.2 Photometric Signal

In order to obtain a direct planetary detection, we aim to employ spectral or photometric techniques to separate photons coming from the surface of the orbiting planet and those coming directly from the stellar host.

Direct Imaging

Direct imaging techniques aim to identify a resolved image of the planet as illuminated by the light from its parent star. The ratio of the brightness of the planet to that of the star depends on the planets size, its orbital phase, its inclination, and on the scattering properties of the planet's atmosphere. The exact nature of this relationship is discussed in more detail in Chapter 2.3. The technique of direct imaging suffers from two major problems:

1. The inherently small planet/star flux ratios involved (typically 10^{-9}, if we were to image Jupiter from the nearest star) make it difficult to obtain a direct image of the planet without saturation of the detector by its stellar host.
2. The small angular planet-star separations (1 arcsec for Jupiter viewed from 5 parsecs) involved suggest that in most cases the planet signal would be lost within the stellar 'seeing' profile of ground-based images, due to atmospheric refraction. Even when seeing is not a factor, most objects would still be immersed in the photon noise of a given telescopes diffraction profile ($\lambda/D \sim 0.05$ arcsecs at 500 nm for HST).

In order to successfully image ESPs directly we need to develop instrumentation and techniques which aim to achieve the following:

- Enhancment of the contrast between planet and star by (i) the use of a coronagraph or apodised aperture to mask out the light from the stellar host and (ii) conducting observations at infrared wavelengths that are more favourable to the detection of the planet's thermal emission.
- Minimisation of the effects of atmospheric turbulence by the use of adaptive optics technology with ground-based telescopes, or through conducting observations from a space-based platform.

- Improvment of the angular image resolution of the star-planet system by increasing the diameter of the observing platform or through the use of optical interferometry.

Although coronagraphic instruments such as Subaru/CIAO (Tamura et al. 2001) and on NASA's Infrared Telescope Facility (IRTF) are currently in use, recent surveys of stars with known extrasolar giant planets (Trilling et al. 2001) have failed to achieve the necessary contrast to confirm the existence of extrasolar planets. Over the next decade, we should see the launch of a number of space-based platforms, such as the DARWIN infrared space interferometer (ESO), the Jovian Planet Finder coronagraph (Clampin et al. 2001), infrared coronagraphs on the James Webb Space Telescope (successor to HST) and the Terrestrial Planet Finder optical/infrared interferometer (NASA). Such a sophisticated arsenal of observational platforms undoubtedly shows mankind's strength of commitment towards the detection of ESPs and the desire to discover worlds similar to our own. Given time we may be fortunate enough to see that commitment pay off.

Spectroscopic reflected light

Spectroscopic reflected-light searches offer an alternative method of achieving a direct planetary detection by aiming to isolate the reflected component of the stellar spectrum, Doppler-shifted due to the planet's orbital motion and modulated in phase strength. The strong dependence on the amount of light intercepted with orbital distance limits this technique to the unexpected class of close-orbiting Pegasi planets. Although we are yet to see a photometric detection, spectroscopic methods are believed to hold the key to the first direct planetary detection from the ground (Charbonneau et al. 1999; Collier Cameron et al. 1999). As this technique is the basis of this thesis, it is described in much greater detail in the course of the following chapters.

Planetary Transits

The idea of detecting companion objects through transits is not a new one, having been applied to eclipsing binary systems for many years. Given a suitable geometric alignment, the photometric signature or light-curve of the stellar host should see a characteristic dip as the planet passes in front, with the effect repeating at the orbital period of the system. For a Sun-Jupiter system at a distance of 10 pc, the resultant flux change is of the order

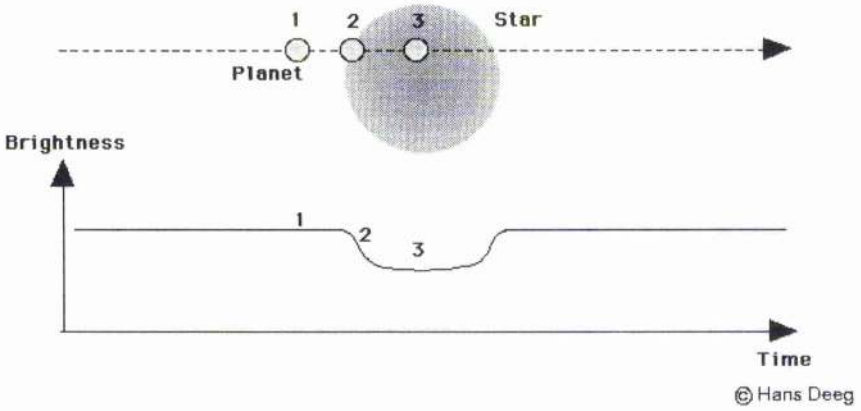

Figure 1.6: Effect of a planetary transit on the photometric lightcurve from a star.

2% or 0.02 magnitudes. However, given the large range of orbital inclinations possible and the typical planet-star separations, the chances of observing an eclipse are very small. Nevertheless, when considering large sky surveys, this method provides the most promising technique currently available for detecting planets with masses significantly below that of Jupiter.

Under the assumption of uniform surface brightness, the flux dip for the ideal geometric alignment approximates to

$$\frac{\Delta L}{L_*} = \left(\frac{R_p}{R_*}\right)^2 \tag{1.4}$$

In a more exact analysis the effects of *limb darkening* would need to be considered, which in the best case could add 25% to the flux reduction. Knowing the radius of the star from spectral classification allows us to estimate R_p, whilst prior knowledge of P_{rot} and M_* allows us to calculate the orbital radius, a, using Kepler's laws. Values of $\Delta L/L_*$ for the Earth, Mars and Jupiter transits of the Sun yield 8.4×10^{-5}, 3×10^{-5} and 1.1×10^{-2} respectively.

Over 20 transit surveys are believed to be in in current operation, including WASP (Street et al. 2003), STARE (Brown & Charbonneau 1999), EXPLORE (Mallén-Ornelas et al. 2003), VULCAN (Borucki et al. 2001) and STEPSS (Gaudi et al. 2002). Whilst these surveys have identified a number of potential targets, only one, OGLE-TR-56b, has tentatively been confirmed by radial velocity measurements (Konacki et al. 2003). At present, ground based photometry can achieve accuracies down to $\sim$ 3 millimags, thus

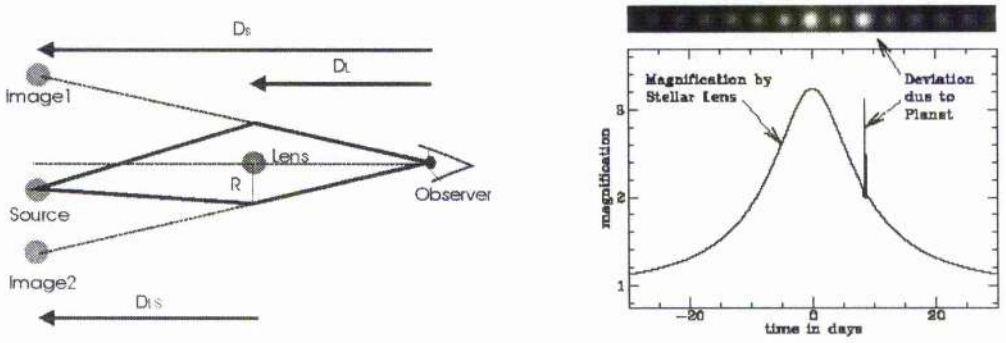

Figure 1.7: Appearence of fine Structure in a gravitational lensing event

targeting the larger gas giants. It is expected that the detection of terrestrial planet transits will only be achievable from space. Future prospects for more accurate wide-field transit surveys include the NASA Kepler Mission (Borucki et al. 1997) and ESA Eddington Project (Roxburgh, Christensen-Dalsgarrd & Favata 2000), both due for launch within the next 5 years, although some doubt has recently surfaced with regard to the latter. Both telescopes would involve a 1 m^2 collecting area with 6 and 12 square-degree fields of view respectively, observing between 40,000 and 80,000 stars over several months down to a $\Delta L/L_*$ close to 10^{-6}. Estimates for each field of observation see the detection of 480 Earth-like planets, 160 inner orbit planets and 24 outer orbit giant planets.

1.4.3 Gravitational Microlensing

In the general sense, gravitational lensing occurs where the light from a distant object is focused and thus amplified by an intervening object of some mass. The ideas surrounding gravitational lensing were first mooted by Einstein (1936) in his "General Theory of Relativity", but were confirmed more recently by the first double image observations of the distant quasar 0957+561 (Walsh, Carswell & Weymann 1979). Relative motion between the bright background source, the intervening object and the observer cause an apparent brightening and dimming of the resulting image, with changes occurring over the timescale of hours up to many days. Microlensing in the planet search sense looks for detectable fine structure in the photometric signal of the background object due to planets orbiting the lensing star (Mao & Paczynski 1991).

The fine structure or microlensing anomalies present themselves as departures from or sharp peaks within the predicted and observed smooth symmetric light curves, as shown

in Fig. 1.7. Gould & Loeb (1992) found that given the right observing strategy, the probability of finding such fine structure is about 17% for a Jupiter-like planet at 5 AU from the host star, whereas for a Saturn-like system it is about 3%. These relatively high probabilities occur where the planet appears within the *lensing zone*, a region corresponding to 0.6 - 1.6 R_E, where R_E is the *Einstein Ring Radius* given by

$$R_E = \left(\frac{4GM_L}{c^2} \frac{(D_S - D_L)D_L}{D_S} \right)^{1/2}. \tag{1.5}$$

Here M_L is the mass of the lensing object, whereas D_L and D_S are the distances to the lens and source. Fortunately these distances correspond to star-planet separations of a few AU, and hence orbital radii in the region of the habitable zone. Whilst microlensing provides a highly sensitive method of detecting planetary objects out to large distances, it does have the disadvantage that detections cannot yet be predicted for these outer planets, and once detected, will not reoccur during the same lensing event. Subsequent lensing of the same system is unlikely to occur for another $\sim 10^5$ years.

CHAPTER 2

The Nature of Extrasolar planets

2.1 Physical properties of the known planets

Our entire knowledge of planets, prior to 1990, came from studies of our own solar system and it was this knowledge which guided initial theories on planet formation. The discovery of 51 Pegasi b in 1995 (Mayor & Queloz 1995) signalled a revolution in planetary science and gave us the first indication that our system may well be atypical. The ball, set in motion 8 years ago, continues rolling to this day and has provided a wealth of information that has required us to rethink many fundamental aspects of astronomy. In this chapter we investigate what the various methods of detection tell us about the extrasolar planets and the systems they occupy. We also investigate how theory combines this information with the science of matter to generate evolutionary and atmospheric models, which may assist observers towards the next elusive step of securing a direct detection of light from one of these distant objects.

2.1.1 Results of radial velocity studies

In their most basic form, radial velocity studies look for small spectral shifts in the stellar absorption features as the host star "wobbles" about the centre-of-gravity of the star-planet system. As the results of radial velocity measurements are crucial to the reflected-light observations presented in this thesis, it is important that we detail the origin of the orbital parameters that ensue. Before doing so, we need to introduce a number of physical quantities that play a major role in the equations that follow. The radial velocity amplitudes of the star and planet are denoted by K_* and K_p, with their respective masses

referred to as M_* and M_p. By convention, M_* is given in solar units $M_\odot$ and M_p in units of Jupiter's mass M_{Jup}. The same holds for the stellar radius, R_*, and the planetary radius, R_p.

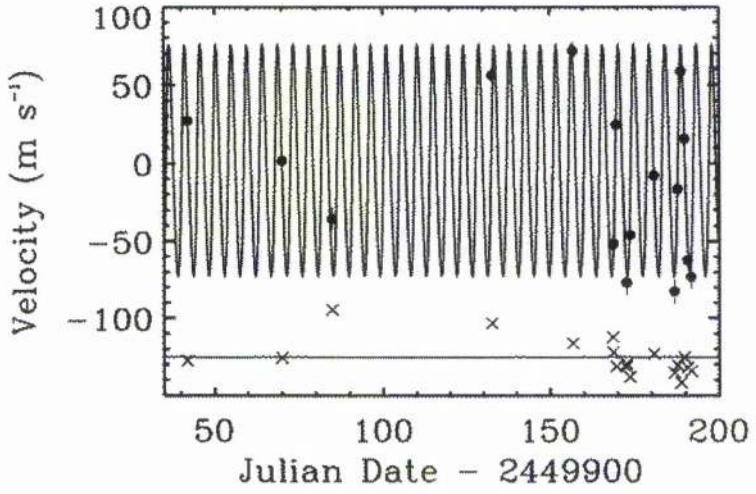

Figure 2.1: Radial velocity measurements for υ Andromedae (HR 458) secured between Aug 1995 and Jan 1996 by Butler et al. (1997). The best-fit curve (solid line) to the velocity measurements yield: $K_* = 74$ m s^{-1}, P = 4.61 days and e = 0.11.

Keplerian fits to the radial velocity (RV) observations are normally displayed in the form of a RV curve, from which K_* and the orbital period P can be determined directly. Fig. 2.1 shows the RV curve and derived parameters for υ Andromedae, as determined by Butler et al. (1997). Any significant deviation from a sinusoidal shape to the curve would indicate an elliptical component to the orbit and/or the presence of an additional gravitational influence, i.e. another star or planet. For a more detailed discussion of determining accurate fits to RV measurements, I would refer the reader to the work of groups involved in RV searches (for example see Mayor & Queloz 1995; Butler et al. 1997; Udry et al. 2000; Marcy et al. 2001). Suffice to say that correct fits to the RV profile can yield the eccentricity, e, of the orbit.

Once P is established, we can rearrange the Newtonian form of Kepler's third law to give the planet/star orbital distance a, where

$$a = \left(\frac{GM_*}{4\pi^2}\right)^{\frac{1}{3}} P^{\frac{2}{3}}, \tag{2.1}$$

and M_* is determined from the comparison of luminosity/$\log g$/$\mathrm{T_{Eff}}$ measurements to theoretical evolutionary models, or alternatively is estimated from spectral classification.

If we consider the motion of the planet about a common centre-of-mass, we can evaluate a term known as the mass function, with

$$\frac{(M_p \sin i)^3}{(M_* + M_p)^2} = \frac{P}{2\pi G} K_*^3 (1 - e^2)^{\frac{3}{2}}. \tag{2.2}$$

The $\sin i$ term arises from the inability of RV measurements to establish any component of motion normal to our line of sight. If we assume $M_p \ll M_*$, we can rearrange to yield the minimum mass of the planet,

$$M_p \sin i \simeq \left(\frac{P}{2\pi G}\right)^{\frac{1}{3}} K_* M_*^{\frac{2}{3}} (1 - e^2)^{\frac{1}{2}}, \tag{2.3}$$

where the orbital inclination i is, according to the usual convention, the angle between the orbital angular momentum vector and our line of sight. Hence, by conducting RV measurements on a star which has been found to wobble, we can identify K_*, P, e, a and $M_p \sin i$. These parameters, for each of the known extrasolar planets, are listed and regularly updated on the "Extrasolar Planets Encyclopaedia" (Schneider 2003) and "California & Carnegie Planet Search" (CCPS 2003) internet sites.

Limitations of RV searches

Although RV searches have heralded a new dawn in the domain of planetary science, there are a number of issues we need to bear in mind. The first arises from the inherently biased nature of the technique. From Eqns. 2.1 and 2.3, we find $K_* \propto M_p$ and $K_* \propto a^{-0.5}$. Thus the closer and more massive a planet, the greater the dynamical influence it has on the parent star, and the easier it is to detect. If we combine this with the efficiency at which we can secure high-quality spectra for nearby bright stars, then it is no surprise that the early planet discoveries identified relatively heavy planets in very close orbits about local neighbourhood stars.

An additional bias arises from the relatively recent introduction of RV searches. To determine the orbital parameters for a system, we need to observe a full orbit. This limits detections to planets with periods less than the amount of time observations have been conducted on a particular target. As the years pass, we should benefit not only from continued sampling of the more distant planets, but from ongoing advances in observational technology and methods. Improvements toward the 1 m s^{-1} velocity precision demonstrated by the HARPS instrument (Pepe et al. 2000), should see a significant increase in

the discovery of smaller mass planets that may have been missed by previous observations conducted using the present 3 m s^{-1} precision.

2.1.2 Results of transit detections

The fundamental result of a transit detection comes from tying the orbital plane to a near edge-on inclination. If we conduct a closer inspection of the photometric light curve (Fig. 1.2) as the planet moves across the face of the star, we can measure the time between the start of transit and the point of maximum eclipse. This allows us to establish the size of the intervening object. If we assume the star has a uniform surface brightness, then the depth of brightness drop ΔL and the stars brightness L_* are approximately related to the radii of the star and planet by

$$\frac{\Delta L}{L_*} \simeq \left(\frac{R_p}{R_*}\right)^2. \tag{2.4}$$

The exact shape of the eclipse profile depends primarily on the planet/star size ratio and stellar latitude of the transit δ, however, it is further compounded by limb darkening on the stellar surface. If the correct models are applied, and we know R_* from spectral classification, we can recover a good estimate for the planet's radius. Results for the two planets known to transit, namely HD209458b (Charbonneau et al. 2000) and OGLE-TR-56b (Konacki et al. 2003), suggest radii of 1.27 ± 0.02 R_{Jup} and 1.30 ± 0.15 R_{Jup} respectively, which, as we mentioned previously, provide strong confirmation of the gas giant nature of both Pegasi planets. If we know P and a from RV results, then an accurate record of the duration of the transit allows us to establish the latitude δ of the transit, since

$$t_{tr} = \frac{P}{\pi}\left(\frac{R_* \cos(\delta) + R_p}{a}\right). \tag{2.5}$$

This information can subsequently be used to derive the inclination of the system using simple trigonometry, since

$$\cos i = \frac{R_* \sin \delta}{a}. \tag{2.6}$$

Finally, by combining this result with Eqn. 2.3, we are able to determine the true mass of the planetary companion.

Limitations of transit searches

If we consider all possible orientations in the orbital plane of the star-planet system, there is a very low likelihood that any particular star will exhibit a transit. Borucki et al. (2001) estimate that the probability of a close-orbiting (3 to 6 day period) Pegasi planet transiting a typical dwarf star is approximately 1 in 1500. Of course, the actual chance of detection is highly dependent on the target selected and the observing strategy employed. However, given the large number of stars in our galaxy, it is highly likely that many such transits are visible. To offer the best probability of securing a transit detection, the current strategy of ground-based transit searches is to photometrically monitor tens of thousands of stars at the same time using a wide-field detector. Borucki et al. (2001) believe that, given 6 weeks to observe a typical transiting Pegasi planet, you have an 80% chance of detecting it in winter, whereas with the onset of summer, this figure drops to 65%.

As with RV searches, we find an inherent bias in transit searches towards the detection of large close-orbiting planets, for the following main reasons:

- As with HD209458b, if the orbital plane of the system is not quite edge-on, only very close objects will pass between the star and our line of sight.
- The sensitivity of ground-based transit searches is generally accurate enough to identify the 1 to 2 % photometric drop associated with the passage of Jovian size gas-giants. The detection of smaller planets is, however, likely to be much more problematic.
- If we suspect a transit, we would generally need confirmation to be sure. This is more likely to occur in the timescale of observations if the planet has a short period orbit. For Jovian-like systems, this confirmation may be many years in coming and would only then be seen again as a result of constant monitoring.
- To ensure a transit is the result of a planet, and not the glancing transit of a brown dwarf or cool companion star, we need final confirmation from RV measurements which, by their nature, are subject to the same biases.

The predisposition towards the detection of large, close-orbiting objects has so far been borne out by the gas-giant transits of HD209458 and OGLE-TR-56.

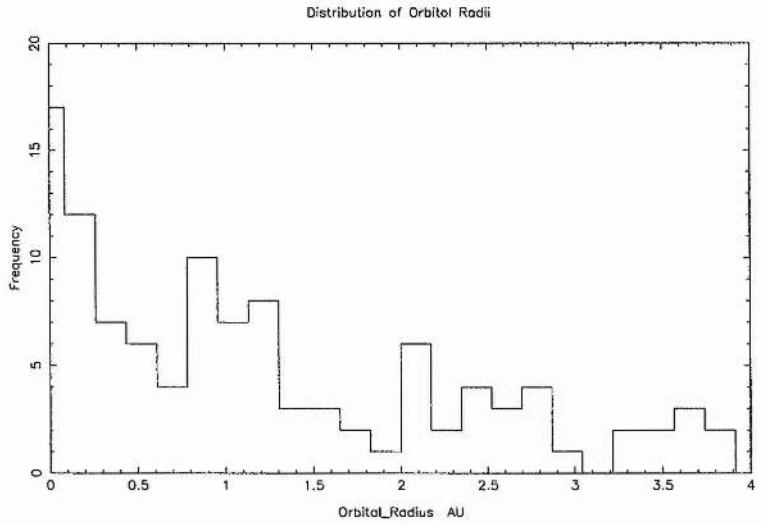

Figure 2.2: Histogram detailing the orbital distance (a) distribution, using the results of RV measurements sourced from CCPS (2003).

2.1.3 Statistical Analysis

In addition to determining their existence, radial velocity and transit studies have provided important orbital information for the known extrasolar planets, which, as of Sep 2003, number 110. The basic orbital parameters we use here, are sourced from the "Almanac of Planets" (CCPS 2003), although we omit four ESPs that are listed with a minimum mass greater than our upper mass limit of $12M_{Jup}$. In looking at the parameters, we are able to conduct a basic statistical analysis, although it is of some debate whether the size of our sample, at this time, will allow us to attach any great significance to the findings. Further caution comes, as we have seen, from the statistically biased nature of the RV/transit studies, in that they preferentially detect closer and more massive objects.

Mass, period and ellipticity histograms

If we plot the orbital distance (a) distribution in the form of a histogram, as at Fig. 2.2, we immediately see the biased nature of RV studies, and their preference for close ESPs. The peak of the minimum mass ($M_p \sin i$) distribution, as at Fig. 2.3, appears to reside close to the Jovian-mass domain, however, in not knowing the orbital inclinations of systems, one suspects that the true mass distribution would peak somewhat higher.

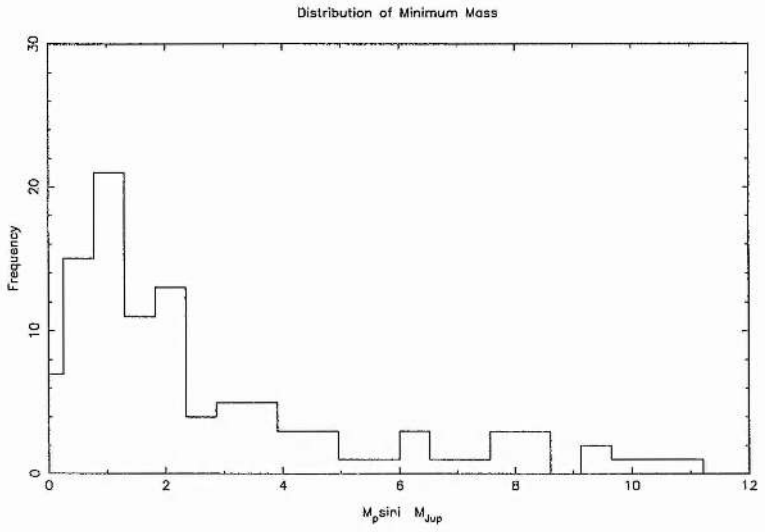

Figure 2.3: Histogram detailing the minimum mass ($M_p \sin i$) distribution, using the results of RV measurements sourced from CCPS (2003).

As the search continues, these histograms should incorporate a higher proportion of less massive planets as the accuracy of RV observations improve, and of more distant planets as longer timescale observations are able to sample their entire orbits.

Mass-period relation

An alternate statistical approach is to investigate whether any correlation exists between the different parameters attached to the systems. If we plot $M_p \sin i$ against a log scale plot of the orbital periods P, as at Fig. 2.4, we start to get the general impression that the more massive ESPs do not tend to occupy short orbital periods, i.e. close-in orbits.

It was Zucker & Mazeh (2002) who first investigated this trend, and by doing so identified a substantial deficit of massive planets with short orbital periods. They further argued that the evolution and formation of planets around host stars in binary systems was likely to differ from single-star systems, and could thus be analysed separately. In doing so, they established a positive correlation for ESPs around single-stars, as seen in Fig. 2.5, and a tentative negative correlation in the binary case, i.e. that more massive planets appear in smaller orbits. Theoretical support for their single-star correlation appears to come from a number of sources, for example -

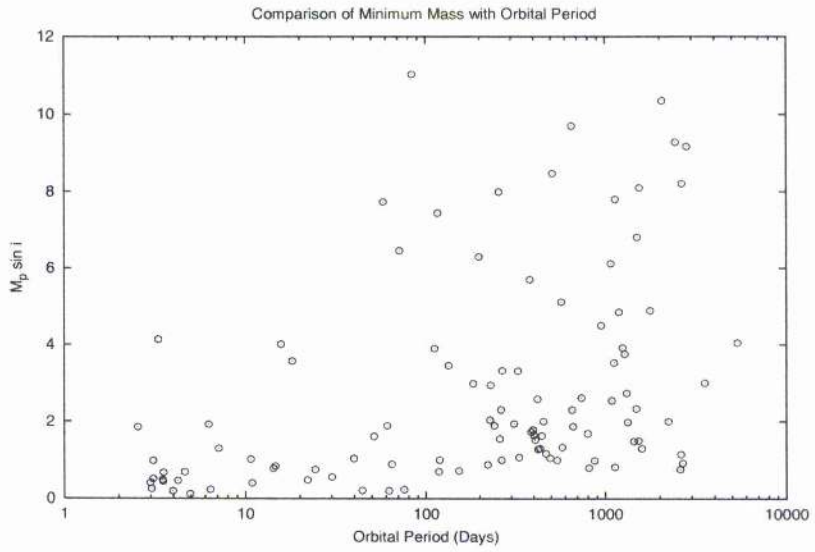

Figure 2.4: Comparison to see if any correlation exists between the minimum mass $M_p \sin i$ and orbital period P of the current ESP sample, as listed at CCPS (2003).

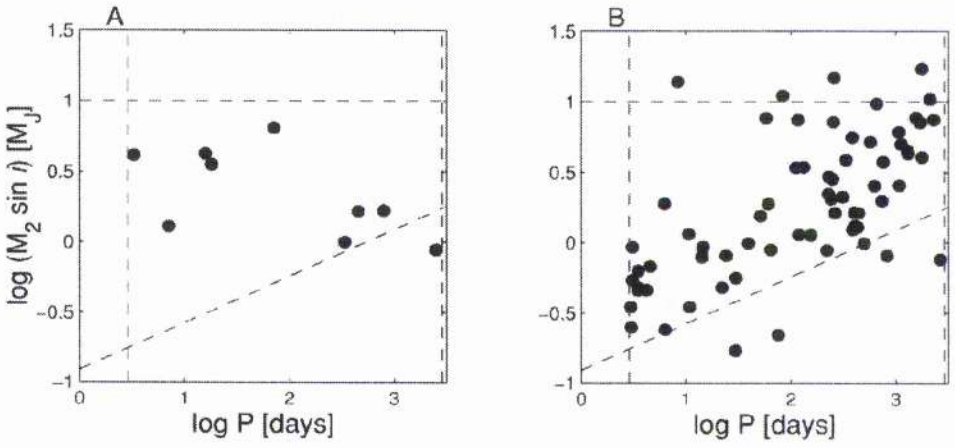

Figure 2.5: Minimum mass vs period of the extrasolar planets around (a) binary star systems and (b) non-binaries. The dashed lines here represent limits imposed and explained in more detail by Zucker & Mazeh (2002).

- On migration, the more massive planets open up gaps in the protoplanetary disks, which subsequently slow their migration rate, such that they don't tend to stray too far from their formation orbit (Ward 1997; Trilling et al. 1998; Nelson et al. 2000).
- It has been suggested (Trilling et al. 1998) that when planets get too close to their parent stars, they lose most of their mass through Roche lobe overflow.
- Migration mechanisms which invoke gravitational planet-disk (i.e. Lin, Bodenheimer & Richardson 1996), planet-planetesimal (i.e. Nelson et al. 2000) or even planet-planet (Rasio & Ford 1996) interactions to drive planets into close orbits, will be much less effective on massive planets.

Any of these explanations could easily be used to explain the apparent mass-period correlation, however, there remains some doubt as to whether the small numbers involved in the Zucker & Mazeh (2002) comparison can be classed as statistically significant.

Period-eccentricity relation

A brief look at the eccentricity distribution, Fig. 2.6, shows a broad range throughout most of the sample, although as Fig. 2.7 clearly demonstrates, closer planets appear to have less eccentric orbits. This would concur with the orbital circularisation experienced by short-period orbits due to tidal dissipation with the stellar host (Rasio & Ford 1996).

Spectral type and metallicity of the stellar hosts

Although it is interesting to investigate the types of stars found to host planets, we again have to caution against the potential bias of observers towards solar-type stars. The bias of our ESP host distribution toward G type stars, as seen in the histogram at Fig. 2.8, may well, in part, reflect a general desire to discover planetary systems, much like our own, and capable of supporting life. Other compounding factors include the much greater prevalence of low mass stars with, in particular, a balance being struck between the more numerous sub-solar stars and our ability to more easily analyse brighter stars. Furthermore, the relatively few spectral absorption features seen in early-type stars preclude the measurement of radial velocities to the precision required.

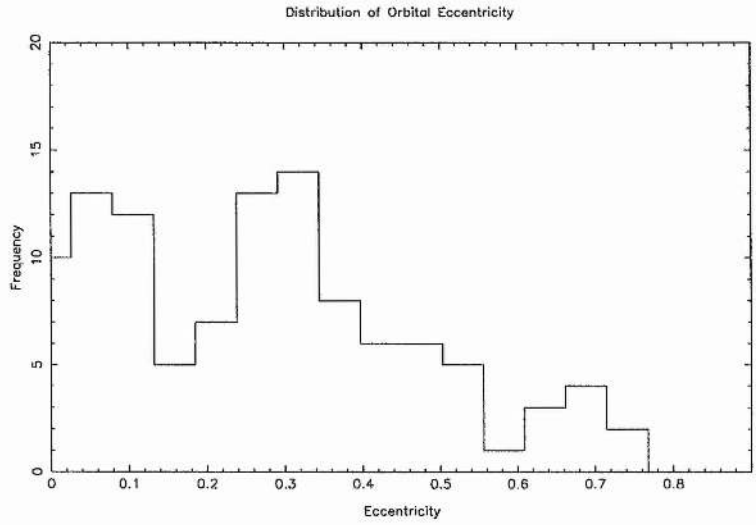

Figure 2.6: Histogram detailing the eccentricity distribution of known ESPs, as listed at CCPS (2003).

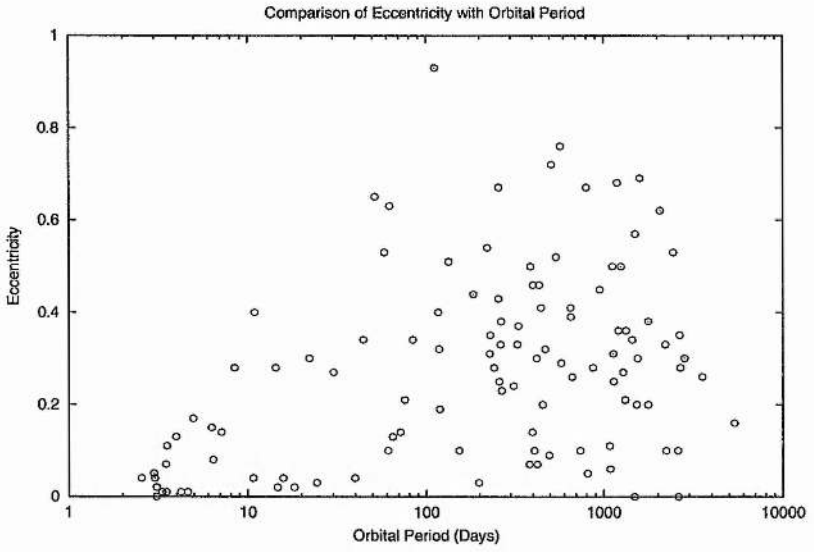

Figure 2.7: Comparison to see if any correlation exists between the orbital eccentricity and orbital period P of the current ESP sample, as listed at CCPS (2003). The log scale plot appears to show that close-in ESPs do not exhibit overly eccentric orbits.

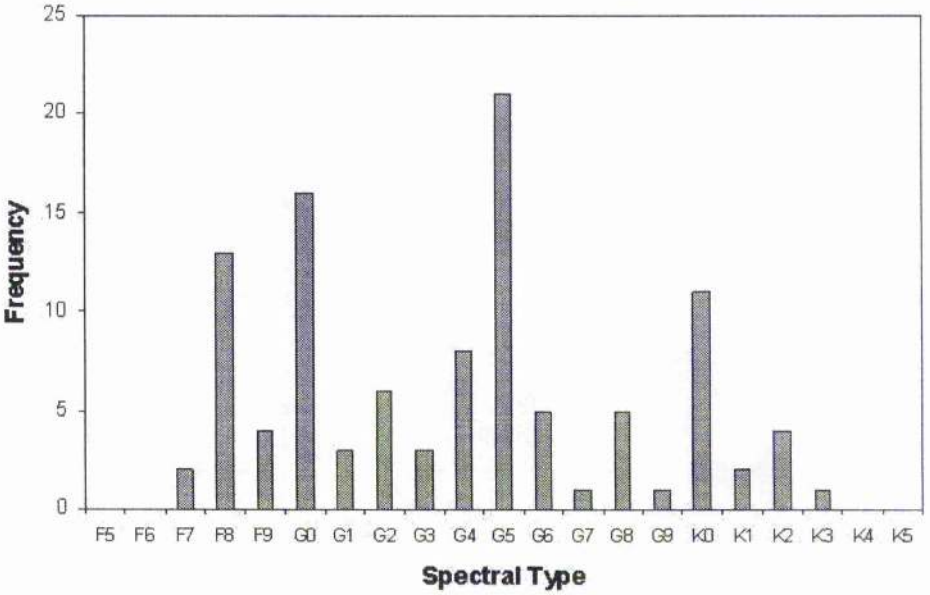

Figure 2.8: Histogram detailing the spectral type distribution for stars known to harbour companion ESPs. The data, for the 106 planets we have included in this analysis, is sourced from CCPS (2003).

Early investigations (Gonzalez 1998; Santos, Israelian & Mayor 2000; Gonzalez et al. 2001) following the discovery of ESPs, seemed to indicate that host stars were metal-rich when compared to dwarf stars in the solar neighbourhood. The discovery of a high-metallicity bias generated two main explanations. The first suggested that a high metal content in the primordial cloud, and consequently in the resulting proto-planetary disk, provided material for the rapid formation of planetesimals and subsequent larger planets. The second idea proposed that the observed metallicity "excess" was due to "pollution" of the convective envelope of the star by the infall of planets and/or planetesimals (Laughlin & Adams 1997; Gonzalez 1998; Laughlin 2000; Gonzalez et al. 2001). Alternative pollution mechanisms invoked have included the transfer of material from the disk as a result of planetary migration (Goldreich & Tremaine 1980; Lin, Bodenheimer & Richardson 1996), and the break-up and subsequent infall of close-orbiting planets due to gravitational interactions with other companions (Rasio & Ford 1996).

In the early years, comparisons involved small numbers of ESPs and any available metallicity studies of dwarf-stars, which were generally sampled from unrelated regions.

Concerned that such comparisons could introduce a bias, Santos, Israelian & Mayor (2001) conducted the first spectroscopic study of stars in a volume-limited region, in addition to 43 known ESPs. Their results, Fig. 2.9, confirmed that stars with planets are substantially metal-rich when compared to lone dwarf stars. The correlation is further strengthened when restricting the comparison to stars located within the same volume sample.

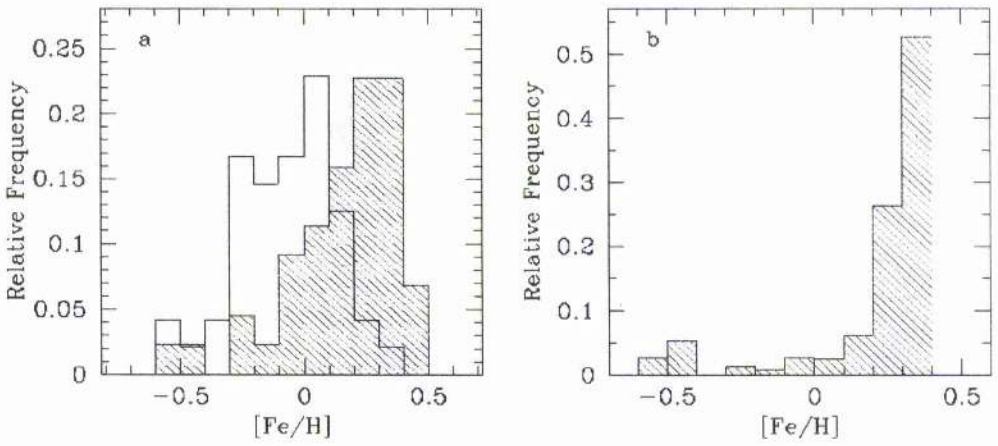

Figure 2.9: Metallicity distribution (a) of known stars with planets (filled histogram) compared to the distribution for a volume-limited sample of field dwarf-stars (empty histogram), and (b) stars with planets found only within the volume-limited sample.

In more recent work, Fischer & Valenti (2003) have investigated the iron content, relative to the Sun, of 754 solar-type stars in the local neighbourhood. Radial velocity measurements were subsequently carried out to confirm that 61 of these indicated the presence of a planetary companion. By comparing the two groups (Fig. 2.10), they have clearly established a direct correlation between the iron content of a star and its likelihood of hosting a planet. Their results show that solar-type stars, whose metal content is typical of neighbourhood stars, have a 5 to 10 percent chance of having a detectable planet, whereas stars with 3 times the solar metallicity have a 20 percent chance. Crucially, they found that the 29 most metal-poor stars in the sample, all with less than 1/3 of the Sun's metal abundance, had no planets.

It has been demonstrated (see Santos, Israelian & Mayor 2000) that the abundance of iron in the outer layers of a star bears a strong relation to the abundance of many other elements - from nickel to silicon. With such varied chemical compositions, the question arises as to whether orbiting planets exhibit similar chemical abundances to their stellar

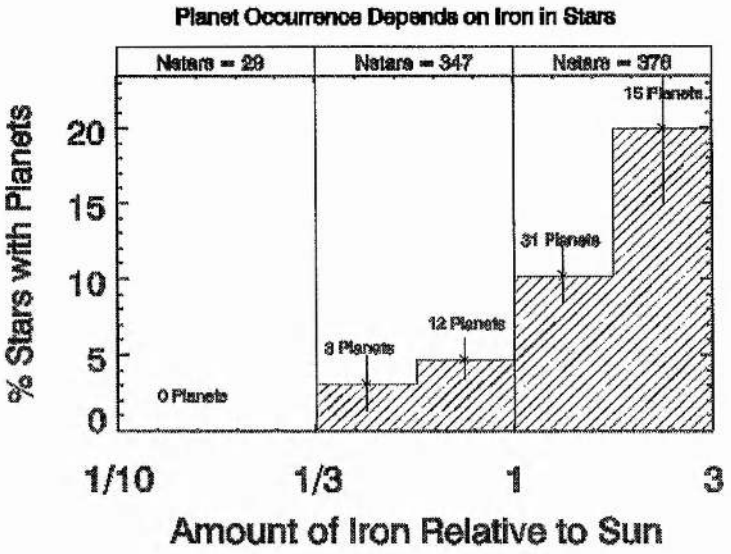

Figure 2.10: The percentage of stars with planets in relation to the iron abundance, relative to the Sun. The sample of 754 solar-type stars show a clear correlation, with stars of higher iron content being more likely to harbour planets.

hosts. We know from the measurements of HD209458b and our knowledge of Jupiter and Saturn, that gas-giants are primarily made of hydrogen (H) and helium (He); elements we would expect to occur in roughly the same proportions as in HD209458. Although we may assume the same to be true for additional metallicity, the case of our own solar system shows that metals heavier than H/He are an order of magnitude more prevalent in Jupiter and Saturn, than they are in the Sun (Saumon et al. 1996a), albeit concentrated towards their centre. This is a further indication that the atmospheres of ESPs may require an altogether different approach than has been applied to the formation and characteristics of brown-dwarf and low-mass stars.

2.2 Planetary Atmospheres

The atmospheric nature of ESPs is one characteristic that RV and transit studies are poorly placed to address, but it is of crucial importance in our attempts to detect starlight reflected from a planet's surface. The theoretical study of planetary atmospheres started well before the discovery of 51 Pegasi b. Early work investigated evolutionary models for Jupiter and Saturn (Graboske et al. 1975; Hubbard 1977), whereas Grossman & Graboske

(1973) and Black (1980) approached the issue from their studies of low-mass brown dwarf evolution. It was Burrows et al. (1995) and then Saumon et al. (1996a) who first extended this knowledge to present a suite of models for extrasolar giant planets (EGPs), ranging in mass from 0.3 - 12 M_{Jup}. As here, they adopted 12 M_{Jup} as an upper limit to the mass of a planet, as it represents the point at which core temperatures and pressures become high enough for deuterium fusion to begin. Although these early models assumed simple physical relations and wavelength dependencies, they did represent an initial salvo into what has turned out to be an intriguing and complex field. Over the intervening eight years, theoreticians have continued to modify and enhance their models, giving a clearer but generalised idea of what we may expect to find, although true confirmation of the atmospheric properties of EGPs will only come with direct observation.

2.2.1 Evolution and Radius

Soon after submission of the Saumon et al. (1996a) work, came the landmark discovery of the Jupiter mass planet, 51 Pegasi b (Mayor & Queloz 1995), in an orbit surprisingly close to its stellar host (< 0.05 AU). Although they were careful not to rule out a giant terrestrial planet, Guillot et al. (1996) argued, contrary to conventional wisdom (Boss 1995), that gas giant planets could survive in such close proximity, although it required their formation beyond the ice point, and subsequent mechanisms for spiralling into and then halting at their current orbit (Lin, Bodenheimer & Richardson 1996).

Previous theory (Saumon et al. 1996a; Burrows et al. 1995) held that EGPs would have fully convective atmospheres, but Guillot et al. (1996) extended this idea to suggest that strong external heating produced by a central star would inhibit convection and result in the creation of an outer radiative zone. In devising a more sophisticated approach to atmospheric modelling, they calculated mass-radius relations for different planetary compositions (Fig. 2.11). Whilst their results restrict the radius of a terrestrial planet to $<$ 0.35 R_{Jup}, they suggest that if 51 Pegasi b were a gas giant, the stellar irradiation could maintain the planet's radius at a value 20% - 80% larger than that of Jupiter. Confirmation of this prediction came with the discovery of the transiting planet HD209458b (Charbonneau et al. 2000), with observations by Henry et al. (2000a) and Mazeh et al. (2000) putting its radius close to 1.4 R_{Jup}. Given a mass close to 0.7 M_{Jup}, HD209458b's large radius implies an atmosphere much less dense than that of Jupiter, providing indisputable

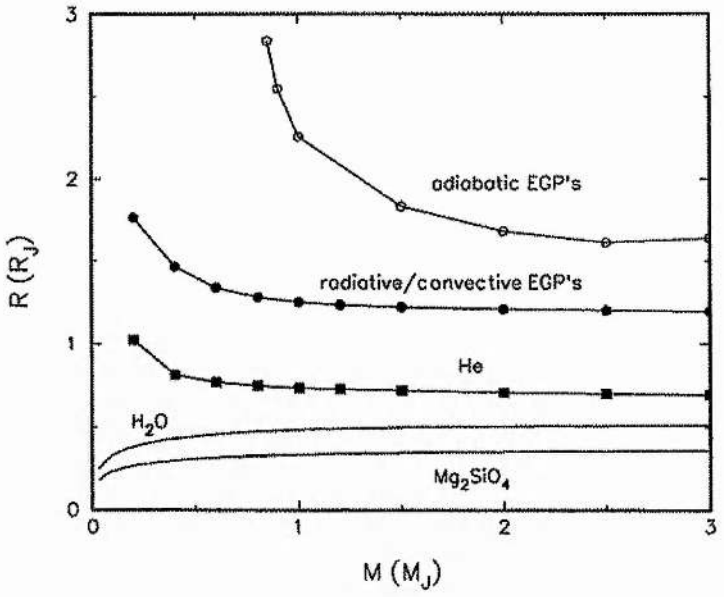

Figure 2.11: Variation of radius as a function of composition, calculated by Guillot et al. (1996) for giant planets in the mass range suggested for 51 Pegasi b by Mayor & Queloz (1995); namely 0.5 - 2.0 M_{Jup}. From top to bottom, the curves represent a fully convective gas-giant, a more realistic radiative/convective gas-giant, a pure helium radiative/convective gas-giant, a zero-temperature planet composed of pure water and a zero-temperature olivine (Mg_2SiO_4) model to represent a rocky terrestrial planet.

evidence of its gaseous nature.

Burrows et al. (2000) agreed that rather than being a result of thermal expansion in the upper atmosphere, the large radius of HD209458b was a consequence of the prevention, by stellar irradiation, of the otherwise natural cooling from the convective core of the planet. In isolation, giant planets would cool through radiation from their surfaces and shrink accordingly, in the same way brown dwarfs and protostars do via Kelvin-Helmholtz contraction. The outgoing thermal radiation (flux) would set the temperature profile through the convective core, thus controlling the rate of core entropy and radius decrease. Saumon et al. (1996a) and Burrows et al. (1997) suggest that EGPs in isolation shrink rapidly, with a 1 M_{Jup} planet reaching 2 R_{Jup} within 10^6 years. However, Burrows et al. (2000) argue that if the planet were to migrate to within 0.1 AU of its host, the resulting increase in stellar irradiation would significantly affect the temperature-pressure profile of the planet's atmosphere. In effect, the irradiation flattens the temperature profile at the outer edge of the convective region, thereby creating an outer radiative zone. This

zone acts as a barrier to the outgoing core flux, thereby reducing the rate of core entropy change (energy loss) and impairing the contraction of the planet.

This theory of EGP evolution provides a basic but logical explanation for the size of Pegasi planets, however, it was soon suggested that it wasn't quite enough to explain the observed radius of HD209458b. Bodenheimer, Lin & Mardling (2001), Guillot & Showman (2002) and Baraffe et al. (2003) argue that the large radius can only be produced by the injection of additional energy ($\sim$ 1% of incident stellar flux) into the deeper atmosphere, creating a hotter environment than was previously suggested (Goukenleuque et al. 2000). The exact origin of this additional energy remains a matter of debate, with Bodenheimer, Hubickyi & Lissauer (2000) suggesting tidal heating from orbital circularization, whilst Guillot & Showman (2002) believe stellar flux is transformed to kinetic energy within the atmosphere, which is subsequently converted to thermal energy via dynamical processes. Although the requirement for an additional energy source is not universally held (Burrows, Sudarsky & Hubbard 2003), it does highlight the potential limitations of standard evolutionary models.

In truth, we expect the atmospheric nature of EGPs, with Pegasi planets in particular, to be a highly complex function of planetary mass, composition, orbital distance and stellar type. In particular, many uncertainties remain over the exact nature and effect of clouds and dust within the atmosphere, and indeed, from our limited understanding of the underlying equations of state and opacities (Guillot 1999).

The primary aim of this thesis is the "Detection and Characterisation of Extrasolar Planets", and as such, it is useful to try and predict how incident stellar flux may interact with the atmosphere of an EGP, and whether we can use it to our advantage. Essentially, to obtain a detection we aim to observe scattered starlight from the surface/atmosphere of the planet. Since we believe that EGPs offer the best chance of securing such a detection, the remainder of this work will continue to focus on the characteristics of these Jovian-like planets.

2.2.2 Composition and Albedo Spectra

In EGPs, it is the composition of the outer atmosphere, rather than its temperature-pressure profile, that is of primary importance when trying to model the scattering prop-

erties of a planet. The first broad study of EGP spectra was put forward by Saumon et al. (1996a), who modelled the reflected component of the spectra as a greybody (i.e. no wavelength dependence) reflection of incident blackbody radiation. However, as they themselves recognised, this basic approach overestimated the reflected flux from Jupiter by up to 2 orders of magnitude. The next step required a more accurate non-grey treatment of the problem, taking into account the chemical composition and abundances expected within the atmosphere.

The measurements of HD209458b, together with our knowledge of Jupiter and Saturn, tell us that gas-giants are primarily made of hydrogen and helium; elements we would expect to occur in roughly the same proportions as in HD209458. Although we might predict the same to be true for additional metallicity, the case of our own solar system shows that metals heavier than H/He are an order of magnitude more prevalent in Jupiter and Saturn, than they are in the Sun (Saumon et al. 1996a), albeit concentrated towards their centres.

Further progress came from Burrows et al. (1997), who modelled solar composition objects to generate thermal emission spectra for planets with effective temperatures ranging from 128 to 1200 K. Although they ignored the influence of incident starlight, they found that the flux emerging from such objects deviated significantly from that of a blackbody with the same effective temperature.

Seager & Sasselov (1998) used a detailed radiative transfer model to investigate the influence of strong irradiation on Pegasi planets of solar metallicity. Their results indicate that, in comparison to an isolated planet, strong incident radiation radically affects the temperature structure within the atmosphere. In the blue part of the spectrum (< 3930 Å), Rayleigh scattering exceeds the total emitted flux (thermal) by a few orders of magnitude and acts to exactly reflect the spectral features of the host star. The inclusion of dust to the model further increases the flux reflected in the blue. In the optical and near-infrared, they found that thermal emission would gradually take over, with typical absorption features being significantly altered by the irradiation. In a similar study, Barman, Hauschildt & Allard (2001) confirmed the importance of including the effect of strong irradiation, especially for the case of close-orbiting Pegasi planets.

The first comprehensive study of the theoretical albedo and reflection spectra of EGPs was presented by Marley, Gelino & Stephens (1999), and incorporated a more

thorough analysis of Rayleigh and Raman scattering, molecular abundances and the first examination of the effect of condensation clouds (see later). They found that the reflected spectra are primarily influenced by Rayleigh scattering, molecular absorption and atmospheric condensates. In brief, their models predict that planets reflect most efficiently shortward of about 6000 Å, where photons undergo Rayleigh scattering before being absorbed. At progressively longer wavelengths, EGPs become darker as Rayleigh scattering gives way to molecular absorption. In the presence of clouds, the planets would appear brighter in the red and infrared, however, they suggest this effect would only be significant in planets cooler than $\sim$ 400 K where water clouds could form. The smaller abundances of typical condensates in warmer planets would result in relatively low albedos.

The next stage in the development saw a recognition from Sudarsky, Burrows & Pinto (2000) that with current theory, one could easily get bogged down in generating endless model albedo spectra, based on numerous combinations of EGP masses, ages, orbital distances, elemental abundances etc. They believed that the key to establishing a general understanding of the albedo and reflection spectra of EGPs over the full range of effective temperatures, was to classify EGPs into composition classes. Because of similarities in the composition and spectra of objects within each of five broad effective temperature regimes, they thought it only natural to establish a set of representative EGP albedo classes. The Sudarsky, Burrows & Pinto (2000) models, as described in Chapter 2.2.4, offer a very robust and understandable approach to the nature of planetary atmospheres. They provide us with a useful guide to planning our observational strategy and against which we can compare the results of any data we secure.

2.2.3 Effect of Clouds

The importance of clouds within the atmosphere of an EGP, was recognised very early on (Saumon et al. 1996a). In general, models (Marley, Gelino & Stephens 1999; Sudarsky, Burrows & Pinto 2000; Sudarsky, Burrows & Hubeny 2003) suggest that atmospheric pressure (P) and temperature (T) decrease with height. If the resulting T-P drop is steep enough to cross the condensation curve of a particular molecule present within the atmosphere of the planet, then clouds will form (see Fig. 2.12). For earth, the dominant cloud-forming molecule is water, whereas typical temperatures and pressures in the upper atmospheres of Jupiter and Saturn see the existence of ammonia (NH_3) clouds. Clouds

act to reflect incident photons before they are absorbed by molecules present deep within the atmosphere. As a result of clouds, Jupiter and Saturn appear quite bright, whereas Uranus and Neptune, with relatively few clouds in their upper atmosphere, see most of the incident red light being absorbed deep in their atmospheres, hence their bluish appearence. The same is thought true of all EGPs, although the range of possible temperatures and pressures mean that the dominant molecular species in each case will be different. For example, the temperature of close-orbiting EGPs such as 51 Pegasi b, is thought to be so high that the dominant cloud-forming species will be silicates of magnesium, such as enstatite ($MgSiO_3$), or even iron (Fe). At present, the general consensus holds that atmospheres in which high-level clouds are present, of whatever chemical species, appear brighter than gaseous (cloud-free) atmospheres where most of the incident light is absorbed.

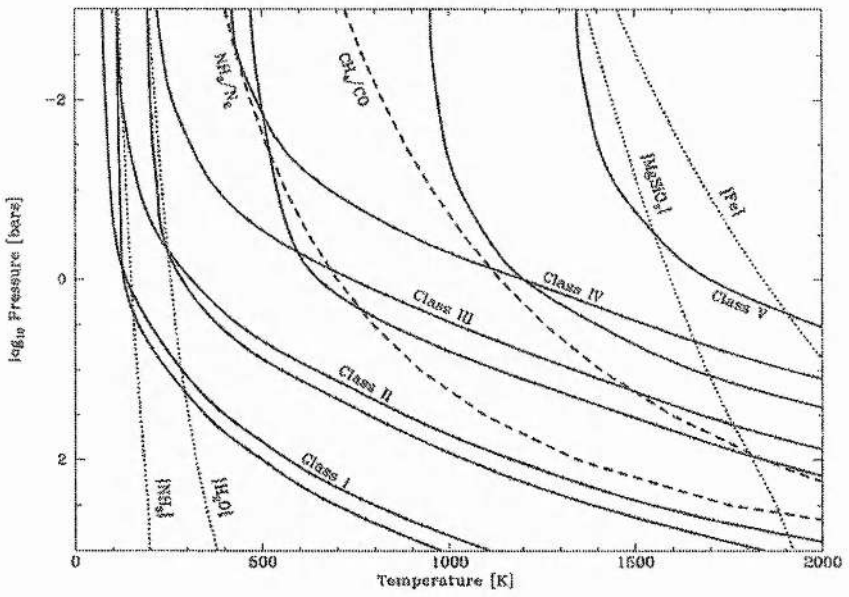

Figure 2.12: Pressure-Temperature profiles for the five EGP composition classes of Sudarsky, Burrows & Pinto (2000). Both isolated and modified (accounting for stellar irradiation) profiles are shown for classes I - IV, whereas for class V, only the modified profile is shown. Also shown (dotted) are the condensation curves for some principle condensates, together with (dashed) abudance equilibrium curves for NH_3/N_2 and CH_4/CO. Where the T-P profile crosses a condensation curve, clouds of that species are expected to form.

Barman, Hauschildt & Allard (2001), however, argue that the reverse is true. In analysing the effects of strong irradiation on cloudy and clear (gaseous) atmospheres, they find that, in the absence of dust opacity, impinging radiation significantly alters the

innermost layers of an EGP atmosphere, such that it appears brighter in the optical. For both cloud and cloud-free models, their results indicate a planet/star brightness ratio of less than 1×10^{-5}.

Whatever case holds true, the atmospheric nature of EGPs is, as we have stated, likely to be a highly complex function of many variables about which we remain uncertain. Current models are still very much in their infancy and will no doubt evolve and improve with time. In the here and now, however, we can still look to the predictions of theory to forge observational strategy and hopefully, when the time comes, to act as comparisons for future detections. In this respect, we believe that Sudarsky, Burrows & Pinto (2000) and Sudarsky, Burrows & Hubeny (2003) offer a useful set of models which can be easily adapted to these purposes.

2.2.4 Albedo and reflection spectra - Sudarsky Models

In introducing a set of EGP composition classes, Sudarsky, Burrows & Pinto (2000) sought to establish a general understanding of albedo and reflection spectra. Due to similarities in the resulting composition and spectra of their model EGPs, they decided to establish five representative albedo classes that encompassed general characteristics found in planets with atmospheres at broadly the same effective temperatures. The following represents a summary of the salient features found within the predicted albedo spectra of the five EGP classes.

Class I - Jovian class

The Jovian class I albedo spectra are found to orbit at a few AU, where effective temperatures are low ($T_{\mathrm{Eff}} < 150$ K), and are characterised by the presence of high-level (tropospheric) reflective ammonia (NH_3) clouds above molecular absorption bands of gaseous methane (CH_4). The clouds prevent most of the incoming starlight from reaching the deeper layers and so act to maintain the geometric albedo fairly high throughout most of the visible spectrum, as shown by Fig. 2.13. Rayleigh scattering is found to dominate in the very blue, but as we move towards the IR, the gaseous absorption cross-sections tend to increase, with photons more likely to be absorbed above the layers of cloud. This results in an albedo lower than that in the optical regions.

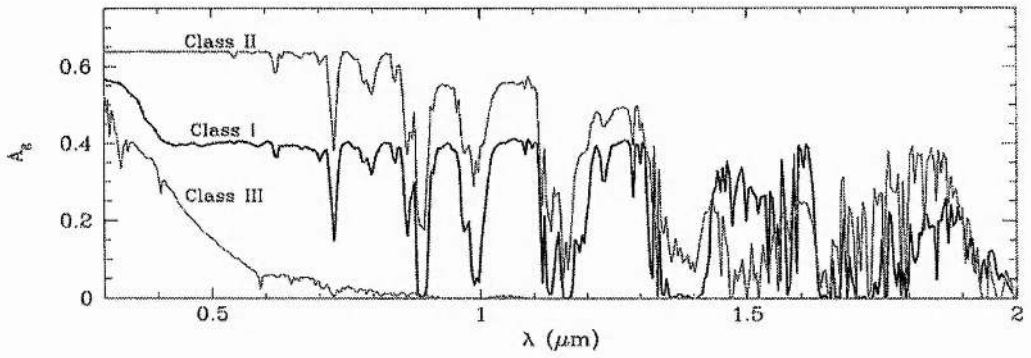

Figure 2.13: Predicted geometric albedo models for the class I, II and III EGP models of Sudarsky, Burrows & Pinto (2000).

Class II - Water class

Found to occupy slightly warmer (150 K < $T_{\rm Eff}$ < 250 K) orbits, 1 - 2 AU from their stellar hosts, class II EGPs are primarily affected by highly-reflective tropospheric layers of water (H_2O) cloud. Strong reflection throughout the visible and near-IR slowly gives way to strong absorption, dominated by H_2O, NH_3 and CH_4 features. Overall, class II objects are expected to have the highest visible albedos of any class.

Class III - Gaseous class

Orbiting at less than 1 AU, class III planets have effective temperatures of between 350 and 800 K. The lack of principal condensates in the upper atmosphere results in very strong absorption by alkali metals present in the troposphere; in particular from the sodium (Na) and potassium (K) resonance lines at $\sim$ 0.6 and 0.77 μm. Moving from the UV/blue spectral region, where Rayleigh scattering cross-sections remain large, the alkali metal absorption soon reduces the red albedo to below 0.1 (Fig. 2.13). Strong CH_4 and H_2O absorption beyond means the contribution to albedo in the near-IR is effectively negligible. Although silicate cloud layers are thought to exist very deep within the atmosphere, the upper atmosphere, where most photon interactions occur, is effectively clear or "gaseous".

Class IV - Roaster

The hot (900 K < T_{Eff} < 1500 K) or "Roaster" class of EGPs are found to orbit just 0.1 - 0.2 AU from their parent stars. Although silcate cloud decks are thought to exist at moderate levels, the abundance of alkali metals higher in the atmosphere is predicted to increase substantially. The resulting albedo spectra is expected to exhibit features predominantly of Na and K, but strongly pressure broadened where photons have been relatively unimpeded in their progress to deeper high-pressure levels. Apart from a short wavelength contribution from Rayleigh scattering, the alkali metal absorption, combined with rovibrational molecular absorption, would result in a very low albedo throughout almost the entire visible and near-infrared wavelength region (see Fig 2.14).

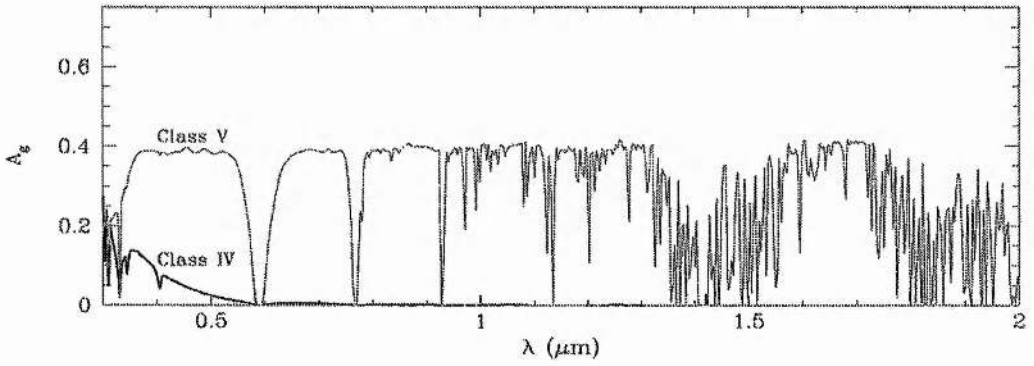

Figure 2.14: Predicted geometric albedo models for the class IV and V EGP models of Sudarsky, Burrows & Pinto (2000). Models were calculated using T-P profiles modified to include the effects of stellar irradiation from the central star.

Class V - Hot Roasters

With orbits less than 0.1 AU, the very hot (T_{Eff} > 1500 K) class V roasters (Pegasi planets) have silicate cloud decks located much higher in the atmosphere than class IV EGPS, resulting in a substantial reduction in alkali metal and molecular absorption. The presence in the outer atmosphere of Na and K, together with molecules of carbon monoxide (CO) and H_2O, generate the pattern of absorption features seen in Fig. 2.14 towards longer wavelengths. Sudarsky, Burrows & Pinto (2000) note that low mass roasters, such as HD209458b, are expected to yield significantly larger radii (Burrows et al. 2000) than similar mass objects that form in isolation. Such low surface-gravity objects see silicate

layers forming higher in the atmosphere, even when $T_{\rm Eff} < 1500$ K. In such cases, the lower $T_{\rm Eff}$ limit of a class V EGP is relaxed.

Sudarsky, Burrows & Hubeny (2003) have since updated their models, primarily to move from presenting results as albedo reflection spectra, to presenting the EGP signal contribution in terms of the total emergent flux. By effecting this change, their models now account for both the reflection of starlight, and thermal emission due to internal energy sources. Although the original Sudarsky, Burrows & Pinto (2000) composition classes remain largely intact, the analysis has shifted to include a more detailed analysis of longer wavelengths. As our analysis is designed to observe at optical wavelengths, the updated models are far less suited to our needs, thus it is the original Sudarsky, Burrows & Pinto (2000) albedo models to which we shall refer.

2.2.5 Effect of particle size

The typical size of condensate particles within EGP atmospheres add yet another dimension, which some (Seager, Whitney & Sasselov 2000; Sudarsky, Burrows & Pinto 2000; Cooper et al. 2003) believe may substantially affect the behaviour of incident starlight, and in doing so, add to the complex network of atmospheric inter-dependencies.

Seager, Whitney & Sasselov (2000) investigated the effect on Pegasi planet reflection spectra and light curves (at 5500 Å) of altering the condensate mix and size distribution, and in doing so found a very strong dependence. They suggest that clouds dominated by highly-absorbing Fe particles with sizes approaching 0.01 μm might reflect less than 1% of the incident starlight, whereas clouds containing an equal mix of $MgSiO_3$, Fe and Al_2O_3 10 μm particles act to back scatter $\sim$ 40% of the light.

In determining their composition classes, Sudarsky, Burrows & Pinto (2000) also looked at differences in the particle size distributions of principal condensates, and found that there could be large quantitative and qualitative effects on the resulting albedo spectra. In general, they found that less condensation, larger particle sizes, and wider size distributions would result in lower albedos.

More recent work by Cooper et al. (2003) has concluded that when modelling substellar mass objects, it was unrealistic to apply a single particle size distribution to an entire class of objects. Their models suggest that particle sizes vary significantly, not only

with surface gravity, but also with effective temperature. Add to this the churning effect of stellar radiation, gravitation and rotationally driven weather systems and you are looking at an atmosphere incorporating a whole assortment of different particle sizes.

2.2.6 Recent advances - Atmospheres

There is little doubt that the atmospheric modelling of EGPs has advanced over the years, however, far from painting us a clearer picture, a fair proportion of recent work has acted more to complicate the issue. It is very much akin to the early days of anatomy, in that the more one looks at the inner workings of the human body, the more difficult it becomes to understand. Here we briefly summarise some of the recent work, which continues to drive the evolution of our knowledge and understanding.

Following discovery of the HD209458b transit (Charbonneau et al. 2000), Brown et al. (2001) obtained high-quality HST transit lightcurves to both confirm, and improve on estimates for the radius, orbital inclination and mass of the planet. Charbonneau et al. (2002) used the same observations to argue that light passing through the planet's atmosphere indicates Na to be less abundant than predicted by theory (Seager, Whitney & Sasselov 2000; Brown et al. 2001; Hubbard et al. 2001). To date, a number of explanations have been put forward to explain this apparent deficiency (Charbonneau et al. 2002; Barman et al. 2002; Fortney et al. 2003). Nevertheless, this first direct evidence from the atmosphere of an EGP does highlight the limitations of current theory in an increasingly complex field.

A further complication comes in the form of atmospheric tides, first mooted by Guillot et al. (1996) but investigated in more depth by Showman & Guillot (2002). They used simple arguments to suggest that day-night temperature differences could generate strong zonal weather patterns that could wreak havoc, not only to the chemical equilibrium within the atmosphere, but also to the existence and homogeneity of cloud layers. Furthermore they argued that such strong atmospheric circulation could potentially render redundant any atmospheric predictions calculated using models that assumed homogenous conditions. Cho et al. (2003) extend this idea of circulatory patterns by suggesting that hot and cold spots (vortices) could develop, inducing spatio-temporal variability. They argue that potential observables, such as absorption levels, albedo, effective temperature, cloud presence and height etc. could differ substantially between spots, thereby producing

significant, and possibly detectable fluctuations in observable signatures.

It is perhaps a little unfair to highlight the potential failures of current theory, but we do so only to emphasise the difficulty in trying to predict the atmospheric nature of EGPs. This is a highly complex field, still very much in its infancy, with little direct evidence to go on besides what we know of our own Solar system. Theoretical predictions remain an important and useful tool, however, the best that observers can currently hope to achieve is to indentify the gross nature of an atmosphere. To that extent, theory should be seen as an interpretive, rather than a predictive tool.

2.3 The scattering of starlight

As the planet orbits its host star, some of the starlight incident upon its surface is reflected towards us, producing a detectable signature within the observed spectra of the star. This signature takes the form of faint copies of the stellar absorption lines, Doppler shifted due to the planet's orbital motion and greatly reduced in intensity ($\sim 10^{-4}$) due to the small fraction of starlight the planet intercepts and reflects back into space. Here we investigate the likely form of the signature and how the physical nature of the orbital motion should drive variations in the strength and spectral shift of the reflected starlight.

2.3.1 Photometric variations

In deriving the first fundamental equation of our analysis, we consider a host star emitting as a monochromatic light source toward a planet at opposition to us, the observer. The stellar flux incident at the surface of the planet, a distance a away, is

$$f_{inc} = \frac{L_\star}{4\pi a^2}. \tag{2.7}$$

If we assume the illuminated face of the planet will behave like a perfect Lambert disk of area πR_p^2, then the total amount of energy received and reflected as luminosity by the planet will be

$$L_p = \pi R_p^2 f_{inc}. \tag{2.8}$$

Lambert's law of reflection states that each surface element of the disk reflects the light incident upon it uniformly back into the local half-sky directly overhead. Thus the energy

is re-emitted into π steradians, with the flux from the planet received by the observer, at a distance D, given by

$$f_p = \frac{L_p}{\pi D^2} = \frac{L_\star}{4\pi D^2}(\frac{R_p}{a})^2. \tag{2.9}$$

Here we define the quantity ϵ as the ratio of flux the observer receives from the planet f_p, relative to that received from the star, f_*. Given that the stellar flux is $L_*/4\pi D^2$, we can rewrite this planet/star flux ratio as

$$\epsilon = \frac{f_p}{f_*} = \left(\frac{R_p}{a}\right)^2. \tag{2.10}$$

Of course, the reality of the situation dictates that (1) the photons are not all perfectly re-emitted, but are subject to the wavelength dependent albedo of the planet's atmosphere, and (2) the observer does not always see the fully illuminated face of the planet. Rather, they experience varying degrees of illumination, dependent on the orbital phase, in much the same way as one experiences different phases of the moon.

Geometric Albedo

The geometric albedo, denoted by p, is defined as the observed flux from the planet, seen fully illuminated, divided by the flux that would be measured from a planar Lambert law disk of the same radius, orientated normal to the direction of the stellar host, and located at the same position and distance of the planet. To first order, the value of p depends on the amplitude and angular dependence of the various scattering sources within the planet's atmosphere, integrated over the visible hemeisphere. For a Lambert law sphere, p = 0.67, whereas at 4800 Å, the geometric albedos of Jupiter, Saturn, Uranus and Neptune are 0.46, 0.39, 0.60 and 0.58 respectively (Karkoschka 1994).

In practice, the geometric albedo is likely to exhibit a strong dependence on the wavelength at which we observe, as discussed previously in Chapter 2.2.4. Such a $p(\lambda)$ dependence is seen clearly with the strikingly blue appearence of Uranus and Neptune, where atmospheric temperature, pressure and molecular abundances combine to absorb a greater proportion of red light. Whilst, our technique (see later) will be unable to determine the true albedo spectrum of a distant planet, it may be possible, given a strong detection, to assign some basic linear wavelength dependence.

Phase Function

The phase function $g(\phi)$ describes the variation in the received flux with orbital phase ϕ, and is a consequence of two competing factors. The first involves the scattering properties of particles within the atmosphere of the planet, in particular, the direction in which incident photons are preferentially scattered. Typically this depends on the size and shape of particles and not the chemical composition of the atmosphere, as is the case for the geometric albedo. The second and most significant factor relates to the varying degrees of surface illumination during the planet's orbit about the stellar host.

Where the orbital plane of a system is inclined to our line of sight, there exists an additional component to the angle of starlight reflection. To account for this we define the phase angle α, as the angle between a line joining the observer, planet and the star. α depends on the orbital inclination i and the orbital phase ϕ (measured from transit or inferior conjunction) according to

$$\cos\alpha = -\sin i \cos\phi. \tag{2.11}$$

As with $p(\lambda)$, the phase function $g(\alpha, \lambda)$ is also expected to exhibit a wavelength dependence, primarily as a result of interactions with atmospheric particles, such as Rayleigh scattering. When constructing any phase function we normalize it to $g(0, \lambda) = 1$.

It was realised early on that the orbit of a close-EGP may generate a detectable variation in the observed photometric signal. Shortly after the discovery of a planet surrounding τ Bootis (Butler et al. 1997), Baliunas et al. (1997) searched for a flux variation caused by $g(\alpha, \lambda)$. Assuming a highly reflective Jovian-like companion, they predicted a variation of ~ 0.1 millimag, however, were only able to exclude peak-to-peak amplitude changes greater than 0.4 millimag. Subsequent work by Henry et al. (2000a) further reduced this upper limit, but failed to make any detection. Future photometric satellite missions, MOST (Matthews, Kuschnig & Shkolnik 2001) and COROT (Bordé, Rouan & Léger 2003) are expected to achieve time stable precisions of ~ 10 μmags and should therefore measure the flux modulation with comparative ease. However, until the time we are able to determine planet-specific phase functions, we need a realistic alternative.

If we are to adopt a phase function there are two natural choices. The first is that of a Lambert sphere (Sobolev 1975), which assumes that the planetary atmosphere scatters

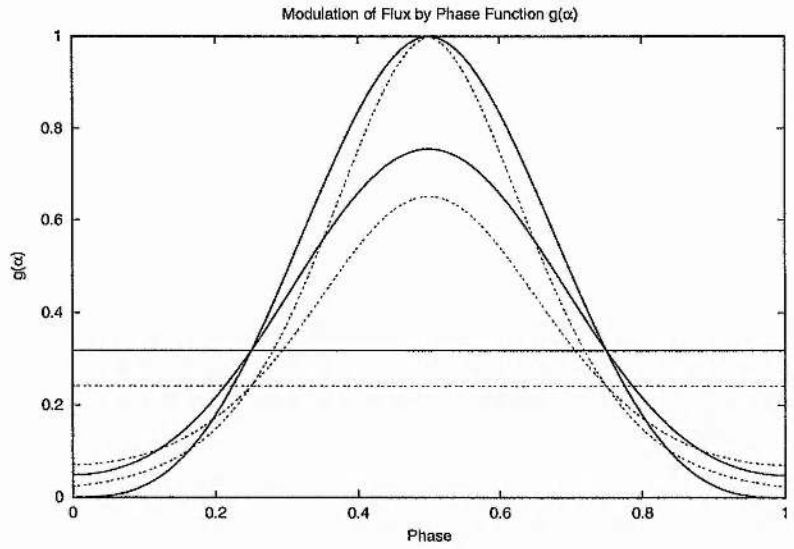

Figure 2.15: Comparisons of flux variation with orbital phase, seen in model planets which assume a Venus-like phase function (dashed) or a Lambert sphere (solid) for orbit inclinations $i = 0, 45, 90°$. In both cases, flux is measured relative to the value for illumination phase angle $\alpha = 0$. The horizontal lines show the $i = 0°$ case, while $i = 90°$ gives the greatest amplitude.

light isotropically into 2π steradians. As such,

$$g(\alpha) = (\sin\alpha + (\pi - \alpha)\cos\alpha)/\pi. \tag{2.12}$$

Observations (Harris 1961) suggest that the phase functions of gas giants in our solar system can be described as Lambert spheres to within an accuracy of 10%.

As our second option, it may be more realistic to adopt a phase function that resembles those for the cloud-covered surfaces of planets in our own solar system. Jupiter and Venus appear to have phase functions that are more strongly back-scattering than a Lambert sphere. Photometric studies of Jupiter at large phase angles from the *Pioneer* and subsequent missions have shown that the phase function for Jupiter is very similar to that of Venus (Hovenier 1989). As a plausible alternative to the Lambert sphere formulation, we can use a polynomial approximation to the empirically determined phase function for Venus (Hilton 1992). The phase-dependent correction to the planet's visual magnitude is approximated by

$$\Delta m(\alpha) = 0.09(\alpha/100°) + 2.39(\alpha/100°)^2 - 0.65(\alpha/100°)^3, \tag{2.13}$$

such that

$$g(\alpha) = 10^{-0.4\Delta m(\alpha)}. \tag{2.14}$$

Both Venus-like and Lambert sphere expressions yield phase-dependent flux correction factors, which have been plotted for comparison in Fig. 2.15.

Seager, Whitney & Sasselov (2000) presented photometric light-curve predictions for CEGPs at 5500 Å, taking into account many factors including the atmospheric density, condensates, particle size, chemical abundances and stellar irradiation. Their predictions appear to suggest that starlight may be more strongly back-scattered than inferred by either the Lambert sphere or Venus-like phase functions, being strongest within 30 degrees of the posterior transit of the planet, i.e. $0.42 < \phi < 0.58$. However, they accept that many unknowns remain that could result in substantially different photometric variations, and that the shape of any orbital light-curve will only be determined through direct observation. In that sense, they also conclude that theory should be used as an interpretive rather than a predictive tool.

First observable quantity - ϵ_o

If we incorporate the wavelength and phase dependencies of the geometric albedo $p(\lambda)$ and phase function $g(\alpha, \lambda)$, the planet/star flux ratio defined in Eqn. 2.10 becomes

$$\epsilon(\alpha, \lambda) \equiv \frac{f_p(\alpha, \lambda)}{f_*(\lambda)} = p(\lambda)g(\alpha, \lambda)\frac{R_p^2}{a^2} = \epsilon_0(\lambda)g(\alpha, \lambda). \tag{2.15}$$

Observations can measure $\epsilon(\alpha, \lambda)$ over some range of orbital phases ϕ and hence phase angles α. However, the signal-to-noise ratio (S:N) and orbital phase coverage of our observations are not yet adequate enough to define the shape of the phase function. Accordingly, current practice is to adopt a specific phase function in order to express the results in terms of the planet/star flux ratio that would be seen at phase angle zero. In doing so, we obtain our first observable quantity,

$$\epsilon_0(\lambda) = p(\lambda)\frac{R_p^2}{a^2}. \tag{2.16}$$

2.3.2 Spectroscopic variations

Our second fundamental observable results when absorption lines within the reflected component of the stellar spectrum are Doppler shifted by the orbital motion. When we

measure the radial velocity "wobble" of the host star, we find a $K_* \sin 2\pi\phi$ modulation. For a near circular orbit, the planet behaves in much the same way, i.e.

$$v_p(\phi) = K_p \sin 2\pi\phi. \tag{2.17}$$

If we consider the motion of star and planet about a common centre-of-mass, we find that their RVs are related by

$$K_p = K_*/q, \tag{2.18}$$

where the mass ratio $q = M_p/M_*$ is given by

$$\frac{q}{1+q} = \frac{K_*}{\sin i}\frac{P}{2\pi a}. \tag{2.19}$$

From this we can define our second observable quantity, namely

$$K_p = \frac{2\pi a}{P}\frac{\sin i}{(1+q)}, \tag{2.20}$$

which, as we see, retains the dependence on orbital inclination. If we know a from Eqn. 2.1 and P from RV studies, then K_p follows. As one might expect, $v_p(\phi, i)$ has a maximum radial velocity when $i = 90°$ and $\phi = \pi/2$ or $-\pi/2$. We can compare this value to the $K_{p,max}$ obtained through any detection, and thus determine the inclination of the system. Take, for example, the planet orbiting υ Andromedae. From stellar and RV parameters given at Appendices A.1 and A.2, we calculate $v_p(\pi/2, 90°) = 139$ km s^{-1}. If our analysis detects a feature orbiting at a maximum value of, say 90 km s^{-1}, then we have an orbital inclination $i = \sin^{-1} 90/139 \simeq 40°$.

In this section, we have described the observable behaviour of starlight, reflected (scattered) towards us by the atmosphere of an orbiting planet. In particular, we have introduced the two main observable quantities, ϵ_0 and K_p, which we would hope to determine from observations. In Chapter 4, we introduce the method by which these observations are secured, and the subsequent processing designed to extract the faint planet signal from observations of the stellar host. Before that, we investigate how the known stellar and planetary parameters of each system can help us to make predictions for ϵ_0 and K_p.

CHAPTER 3

Prospects for Spectroscopic Reflected-light searches

This chapter summarises the contents of a paper, authored by myself and recently published in MNRAS (Leigh et al. 2003b), presenting work carried out in conjunction with Andrew Collier Cameron and Tristan Guillot, both of whom were cited as co-authors.

3.1 Introduction

Spectral models of close-orbiting EGPs (Seager & Sasselov 1998; Marley, Gelino & Stephens 1999; Goukenleuque et al. 2000; Sudarsky, Burrows & Pinto 2000; Barman, Hauschildt & Allard 2001) show that scattered starlight dominates over thermal emission at optical wavelengths, but the albedo is very sensitive to the depth of cloud formation. Sudarsky, Burrows & Pinto (2000) find that the relatively low surface gravities of planets such as υ And b, HD75289b and HD209458b may favour the formation of relatively bright, high-altitude silicate cloud decks (cf. class V model). On higher-gravity objects such as τ Bootis b, however, the same models predict a much deeper cloud deck (cf. class IV model). In this case, much of the optical spectrum is absorbed by the resonance lines of the alkali metals. The Na I D lines in particular are strongly broadened by collisions with H_2 molecules.

In reality, however, the atmospheric structure of close-orbiting Pegasi planets is expected to be more complex, with strong winds and horizontal temperature variations (Showman & Guillot 2002), and possible temporal variations (Cho et al. 2003). The combined atmospheric circulation and temperature variations are likely to yield a disequilibrium chemical composition. Furthermore, the location and characteristics of any cloud decks cannot be predicted to any great precision with present theoretical knowledge. The next logical step towards understanding the properties and evolution of these objects will

be to test these emerging models by measuring the albedos of these Pegasi planets directly.

We found in Chapter 2.3 that a planet of radius R_p, orbiting a distance a from a star, intercepts a fraction $(R_p/2a)^2$ of the stellar luminosity. The proximity of Pegasi planets to their parent stars make them excellent prospects for reflected-light searches. At optical wavelengths, starlight scattered off the planet's atmosphere is expected to dominate over thermal emission. The planet/star flux ratio

$$\varepsilon(\alpha, \lambda) \equiv \frac{f_p(\alpha, \lambda)}{f_\star(\lambda)} = p(\lambda) \left(\frac{R_p}{a}\right)^2 g\,(\alpha, \lambda) \tag{3.1}$$

is therefore expected to vary with the star-planet-observer illumination angle α, giving a small periodic modulation to the system brightness in the form of the phase function $g(\alpha, \lambda)$. The amplitude of optical flux variability for the system is expected to be

$$\frac{\Delta f}{f} \leq 8.3 \times 10^{-5} \left(\frac{p}{0.4}\right) \left(\frac{R_p/1.4R_{Jup}}{a/0.045AU}\right)^2 \tag{3.2}$$

for a typical Pegasi planet. Future space-based photometry missions are expected to be able to detect and measure this modulation with ease. However, the orbital inclination (and hence planet's mass) cannot be determined directly from the light-curve, since the form of the phase function $g(\alpha, \lambda)$ is unknown.

Starlight reflected from a planet's atmosphere contains copies of all the thousands of photospheric stellar absorption lines, Doppler-shifted by the planet's orbital motion and modulated in strength by the phase function $g(\alpha, \lambda)$. By detecting and characterising the planetary reflected-light signature we observe the planet/star flux ratio as a function of orbital phase and wavelength. The information we aim to obtain (in order of increasing difficulty) comprises:

- K_p, the planet's projected orbital velocity, from which we obtain the orbital inclination of the system, i. This allows us to determine the planet mass M_p, since $M_p \sin i$ is known from the star's Doppler wobble.
- ϵ_0, the maximum strength of the reflected starlight that would be seen if the planet were viewed fully illuminated.
- $p(\lambda)$, the albedo spectrum, which depends on the composition and structure of the planet's atmosphere.
- $g(\alpha, \lambda)$, the phase function describing the dependence of the amount of light reflected toward the observer by the star-planet-observer angle α.

3.2 System Parameters

The known stellar parameters for six bright stars known (from Doppler wobble studies) to harbour Pegasi planets are set out in Appendix A.1. Fits to the radial velocity data have provided us with orbital periods for the planets, together with the stellar reflex velocity K_* of each star about the common centre-of-mass of the system. Both parameters are set out in Appendix A.2 alongside calculated values for the orbital radius of the system (from Kepler's Laws) and the minimum planet mass. In addition, we provide theoretical estimates for the effective temperature and upper limit on the radius of the planet (for edge-on orbits), assuming both "Hot" and "Cold/Dissipative" atmospheric structure models, as described in more detail by Showman & Guillot (2002) and summarised in Chapter 3.2.2.

3.2.1 Planetary mass estimates

Among the known Pegasi planets there are several promising candidates for future spectroscopic reflected-light searches. The main selection criteria are that the host star must be bright, and that the planet/star flux ratio near superior conjunction must be high. Given spectroscopic and/or photometric estimates of the stellar radius R_*, the projected rotation speed $v \sin i$ and rotation period P_{rot}, we estimate

$$\sin i = \frac{P_{rot}\, v \sin i}{2\pi R_*} \tag{3.3}$$

This makes the assumption that the stellar rotation axis and the orbital plane are close to perpendicular, as was determined for HD209458 by Queloz et al. (2000a). The mass ratio, $q = M_p/M_*$, follows from the observed orbital period P_{orb} and the stellar reflex velocity, K_*, with

$$\frac{q}{1+q} = \frac{K_* P_{orb}}{2\pi a \sin i} \tag{3.4}$$

This then provides us with the planet's projected orbital velocity amplitude ($K_p = K_*/q$) in addition to the planet mass ($M_p = qM_*$).

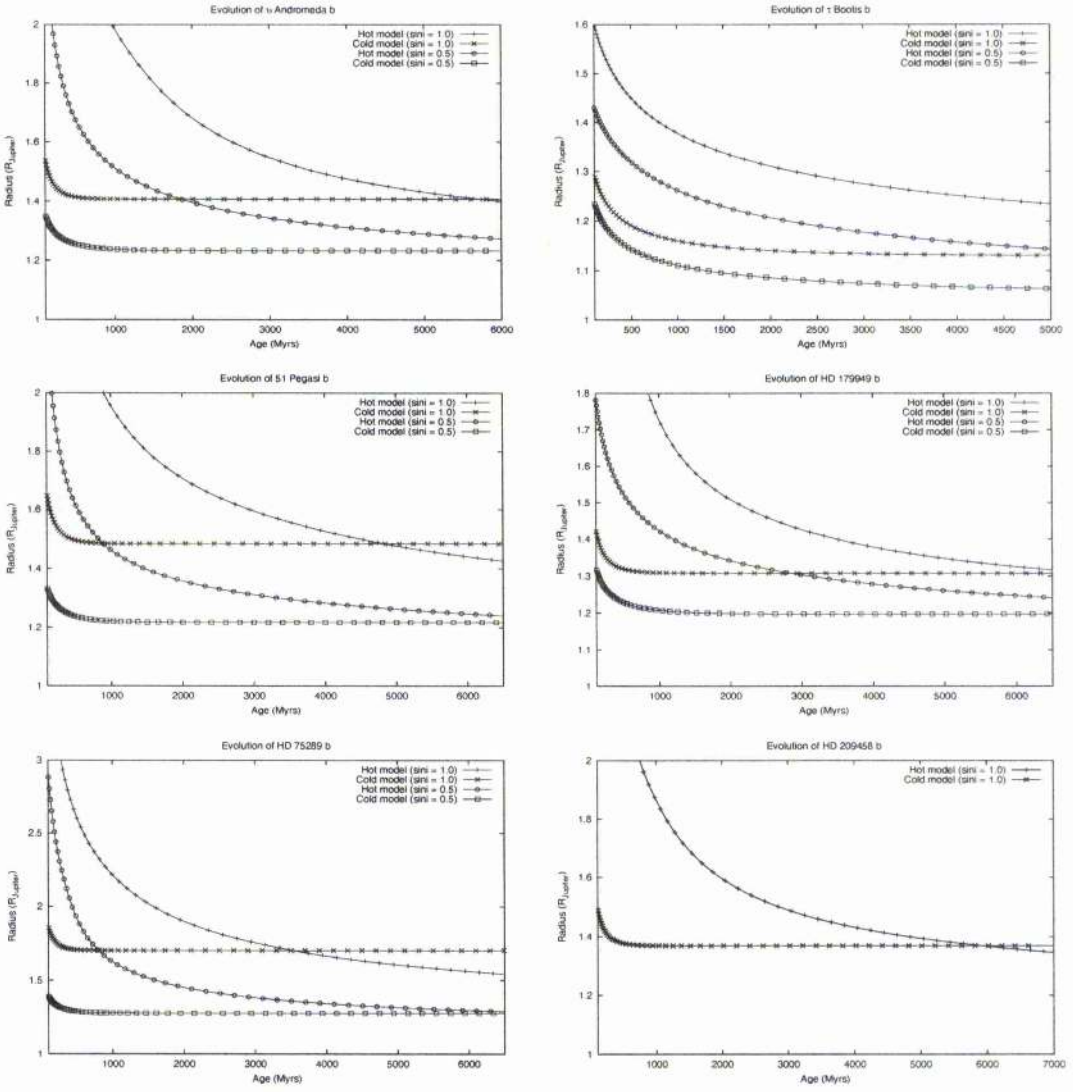

Figure 3.1: Evolutionary radius models for the planets surrounding υ And, τ Bootis, 51 Pegasi, HD179949, HD75289 and HD209458. The evolutionary tracks show the "Hot" and "Cold/Dissipative" models for orbital inclinations of $\sin i = 0.5$ and $\sin i = 1.0$. Being a known transiting planet, HD209458b is shown solely for $\sin i = 1.0$.

3.2.2 Planetary radius estimates

Assuming a known mass, the radius of a gaseous planet is governed by its Kelvin-Helmholtz contraction, and the following factors, in order of significance: (1) its composition; (2) its atmospheric temperature; (3) possible additional energy sources; and (4) its age. Uncertainties also stem from our limited understanding of the underlying physics: equations of state, opacities (see Guillot 1999).

Transit measurements of the radius of HD209458b (Charbonneau et al. 2000; Henry et al. 2000a; Brown et al. 2001) show that the planet is essentially made of hydrogen and helium (Guillot et al. 1996; Burrows et al. 2000), thus addressing the first source of uncertainty concerning the radii of Pegasi planets. However, it was later shown that the radius of HD209458b is too large to be explained by standard evolution models using realistic atmospheric boundary conditions (Bodenheimer, Lin & Mardling 2001; Guillot & Showman 2002; Baraffe et al. 2003). Instead, Bodenheimer, Lin & Mardling (2001) proposed that HD209458b may be kept inflated by the dissipation of tides through the circularization of its orbit. Due to the very small eccentricity of the orbit (consistent with 0.0), Showman & Guillot (2002) proposed two alternative explanations: either the atmosphere is relatively cold, as predicted by radiative transfer calculations, and kinetic energy generated in the atmosphere is dissipated relatively deep in the interior (e.g. by tides due to a slightly asynchronous rotation of the interior), or the atmosphere is warmer than calculated, for example because shear instabilities force it into a quasi-adiabatic state. We therefore calculate the radii of other Pegasi planets on the following basis:

- All Pegasi planets have approximately the same composition, being made mostly of hydrogen and helium.
- Their atmospheres are either "hot" or "cold", the temperature at a given level (10 bars) being calculated as a function of the effective temperature and gravity, as described in Guillot & Showman (2002), assuming a bond albedo equal to 0.4.
- In the "cold" case, an additional energy flux is deposited at the centre of the planet. This flux is set equal to 8×10^{-3} times the absorbed stellar luminosity (i.e. between 1.2 and 3.1×10^{26} erg s^{-1}). This corresponds to the energy flux necessary to reproduce the radius of HD209458b with "cold" boundary conditions (Guillot & Showman 2002).

Of course, a number of unknowns remain. Most importantly, both the composition, bond albedo and the energy flux dissipated in the planet are likely to be complex functions of the planetary mass, orbital distance and even stellar type. However, this is likely to be a second order effect because structure calculations take advantage of the known radius of HD209458b. It is interesting to see that even though the parameters of the models have been set by the constraint on HD209458b, the "hot" and "cold" scenarios shown in Fig. 3.1 yield significantly different radii for the other planets. This is due to the fact that energy dissipation (in the "cold" case) has a greater impact on planets of smaller mass, and that the "hot" boundary condition yields a planetary radius that is more sensitive to the orbital distance.

As a corollary, this shows that observations of the reflected light from these planets can provide critical information for deciding between these models.

3.2.3 Flux ratio estimates

For a Lambert-sphere phase function $g(\alpha)$ we can compute the maximum expected planet/star flux ratio near to superior conjunction,

$$(f_p/f_*)_{max} = pg(\pi/2 - i)\left(\frac{R_p}{a}\right)^2 \tag{3.5}$$

The value $p = 0.4$ assumed for the grey geometric albedo is plausible for the case of a high, reflective silicate cloud deck with little overlying absorption, as in the class V models of Sudarsky, Burrows & Pinto (2000). Other models in which cloud layers are deeper, or even absent, produce lower optical albedos; thus the flux ratios we compute here should be treated as upper limits on the plausible planet/star flux ratio.

3.3 Prior probability distributions

We derive the prior probability distributions for the observable quantities K_p and $(f_p/f_*)_{max}$ by drawing randomly from the uncertainty distributions (assumed gaussian) for the observed quantities K_*, M_*, R_*, P_{rot}, Age and $v \sin i$. The values of these quantities, for six of the brightest stars known to harbour Pegasi planets with orbital periods of less than 5 days, are given at Appendix A.1 and A.2. In order to provide a radius estimate for each planet, we use our $\sin i$ estimate to conduct a $\log R_p - \log M_p$ linear interpolation (for a

selected age) between the $\sin i = 1.0$ and $\sin i = 0.5$ evolutionary models. In each case we performed 1,000,000 random Monte Carlo trials to compute K_p and $\log(f_p/f_*)_{max}$. The resulting joint probability distributions for the planet/star flux ratio and projected orbital velocity amplitude are presented in Fig. 3.2.

The maps are calculated for an evolutionary radius model that exhibits a "Hot" atmospheric structure, although maximum likelihood values for both the "Hot" and "Cold" scenarios are shown at Table 3.1. Trials in which the orbital inclination was high enough to cross the observer's line of sight to the stellar disc were rejected for all cases bar HD209458b, since none of these other systems has been seen to exhibit transits (Henry et al. 2000a; Tinney et al. 2001). For the transiting planet, its known inclination and mass act to constrain the projected radial velocity amplitude.

In the case of τ Bootis, an additional constraint was applied. Since the rotation of the primary appears to have become synchronised with the planet's orbit (Baliunas et al. 1997; Collier Cameron et al. 1999; Henry et al. 2000a), the planet must have been massive enough to have synchronised the star's spin within its own main sequence lifetime. For each trial we computed both the main sequence lifetime and the synchronisation timescale. Trials in which the latter exceeded the former were rejected. This, in conjunction with the well determined $v \sin i$ value, leads to a fairly tight constraint on the system inclination and hence K_p.

3.4 Discussion

The maximum observable planet/star flux ratio for a planet depends strongly on the inclination of its orbit to our line of sight, and on the distance of the planet from the star. The statistical analyses presented here provide estimates of the planet/star flux ratio, derived from the best data currently available on six bright stars harbouring planets with orbital periods of less than 5 days. These estimates are model-dependent, in that we have made theoretical assumptions about each planet's radius, the inclination of each orbital plane to the stellar rotation axis and used a Lambert-sphere phase function to describe the atmospheric scattering properties. In addition, we have adopted a grey geometric albedo ($p = 0.4$) that corresponds roughly to the reflective, high-level silicate cloud decks predicted by the class V spectral models of Sudarsky, Burrows & Pinto (2000).

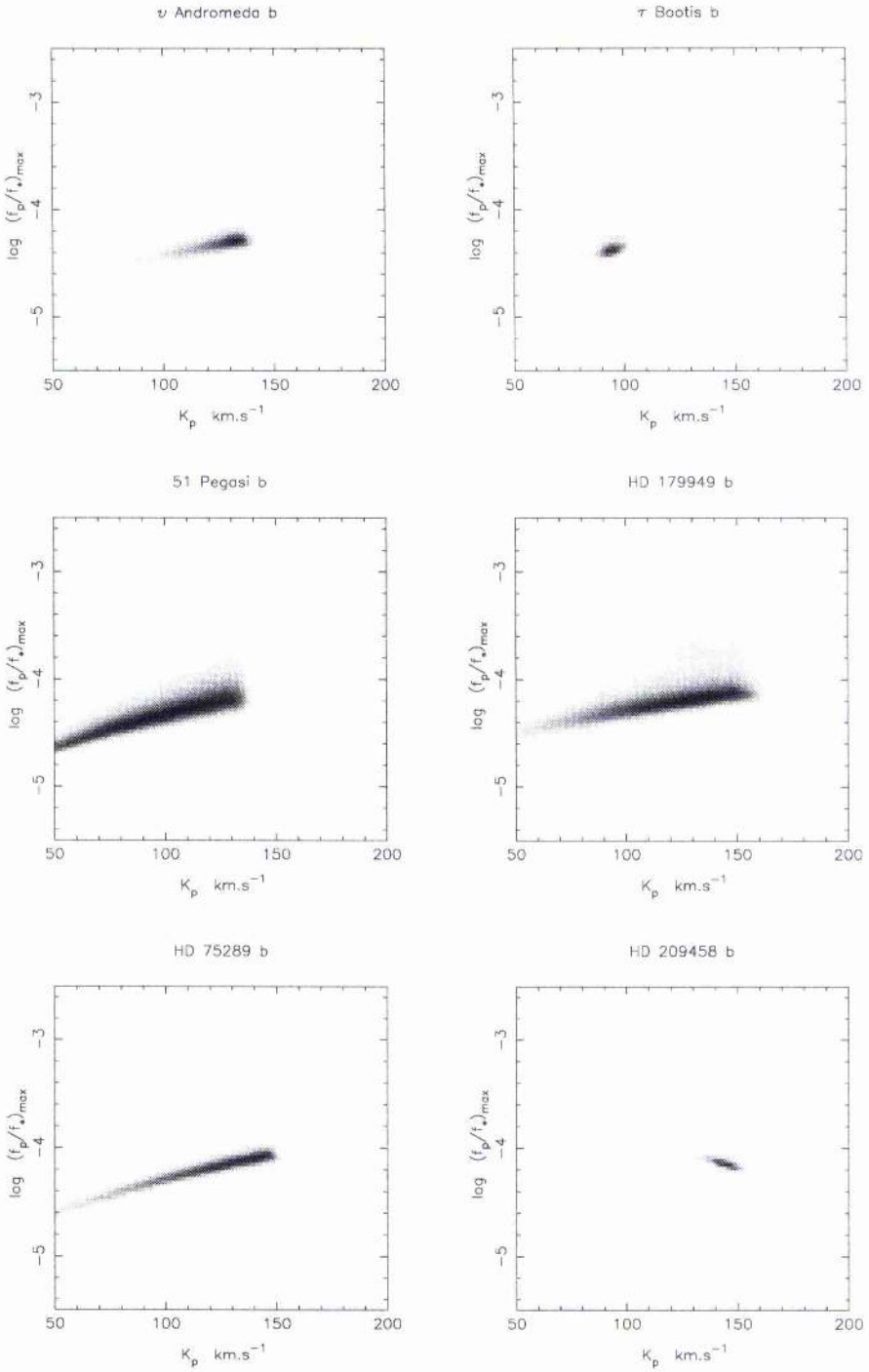

Figure 3.2: Prior probability density maps for the planet/star flux ratio near superior conjunction, as a function of the planet's projected radial velocity amplitude K_p, for an assumed geometric albedo $p = 0.4$. The maps are calculated for an evolutionary radius model that exhibits a "Hot" atmospheric structure, although maximum likelihood values for both the "Hot" and "Cold" scenarios are shown at Table 3.1.

Planet	K_p (km s^{-1})	Inclination (Degrees)	M_p/M_{Jup}	$(f_p/f_*)_{max}$ Hot model	$(f_p/f_*)_{max}$ Cold Model
υ And b	133	78	0.760	4.88 x 10^{-5}	4.53 x 10^{-5}
τ Boo b	95	37	6.813	4.18 x 10^{-5}	3.22 x 10^{-5}
51 Peg b	117	63	0.523	4.81 x 10^{-5}	4.46 x 10^{-5}
HD 179949 b	135	60	0.945	6.44 x 10^{-5}	5.34 x 10^{-5}
HD 75289 b	141	75	0.498	7.38 x 10^{-5}	9.17 x 10^{-5}
HD 209458 b	144	87	0.620	7.18 x 10^{-5}	7.17 x 10^{-5}

Table 3.1: Maximum likelihood statistics for the parameter distributions returned by the Monte Carlo trials, given what we already know about the system from observation. In adopting a grey albedo of $p = 0.4$ for our trials, similar to that of the class V models of Sudarsky, Burrows & Pinto (2000), we expect the f_p/f_* results to reflect an upper limit to the expected brightness of the planet.

Target	m_V (Mags)	$(f_p/f_*)_{max}$ Hot model ($i = 90°$)	4m-class telescopes	8m-class telescopes
υ And	4.09	4.88 x 10^{-5}	20.0 hrs	5.0 hrs
τ Boo	4.50	4.18 x 10^{-5}	39.8 hrs	9.9 hrs
51 Peg	5.46	4.81 x 10^{-5}	72.7 hrs	18.2 hrs
HD 179949	6.25	6.44 x 10^{-5}	84.0 hrs	21.0 hrs
HD 75289	6.35	7.38 x 10^{-5}	70.1 hrs	17.5 hrs
HD 209458	7.65	7.18 x 10^{-5}	245 hrs	61.3 hrs

Table 3.2: Exposure time predictor to compare benefits of observing different star and telescope class combinations. We take 4m-class observations on υ And as our standard, with an exposure time benchmark of 20.0 hrs required to reach the predicted $(f_p/f_*)_{max}$ signal levels. In deriving these estimates we assume that all other variables are equal, such as overall instrument efficiency, observing strategy and weather conditions.

A recent spectroscopic search for the relected-light signature from υ And b (Collier Cameron et al. 2002), has already reached detection limits comparable to the signal levels predicted here, using an échelle spectrograph on a 4m-class telescope. We find the total number of photons that must be collected scales with the square of the planet/star flux ratio, whilst the length of time required to collect this number of photons with a given telescope scales with the flux received from the star. If we adopt 4m-class observations of υ And as our benchmark (20.0 hrs) to reach the $(f_p/f_*)_{max}$ signal levels predicted, then Table 3.2 details the relative exposure times for each planetary system, given access to both 4m and 8m-class telescope facilities. Given that it has been possible to probe to these deep signal levels for υ And in only a few nights on a 4m-class telescope, the remaining five stars are clearly viable and compelling targets for future studies with existing high-throughput spectrographs on 8m-class telescopes. Future instruments that are also likely to be useful in this respect include the high-efficiency fibre-fed échelle spectrograph ESPADONS, which is to be commissioned on CFHT during 2003.

CHAPTER 4

The Search for a Planetary Reflection

4.1 Introduction

The primary aim of our technique is the direct detection of starlight reflected from the surface of a close-orbiting Pegasi planet. In conducting ground-based observations, we believe Échelle spectroscopy offers the best chance of overcoming the main obstacle to achieving a direct detection, namely the separation of the planet signal from that of the star. As the planet orbits its stellar host, it reflects a faint copy of the stellar spectrum, Doppler shifted due to the orbital motion and much reduced in intensity due to the small fraction of starlight its surface intercepts and scatters toward our line of sight. The Monte Carlo simulations conducted in Chapter 3 suggest that the flux of the scattered starlight is likely to be no more than one part in $\sim 10^4$ of the flux received from the star itself. In the remainder of this chapter, we detail how the high resolution and broad wavelength coverage obtained using Échelle spectroscopy should help us to separate and extract a planet signal from observations of its stellar host.

It is the spectral nature of the observation that is key to achieving signal separation. However, in order to successfully disentangle the distinct radial-velocity signature of the planet, we must first overcome the weak nature of the planet's signal in comparison to that of its host. In conducting stellar observations, we invariably see the appearance of noise and systematic errors from the usual sources, i.e. readout noise, photon statistics, sky background, telluric absorption and instrumental flexure. The small planet/star flux ratio expected ($< 10^{-4}$) suggests that even with the high signal-to-noise ratios (S:N) achievable with 8m and 10m-class telescopes (typical S:N $\sim$ 1000), we would still expect any planet signal to be deeply buried in noise. In Chapter 4.5 we review the spectral deconvolution

process used to substantially boost the S:N achieved during observation, but in the data acquisition stage, we still aim to maximise the accumulated S:N. In basic terms, this necessitates observing nearby bright stars that are known to host Pegasi planets, whilst maximising the number of photons collected, through use of a large collecting surface and/or a high-efficiency spectrograph.

4.2 High-resolution Spectroscopy

In traditional spectrographs a dispersing element (typically a prism or diffraction grating) is used to produce the image of a single-order spectrum, in which the range of wavelengths recordable is limited by the size of the imaging device. The raw CCD image of a typical spectrum shows that much of the detector area away from the spectrum itself is unused. Échelle spectroscopy provides a method of optimising the use of the available detector area whilst maintaining spectral resolution.

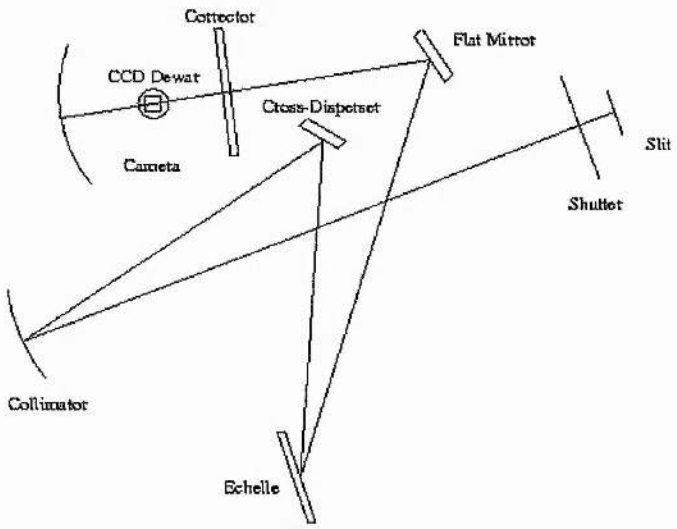

Figure 4.1: Simple diagram to show the typical setup within an échelle spectrograph.

An échelle is a diffraction grating where the rulings are much further apart than usual. This results in a number of short wavelength-range orders of very high spectral dispersion, but which tend to overlap each other. To overcome this effect, a cross-dispersing element is used to spatially separate the orders at the detector. Fig. 4.6 shows a raw échelle spectrum for the star HD75289, recorded using the UV-Visual Échelle Spectro-

graph (UVES) on the VLT(UT2) telescope. The spectrum contains 25 orders running from left to right across the image at a slight angle, with each containing a number of prominent absorption features. Astronomical échelle spectrographs are designed so that the wavelength coverage in one order will overlap the coverage of the adjacent orders. Note that in describing the techniques involved here, we shall demonstrate using the HD75289 data secured on 2003 Jan 13. A detailed description of the HD75289 analysis and results is set out in Chapter 6.

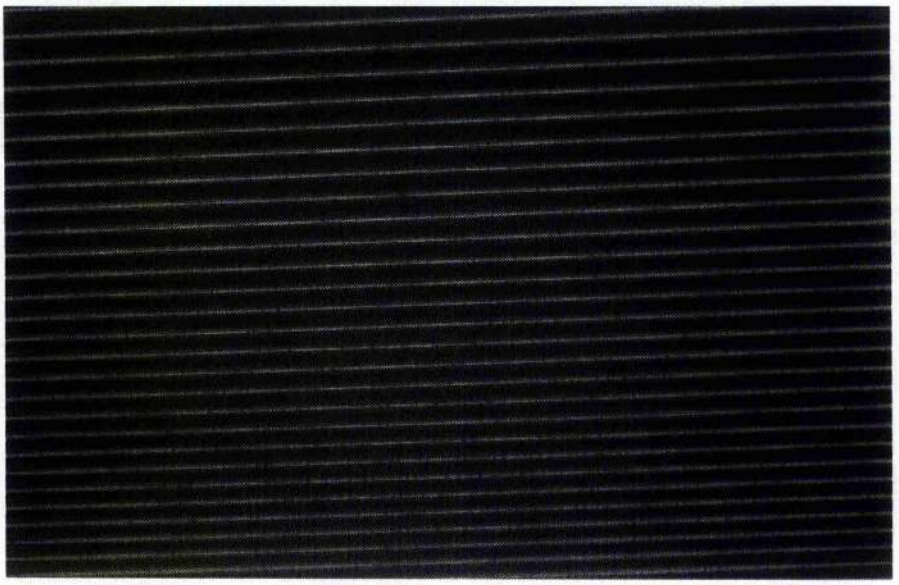

Figure 4.2: Raw échelle spectra of the star HD75289. The images were obtained on 2003 Jan 13 using the UVES instrument, mounted on the ESO VLT(UT2) telescope at the Paranal Observatory in Chile.

As we don't have space to tackle a detailed description of the internal working of an échelle spectrograph, I would refer the reader to descriptions provided by instruments in current use, i.e. VLT/UVES (ESO 2003), KECK/HIRES (Keck 2003), TNG/SARG (IAC 2003) and AAT/UCLES (AAO 2003). For the remainder of this chapter, it is assumed that the reader understands the rudiments of observational spectroscopy.

4.2.1 Data Acquisition

In conducting observations on our target object, the primary aim is to accumulate as many photons as possible whilst sampling a range of orbital phases with the planet at different Doppler shifts. Maximising the acquired S:N requires an observing strategy that monitors

and varies exposure times through the night, such that the CCD pixels are ideally exposed to within 15% of their saturation level. Typically, we aim for S:N in the range 600 - 1000 for the brightest orders in any single exposure, although this very much depends on the length of exposure, brightness of object and prevailing observing conditions. Observational overheads (CCD readout time/preparation) act to reduce the time spent collecting data, but with careful handling observing efficiencies of 80 - 90% can be achieved.

In order to remove detector-related effects we need to obtain a complete set of bias and flat-field frames taken at the start and end of each night. These allow us to characterise and correct for variations in the instrumental response, as detected at the CCD. In order to accurately correct for pixel sensitivities, without degrading the data significantly, it is important to collect at least as many photons in the master flat-field as were accumulated in all the object spectra. This requires summing $\sim$ 100-200 flat-field exposures, obtained during daylight hours, using tungsten lamps designed for the purpose. The master flat-field is then used to construct a balance-factor frame to be applied during the spectral extraction process. Additional calibration frames required include trace frames and Arc (Thorium-Argon) frames for wavelength calibration, although these will shortly be discussed in more detail.

4.2.2 Spectral Extraction

The extraction of échelle spectra to 2-D images is similar, in principle, to the extraction of a single-order spectrum, but presents a few additional considerations. The main problem is that the orders have a more complex spectral profile than seen with a single-order instrument. Additional difficulties arise in flat-fielding the data and require that we take a careful approach. Fortunately, there are several dedicated software packages available which address these specific features of échelle data reduction. In this analysis we have chosen to extract the raw data using automated pipeline reduction scripts built around the Starlink ECHOMOP and FIGARO packages.

Data Preparation

Prior to attempting the extraction, it is essential to prepare the data carefully. After subtraction of the median bias frame ($\sim$ 40 of which are obtained each night), each object

and Arc frame is cropped to remove the overscan regions and rough edges of the CCD, which can sometimes confuse the algorithms in the échelle data reduction engine. The final step involves rotating and orientating the frames to meet the criteria expected by ECHOMOP, i.e. orders run roughly horizontal with wavelength increasing from left to right. Once the set of Arc and object images have been prepared in this way the extraction process can begin.

ECHOMOP - Échelle Data Reduction Package

The initial identification and tracing of the échelle orders on the CCD frames is performed manually using a dedicated narrow-order trace frame. In the absence of a specific frame for this task, one can trace using the spectrum of a hotter B star that has relatively few absorption features, or in some cases the spectrum of the target star itself.

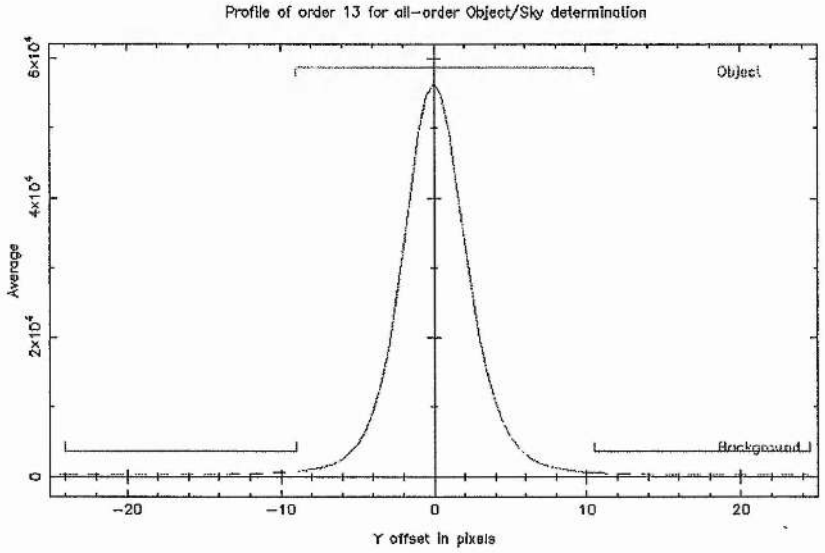

Figure 4.3: Spatial profile of the central order of the spectrum for HD75289. Its extent determines which parts of the profile contain the spectral information and which can be used to calculate the sky background.

Once the location and path of the orders has been determined from fits to the trace, a lateral (or spatial) cut is taken to manually identify their profile and extent (Fig 4.3). Regions beyond the wings of the spatial profile in each order are used to model a linear fit to the scattered-light (or sky) background, which is subsequently removed from all frames. Flat-field balance factors are applied at this point to correct for the pixel-to-pixel

variations in the instrumental response seen at the detector. After modelling the object profile across all orders, the process performs an optimal (profile and inverse-variance weighted) extraction of the orders across the full spatial extent of the object region. With the extraction of both object and Arc frames, comes the time consuming and much loved process of wavelength calibration. The location of emission line features within the Arc frame is followed by a manual process to identify them (see Fig. 4.4) from a reference list of known Thorium-Argon features.

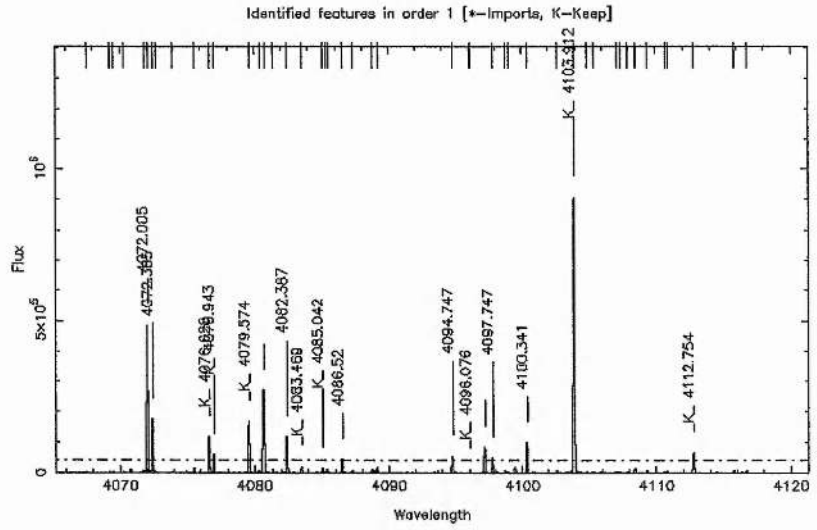

Figure 4.4: Wavelength calibration and extraction of a typical spectra using ECHOMOP. The screenshot shows the identification of emission features within the first spectral order of the Arc (Th-Ar lamp) frame.

The results of the wavelength calibration are attached to the extracted object frame, with both written to a 2-D échellogram in Starlink NDF format, suitable for subsequent processing. The remaining object frames are then extracted automatically using parameters set in this first manual extraction. Fig. 4.5 shows a full 2-D échellogram of the star HD75289, as extracted from a raw échelle spectrum (Fig. 4.2) secured on VLT(UT2)/UVES. The échellogram represents 25 high-resolution single-order spectra, similar to that in Fig. 4.6a, stacked to form a single object with complete wavelength coverage from 4000 - 5200 Å. The overlap of adjacent orders in the spectral direction results in roughly 2400 images of the $\sim$ 1800 absorption features detected within the spectrum. A well-known feature of échelle spectroscopy is that the spectral sensitivity in a given order decreases toward the wings. This characteristic is known as the "blaze function" and arises

from the manner in which light is reflected by the échelle grating. The presence of such a strong continuum profile, shown clearly in Figs. 4.5 and 4.6, requires careful handling in subsequent processing, especially when dealing with the associated errors.

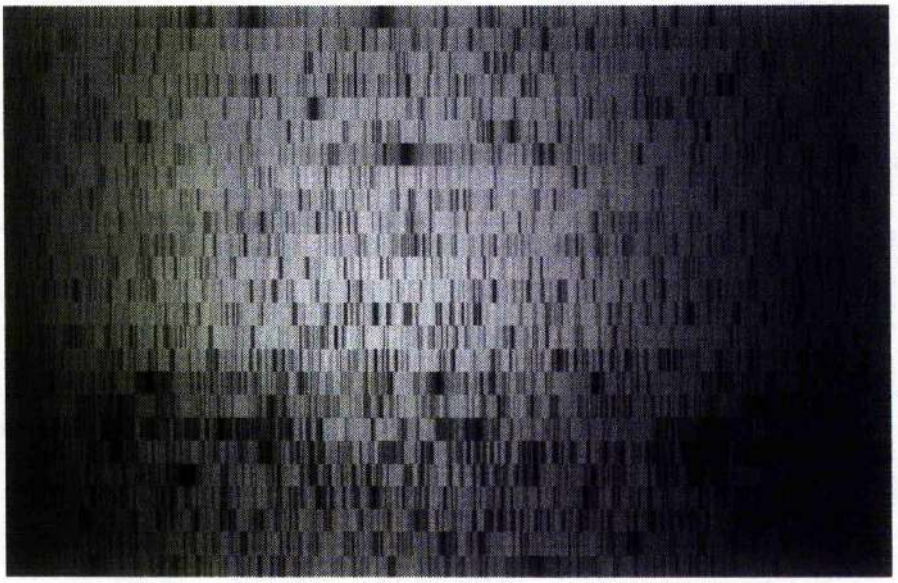

Figure 4.5: The resulting reduced échellogram following ECHOMOP extraction. The form of the continuum profile and resultant dimming towards the wings of the orders results from the blaze function.

4.3 Separating the Planet Signal

The next stage in the process requires us to accurately model and remove the intrinsic spectrum of the star to leave the planetary reflection, which at this stage is still buried deeply in the noise. In modelling the star, we create a stellar template from the co-aligned sum of all the spectra secured on each night of observation. As the planet's Doppler shift changes through the night, the summation allows us to average out any reflected-light contribution present in the data, such that subtraction of the template from individual spectra does not remove too much of the planetary signal.

We begin by removing cosmic-rays from the individual frames. To achieve this we divide each target spectrum by its predecessor, with the result smoothed using a median box filter covering 21 pixels in the dispersion direction and 5 adjacent orders. The smoothed frame is used to scale the predecessor frame, which is then subtracted from the

target frame. The resulting difference frame is divided by the square root of the target frame to yield deviates in units of the local Poissonian noise amplitude. All pixels whose deviates are more than 7 sigma in excess of their counterparts in the scaled predecessor frame are assumed to be cosmic ray hits and are replaced with the corresponding pixel value from the scaled predecessor frame. The cleaned target frames are then shifted linearly (if required) to co-align the stellar absorption lines to the nearest integer pixel. Such a shift is not generally required with stable platforms such as VLT(UT2)/UVES, however, with WHT/UES, one finds that the spectral image moves across the detector during the night, resulting in significant misalignments between frames taken at the start and end of observation. Once aligned, the frames are then summed to create the stellar template.

The next stage involves scaling, shifting and de-blurring the stellar template prior to subtraction from the individual spectra. The first two derivatives of the template frame are calculated from the template values t_j in each order, as a function of pixel number x_j in the dispersion (spectral) direction:

$$t'_j = \frac{t_{j+1} - t_{j-1}}{x_{j+1} - x_{j-1}} \ , \tag{4.1}$$

and

$$t''_j = 2\frac{(t_{j+1} - t_j)/(x_{j+1} - x_j) - (t_j - t_{j-1})/(x_j - x_{j-1})}{x_{j+1} - x_{j-1}} \tag{4.2}$$

The third and fourth derivatives are calculated by performing the same operations on t'', and are used to correct frame-to-frame variations in the higher moments of the Point Spread Function (PSF) and seeing profile.

We then model the vector $\boldsymbol{f}$ of all observed spectrum values within each extracted échelle order, by scaling the template $\boldsymbol{t}$ along each order. The scale factors vary as a function of position $\boldsymbol{x}$, and are approximated by a 34-knot least-squares spline. We need such a high-order spline to tackle the vignetting near the edges of each order, which produces abrupt and time-variable changes in the slope of the stellar continuum. The derivative frames were scaled in a similar fashion, using 6-knot splines to define the scale factors. A further 6-knot spline was calculated to provide a smooth background correction for any inconsistencies in the scattered-light subtraction during the extraction process. The scaled, aligned and de-blurred template spectrum thus has the form

$$g_j = \alpha_j t_j + \beta_j t'_j + \gamma_j t''_j + \delta_j t'''_j + \epsilon_j t''''_j + \eta_j \tag{4.3}$$

where α_j is the value at x_j of a 34-knot spline and β_j, γ_j, δ_j, ϵ_j and η_j are the values of the corresponding 6-knot splines used to scale the derivatives and correct for the background. The knot values for the various splines were determined by the method of least squares using singular-value decomposition to ensure that spurious fluctuations were suppressed in those parts of the spectrum where few lines were present.

The best-fit stellar template $\boldsymbol{g}$ is then subtracted from the observed spectrum $\boldsymbol{f}$ to leave a residual spectrum $\boldsymbol{r}$ composed mainly of noise. If the planet velocity is sufficient that absorption lines in the reflected starlight are shifted clear of those in the direct starlight, then the residual spectrum is expected to retain the reflected starlight signal buried deeply in Poissonian noise. The next step is to pull this signal out of the noise, but before that we need to investigate and remove any fixed-pattern noise in the residual spectrum.

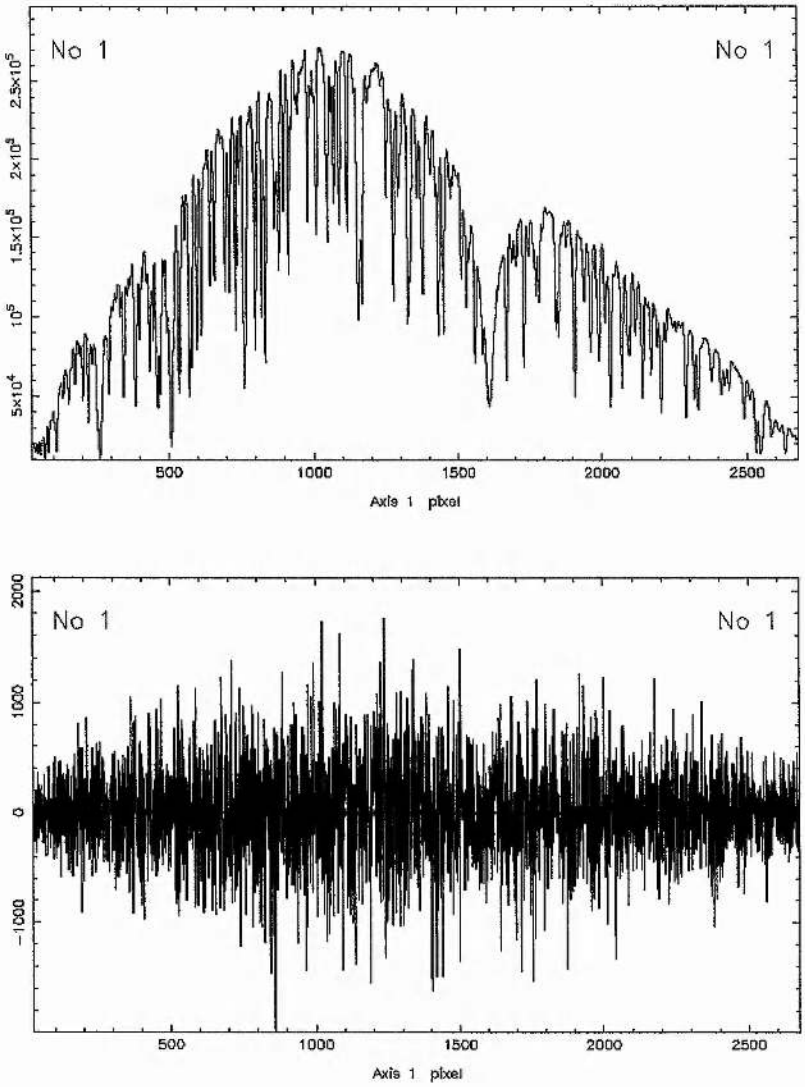

Figure 4.6: (a) Single order of a typical stellar spectrum above (b), the resulting residual spectrum following subtraction of the scaled, aligned and de-blurred stellar template. We note a residual rms scatter of ~ 600, which when compared to maximum stellar photon flux of $\sim 2.5 \times 10^5$, suggests a S:N ~ 400 for the brightest parts of this image.

4.4 Principal Component Analysis

When the aligned stellar template is subtracted from the direct starlight, we find that the residual spectra exhibit a spatially fixed but time variable pattern of ripples. Closer inspection suggests that the ripple pattern is attributable to a combination of time dependent changes in the sensitivity of the detector, thermal flexure in the spectrograph and changes in the strength of telluric-line absorption features in some of the orders.

The significance of this fixed-pattern noise was first investigated by Collier Cameron et al. (2002) who used a Principal Component Analysis (PCA) technique to isolate and compensate for its effects. They compared the scatter of pixel values in each residual spectrum with what might be expected from photon statistics alone. By dividing each object spectrum by the square root of its computed variance, they found several hundred outliers in the distribution of pixel deviates, caused mostly by systematic errors in the polynomial fits to half a dozen regions affected by defects on the CCD. Despite clipping at ± 4 times the expected local root-mean-square (rms) photon noise amplitude, they found a Gaussian distribution in the remaining values, with an rms error ~ 1.5 times the expected value. In addition, there was a significant correlation between pixel values in successive residual frames, indicating that some fixed-pattern noise sources had not been fully eliminated by the template alignment and subtraction. The residuals in pairs of frames taken several hours apart or on different nights were also found to be correlated, though in some instances the slope of the correlation was reduced or even reversed.

We can map and correct for these spatially fixed but time-varying patterns by use of a technique involving principal component analysis. PCA is a statistical method widely used in data analysis and compression. It involves the linear transform of a number of (possibly) correlated pixel-values into a number of uncorrelated pixel-values called *principal components*. The first principal component accounts for the majority of the commonality in the data, with each successive component containing the remaining variance in the data but increasingly less commonality. By subtracting the first two principal components from a temporally-varying stack of residual spectra we should, in theory, remove most of the fixed-pattern noise.

Traditionally, PCA is performed on a square symmetric matrix. If we take a set of M spectra, each of length N pixels, then the ith spectrum has elements $\boldsymbol{s}_i = \{s_{i1}, s_{i2}, \ldots, s_{iN}\}$

and associated variances $\boldsymbol{\sigma^2}_i = \{\sigma_{i1}^2, \sigma_{i2}^2, \ldots, \sigma_{iN}^2\}$. The covariance matrix of the temporal variations in the individual spectral bins of this set of spectra is a real symmetric matrix of dimensions $N \times N$, whose elements are given by:

$$H_{jk} = \sum_{i=1}^{M} \frac{(s_{ij} - \hat{s}_j)(s_{ik} - \hat{s}_k)}{\sigma_{ij}\sigma_{ik}}. \tag{4.4}$$

Note that we subtract the inverse variance weighted mean spectrum $\hat{s}$ before computing the covariance matrix. The jth spectral bin of $\hat{s}$ is given by:

$$\hat{s}_j = \frac{\sum_{i=1}^{M} s_{ij}/\sigma_{ij}^2}{\sum_{i=1}^{M} 1/\sigma_{ij}^2}. \tag{4.5}$$

The eigenvalues and eigenvectors of the covariance matrix are determined using Jacobi's method (Press et al. 1992), although this requires that we process the spectra in wavelength segments of length $\sim$ 100 pixels to keep the computer processing time down. The eigenvector associated with the largest eigenvalue has the same direction as the first principal component. In a statistical sense the principal components are those eigenvectors of the covariance matrix accounting for the largest fraction of the variance.

Collier Cameron et al. (2002) found that most of the unwanted additional variance in their υ And spectra was contained in the first two principal components, suggesting two independent sources of fixed-pattern noise. The first principal component contained a spatially fixed but temporally-varying pattern of ripples affecting all orders. This they attributed to a slow drift in the sensitivity pattern of the flat field. The second principal component consisted mainly of imperfectly-subtracted telluric absorption features that appeared at variable strengths in some of the orders.

Once the degree of the fixed-pattern noise contribution for each exposure is established using PCA, it can be subtracted from the residual frame. The method effectively removes any correlation between successive frames, and has been found to reduce the RMS scatter in the pixel values to within $\pm$10% of the value expected from photon statistics alone. The planet signature should not be affected by this procedure any more than it is affected by the template subtraction because, unlike the fixed-pattern noise, it is smeared out by orbital motion. Nonetheless, it is important for the subsequent matched-filter analysis (Chapter 4.6), to investigate and quantify any signal loss. This can be achieved by monitoring the progress of a simulated planet signal through each of the processing steps, as detailed in Chapter 4.8.

4.5 Least Squares Deconvolution

Once the fixed-pattern noise has been removed from the data, we extract the reflected-light signature from the residual frames using a weighted least-squares deconvolution (LSD) technique, described initially by Donati et al. (1997). In brief, the method involves taking a list of photospheric absorption lines for a given stellar type and calculating a "mean" line profile which, when convolved with the line list, gives an optimal match to the observed spectrum. The deconvolved line profile thus incorporates an average broadening function that is representative of all the lines recorded in the spectrum. Since we expect the planet to reflect the same pattern of absorption-lines as the host star, the technique of LSD should prove an effective way of measuring the average line profile of any faint planet signature within the residual spectrum (from which the stellar signal has been removed).

4.5.1 Mathematical description of the LSD

In order to apply our technique we first need a line list. The list details the wavelength of each absorption line, together with its relative weighting (defined as the depth of the unbroadened absorption lines) within a normalised spectrum. A set of line-lists were generated by Donati et al. (1997) for a number of different stellar types, using the model atmospheres of Kurucz (1993). With the majority of Pegasi planet hosts having a spectral-type close to that of the Sun, we believe the model line-list for a G2V star with solar metallicity should provide good results for all our target stars. Note, that we do not benefit significantly from the inclusion of weak lines, and thus concentrate our analysis on lines where the central depth exceeds 0.4 normalised units.

The predicted residual spectrum $\boldsymbol{p}$ is the convolution of a "mean" line profile $\boldsymbol{z}$ with the line-list of weighted delta functions $\boldsymbol{\alpha}$ (see Fig. 4.7), according to

$$\boldsymbol{p}_j = \sum_k \boldsymbol{\alpha}_{jk} \boldsymbol{z}_k \tag{4.6}$$

where j is the spectral element (pixel) and k an element (bin) of the deconvolved profile. The profile is defined on a linear velocity scale for the projected orbital velocity K_p, and is determined from the average velocity change per pixel shift in the extracted spectra, Δv. This value is instrument dependent, but for the WHT/UES configuration, the resolution and pixel size combine to give $\Delta v = 3$ km s^{-1} per pixel bin, whereas for VLT/UVES,

$\Delta v = 1.5$ km s^{-1} pixel^{-1}. The $N_j \times N_k$ elements of the convolution matrix, $\boldsymbol{\alpha}$, are defined in terms of line weights $\boldsymbol{w}_i$ and the triangular interpolation function $\Lambda(x)$, where

$$\boldsymbol{\alpha}_{jk} = \sum_i \boldsymbol{w}_i \Lambda(x) \tag{4.7}$$

and

$$x = \frac{\boldsymbol{v}_k - c(\frac{\boldsymbol{\lambda}_j - \boldsymbol{\lambda}_i}{\boldsymbol{\lambda}_i})}{\Delta v} \tag{4.8}$$

in which,

$\boldsymbol{w}_i$ = weighting (depth) of line i

$\boldsymbol{\lambda}_i$ = wavelength of line i

$\boldsymbol{\lambda}_j$ = wavelength of spectrum pixel j

$\boldsymbol{v}_k$ = radial velocity of deconvolved profile bin k

Δv = velocity increment per pixel within the deconvolved profile

The triangular function $\Lambda(x)$ is defined such that

$$\begin{aligned} \Lambda(x) &= 1 + x \qquad \text{for} \quad -1 < x \leq 0 \\ &= 1 - x \qquad \text{for} \quad 0 \leq x < 1 \\ &= 0 \qquad\quad \text{elsewhere} \end{aligned}$$

In this way, the elements of the convolution matrix $\boldsymbol{\alpha}_{jk}$ are calculated by summing, over all spectral lines i, the contribution of the deconvolved profile element at velocity v_k, to the corresponding data pixel at wavelength λ_j when the centre of the deconvolved profile is shifted to the wavelength λ_i of each line in turn. The α matrix is effectively a weighting mask that only includes regions of the spectrum covering the deconvolution range of wavelength/velocity space.

Our next step is to determine the unknown deconvolved profile $\boldsymbol{z}_k$ for the observed data. We use the χ^2 function to obtain the inverse variance weighted fit of the convolved line-list and deconvolved profile, to the normalised residual spectrum $\boldsymbol{r}_j$,

$$\chi^2 = \sum_j \left(\frac{\boldsymbol{r}_j - \sum_k \boldsymbol{\alpha}_{jk} \boldsymbol{z}_k}{\boldsymbol{\sigma}_j} \right)^2 \tag{4.9}$$

where σ_j represents the observational errors associated with the individual spectral bins and therefore weights the fit optimally with respect to the photon counts in the spectrum. The equation is minimised by solving for

$$\frac{\partial \chi^2}{\partial z_k} = 0 \tag{4.10}$$

to obtain an expression in which z_k is the only unknown,

$$\sum_j \frac{1}{\sigma_j^2} \sum_k \alpha_{jk} \sum_l \alpha_{jl} z_l = \sum_j \frac{1}{\sigma_j^2} r_j \sum_k \alpha_{jk} \tag{4.11}$$

If the inverse variances $1/\sigma^2$ are assigned to the diagonal matrix $\boldsymbol{V}$, and the residual spectrum elements r_j to vector $\boldsymbol{R}$, then the equation can be written in the same matrix format as Eqn. 4 in Donati et al. (1997), namely

$$\boldsymbol{z} = (\boldsymbol{\alpha}^T.\boldsymbol{V}.\boldsymbol{\alpha})^{-1}\boldsymbol{\alpha}^T.\boldsymbol{V}.\boldsymbol{R} \tag{4.12}$$

where $\boldsymbol{\alpha}^T.\boldsymbol{V}.\boldsymbol{R}$ represents the cross-correlation of the residual spectrum with the line weighting matrix or mask. However, unlike standard cross-correlation techniques, the solution gives a flat deconvolved profile outside the regions occupied by the residual stellar spectrum. As a result the procedure compensates for the effect of spectral line blends and leaves the profile free of the resulting side-lobes. Since the square matrix $\boldsymbol{\alpha}^T.\boldsymbol{V}.\boldsymbol{\alpha}$ is symmetric and positive-definite, the least-squares problem can be solved using efficient methods such as Cholesky decomposition (Press et al. 1992).

The formal errors on the N points of the deconvolved profile $\boldsymbol{z}$ are obtained in the usual way from the diagonal elements of the $N \times N$ covariance matrix

$$\boldsymbol{C} = (\boldsymbol{\alpha}^T.\boldsymbol{V}.\boldsymbol{\alpha})^{-1} \tag{4.13}$$

The deconvolution process is conducted using a purpose built fortran routine called SPDECON (Barnes et al. 1998). The result is a deconvolved profile, similar to that at Fig. 4.8, expressed in units of the weighted mean continuum level of the observed object spectrum. The deconvolved profile typically extends from -200 to +200 km s^{-1}, to take in regions of velocity space that the Doppler shifted planet is expected to occupy. As such, the extent of the profile is driven by the orbital nature of the planetary system.

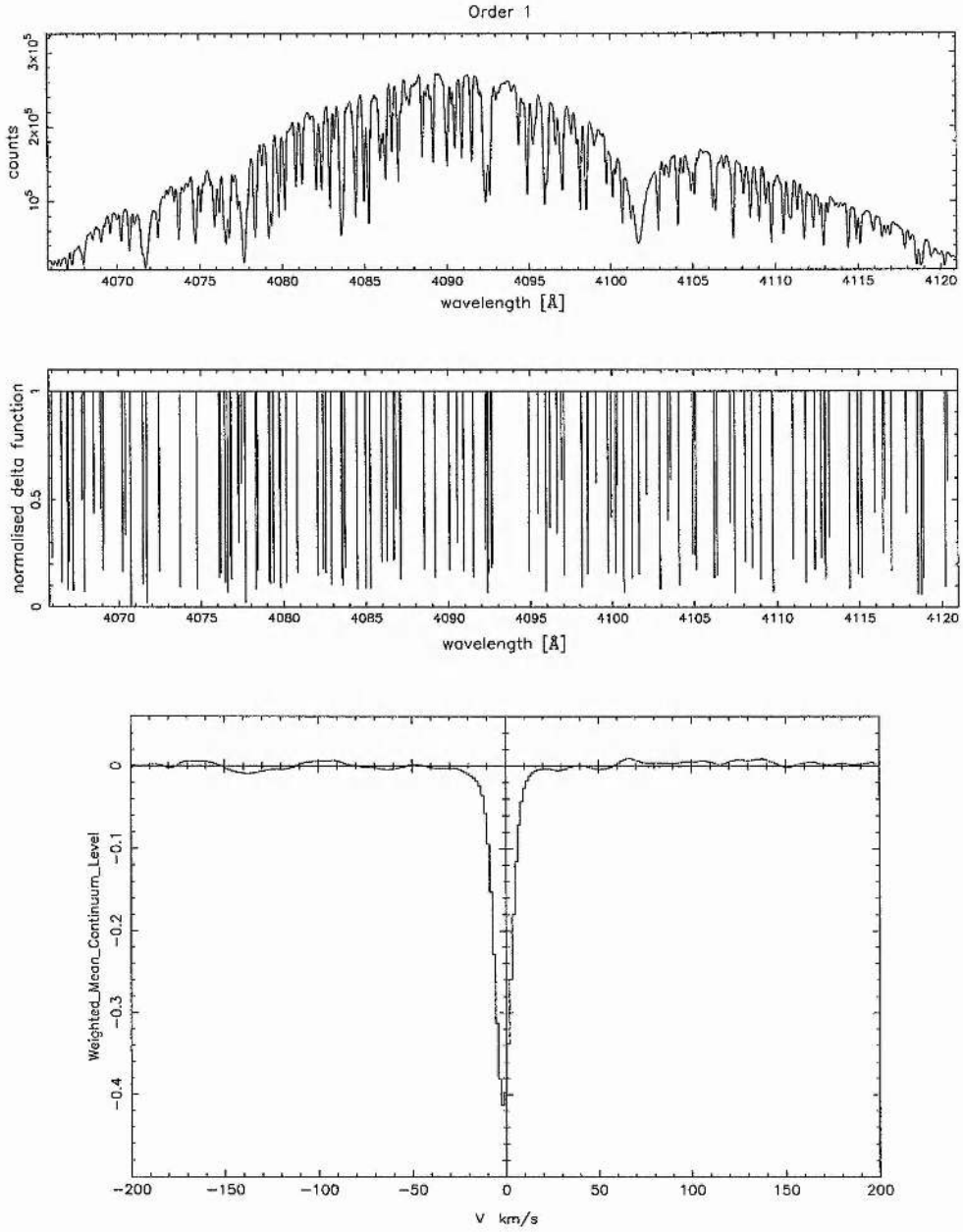

Figure 4.7: By deconvolving a stellar spectrum (upper panel) with a close spectral-type line-list of weighted delta functions (middle), we obtain a "mean" line profile (lower panel) that exhibits the average broadening function of all absorption lines within the wavelength range in question. Here the line profile shows the broadening function seen in all 25 orders of a single HD75289 spectrum. It allows us to estimate the $v \sin i$ of the star at ~ 5 km s^{-1}, which is in reasonable agreement with the value of 4.4 ± 1.0 km s^{-1} obtained by Benz & Mayor (1984). The profile also suggests that, at the time of observation, HD75289 had a relative velocity of 1.7 km s^{-1}, which has to be corrected for in the residual profiles.

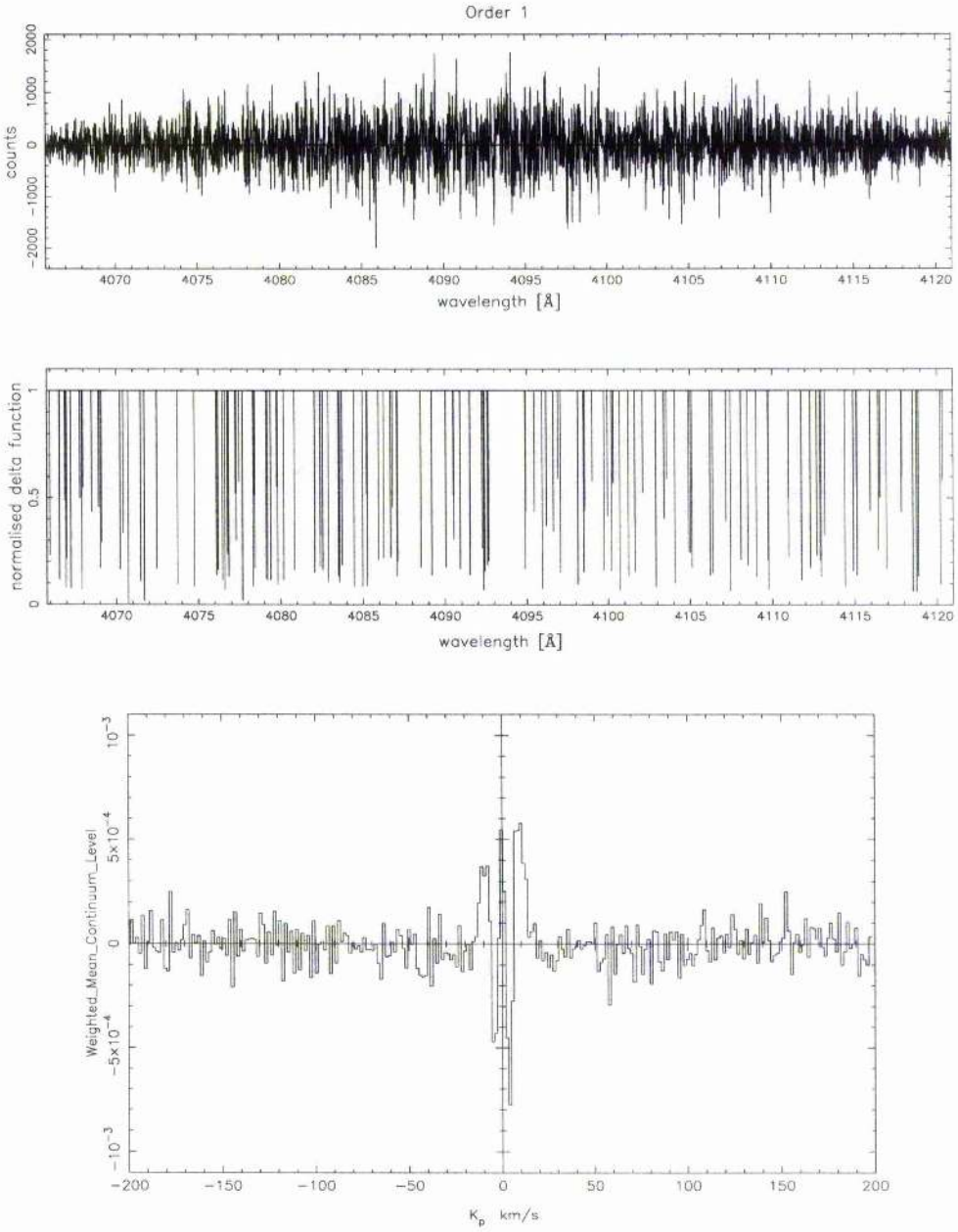

Figure 4.8: The same deconvolution as in Fig. 4.7, but this time conducted on the residual profile (stellar template removed). The profile is defined in terms of the projected orbital velocity K_p of the companion object, and is given in units of the mean weighted continuum level, so as to indicate its relative brightness. The strength of any planet signal present in the data is expected to be approximately the same as the scatter in the noise. The distortions seen in the centre of the line profile are artefacts from high-order mismatches in the stellar template subtraction procedure (see later).

4.5.2 Quantifying the S:N gain

In terms of noise reduction (or signal enhancement), LSD effectively aligns and averages the profiles of all photospheric absorption lines that appear in the échellogram and are included on the line list. As each individual absorption line can appear in adjacent échelle orders, we have more images of lines than are listed in the observed wavelength range. If the continuum signal were constant across the whole frame and the strength of all lines equal, then the S:N of the deconvolved profile would be proportional to the square root of the number of line images processed. For example, a spectrum in which there were 6000 images of 3300 listed spectral lines, would see a theoretical S:N improvement of $\sqrt{6000} \sim 75$. In practice, the continuum is subject to the blaze function and there is a wide variation in line depths.

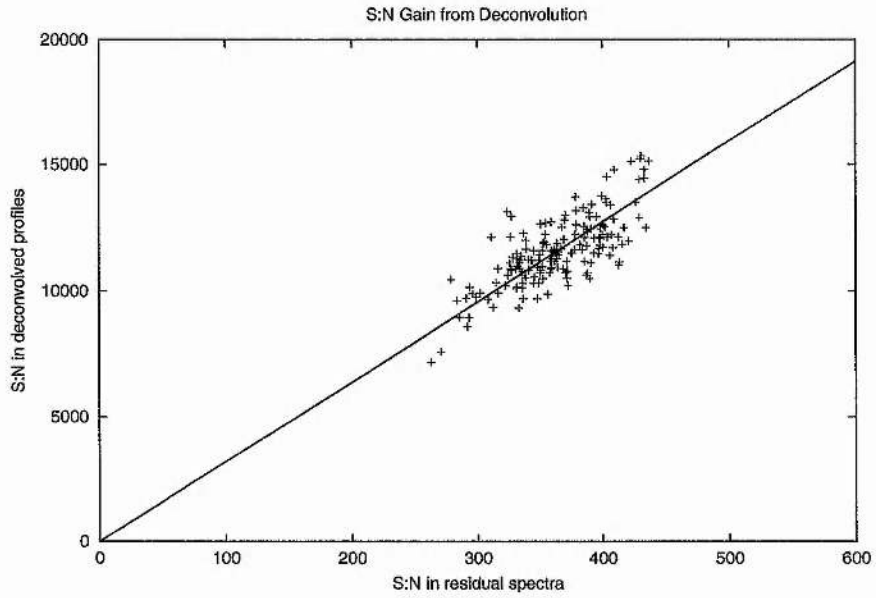

Figure 4.9: We plot the signal-to-noise (S:N) ratio seen in the deconvolved profiles against that seen in the residual spectra, to assess the gain in S:N from the LSD technique. A linear fit to the HD75289 data secured on 2003 Jan 13 yields a S:N gain close to 32.

We investigated the efficiency in the S:N gain generated by SPDECON, by analysing HD75289 data secured on 2003 Jan 13 using VLT(UT2)/UVES. Once again, full details of the acquisition and processing of the HD75289 spectra are set out in Chapter 6. We define the S:N gain as the ratio of the S:N seen in the deconvolved line profile, to that seen in the orders of the residual spectra prior to deconvolution. To overcome the variation

in signal intensity (and hence S:N) across the blazed orders, the input S:N we calculate is the ratio of the average signal strength across the extracted spectrum to the scatter observed in the residual spectrum, i.e. $\langle S \rangle / \langle \sigma \rangle$. The S:N values for the HD75289 data, as determined by the FIGARO ISTAT package, were found to vary between 260 and 440 depending on the time of exposure. As SPDECON normalises the deconvolved profile to unity, the deconvolved S:N is determined directly as the inverse of the scatter in the continuum beyond the wings of the deconvolved profile (Fig. 4.8). We measure within the continuum of the profile for two reasons, first, because it avoids the absorption line profile of the star where mismatches during stellar template subtraction can cause anomalies, and second, because the continuum is where we expect to detect any planet signal, at times when it is Doppler shifted well clear of the stellar signature.

Fig. 4.9 shows the input S:N values plotted against the S:N seen in the deconvolved profiles of the HD75289 spectra. A linear fit to the resulting distribution suggests a mean multiplex gain of ~ 32, which compares well with the maximum theoretical gain ($\simeq 48.5$) possible from the 1744 absorption lines listed within the observed wavelength range, of which there are 2360 images.

Least-squares deconvolution reduces noise in the deconvolved profiles to $\sim 10^{-4}$ times the signal strength in the extracted object spectra, and puts us in the right ballpark for attempting the detection of any reflected-light signature within the data.

4.6 Matched Filter Analysis

We expect the radial velocity of the Pegasi planet to vary sinusodally with the orbital phase, as all the absorption features attributable to the reflection are periodically Doppler shifted to longer then shorter wavelengths. If the intrinsic widths of the line profiles in the reflected starlight are similar to those in the direct light, then our work in Chapter 3 suggests the central depth of any planetary absorption feature should lie between 10^{-5} and 10^{-4} (normalised units) when viewed at zero phase angle. In practice, the depth of the feature will be less than this, since the planet signature is only separable from the stellar profile when its phase angle is more than 20° away from superior conjunction. The amplitude is further diluted during the construction of the stellar template spectrum, where the planet signal from individual images will combine to generate a smeared planetary con-

tribution. This additional contribution will be particularly strong near quadrature (see later). All told, we still expect the central depth of the planetary signature within each image to be comparable with the RMS noise amplitude in the individual profile bins, as seen in Fig. 4.8. Thus no single profile is expected to yield a significant detection. To improve our chances of detection we must investigate the signal contribution of the planet at many different orbital phases.

Given an assumed orbital inclination, we can calculate the sinusoidal path the planet should follow through velocity space, together with the corresponding variations in signal strength. In order to search for a pattern of faint features displaying the expected behaviour, we construct a set of matched filters that can be shifted and scaled to fit the data. Our first task in looking for the planet signal is to stack each deconvolved profile into a phased time series. This is achieved by comparing the time of exposure with the orbital ephemeris (time of inferior conjunction) and period obtained from the radial velocity studies, as determined by Udry et al. (2000) for the case of HD75289. In doing so we construct a phased deconvolved profile, as shown at Fig. 4.10, with 500 phase bins used to cover the entire orbit. Note that the phase binning is used for display purposes only and that subsequent matched-filter operations are conducted on the original unbinned time series.

Our next step is to model the reflected-light signal by a sequence of gaussians with the appropriate velocities and relative amplitudes:

$$\begin{aligned} G(v,\phi,K_p) &= \frac{W_*}{\Delta v_p\sqrt{\pi}} g(\phi,i) \times \\ &\quad \times \exp\left[-\frac{1}{2}\left(\frac{v - K_p \sin\phi}{\Delta v_p}\right)^2\right]. \end{aligned} \tag{4.14}$$

The amplitude K_p of the sinusoidal velocity variation is determined by the system inclination and stellar mass according to Eqn. 2.20. The orbital phase ϕ is known to high precision from the ephemeris for times of transit derived from the radial-velocity curve and shown at Appendix A.2. The phase angle α can be determined at any orbital phase from Eqn. 2.11. W_* is the integrated area of the deconvolved stellar line profile, and Δv_p is the characteristic width of the planet's reflected-light profile. The phase function $g(\phi,i)$ is given by Eqn. 2.12 or 2.14.

Fig. 4.11 uses a simulated planet signal to demonstrate the trail we would expect

to see in the presence of a genuine reflected-light detection. By adding a simulated planet signal to the observed spectra, we can test to see whether a faint planetary signal would survive through the sequence of operations described here, in the presence of realistic noise levels. The purpose of the matched-filter analysis is to generate a model which best matches any such trail.

The weakening of the signature near quadrature (phase 0.25 and 0.75) is primarily a result of the phase function, but can in some circumstances be exacerbated by the way in which we construct the stellar template. Because the radial velocity of the planet changes very little close to quadrature, summation of object frames at these phases will create a significant planetary contribution within the resulting stellar template, signal which will be lost in the subsequent subtraction. In generating reflected-light models to match the data, we first need to address issues surrounding this signal loss.

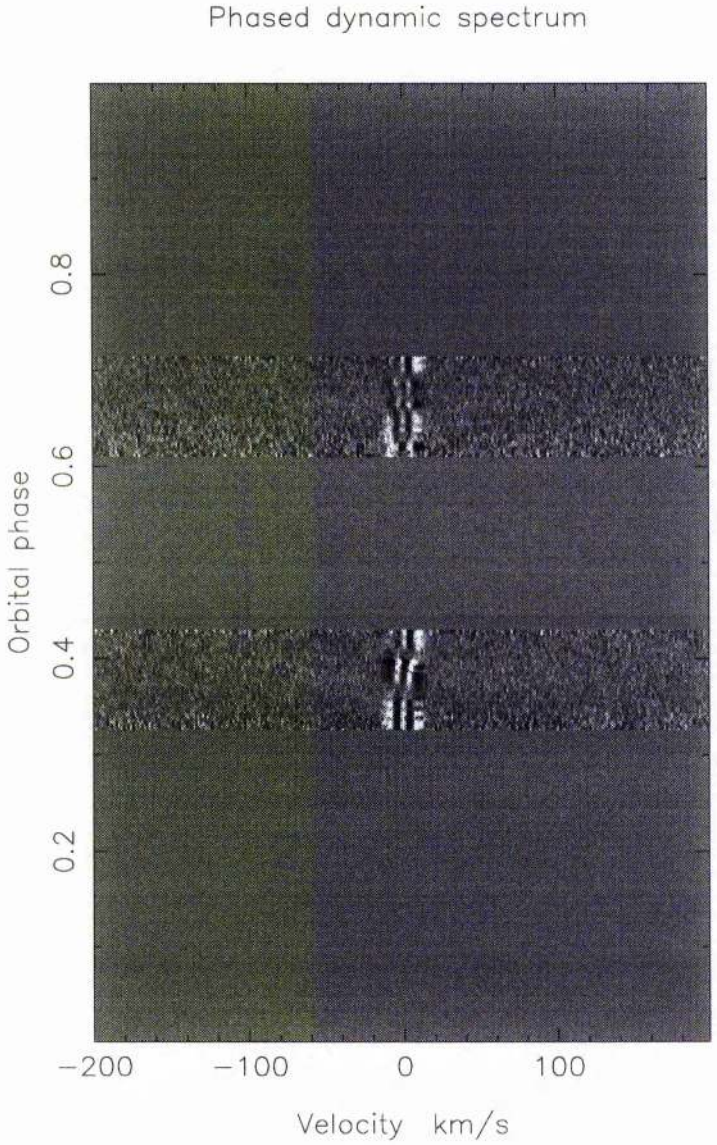

Figure 4.10: This velocity-phase map stacks the deconvolved residual profiles according to the orbital phase at time of exposure. Here we adopt a hypothetical orbital solution (for demonstration purposes) for the 4 nights of VLT(UT2) data secured in 2003 Jan. Any planet signature is expected to resemble a travelling Gaussian of characteristic width Δv_p, whose velocity varies sinusoidally around the orbit and whose strength is modulated by the phase function $g(\phi, i)$. No such trail is obvious here.

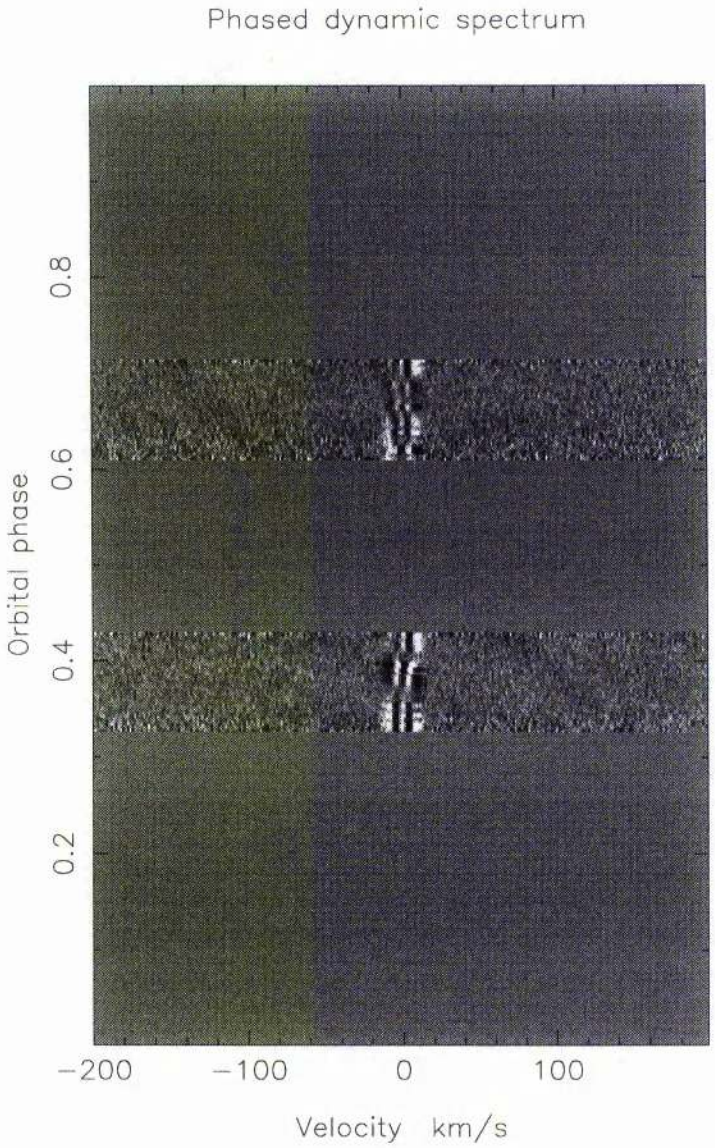

Figure 4.11: As for Fig 4.10 but with the addition of a simulated planet signal at an inclination of 80°. The planetary signature appears as a dark sinusoidal feature crossing from right to left as phase increases and centred on phase 0.5. Note, that the dates of observation are chosen to maximise the observable reflected-light obtained as the planet passes behind its stellar host. Ideally we aim to target gibbous phases $0.33 < \phi < 0.47$ and $0.53 < \phi < 0.67$ where it is possible to disentangle the planet spectrum from the direct stellar spectrum.

4.6.1 Attenuation by Stellar Template

The stellar template we previously subtracted from each object spectrum will have contained a blurred contribution from any planet signal present, which, as we have just stated, is most prominent near quadrature. To ensure that the matched filter accurately mimics the effects of subtracting the template, we subtract the inverse variance-weighted average of the travelling gaussian. If σ_{ij}^2 is the variance of the ith velocity bin in the jth deconvolved profile, then the attenuated basis function becomes:

$$H(v_i, \phi_j, K_p) = G(v_i, \phi_j, K_p) - \frac{\sum_j G(v_i, \phi_j, K_p)/\sigma_{ij}^2}{\sum_j 1/\sigma_{ij}^2}. \tag{4.15}$$

In short, the procedure mimics the attenuation of the planet signal which results when the stellar template spectrum is subtracted from the individual spectra. To allow for any systematic errors in the continuum level following template subtraction and deconvolution, we next subtract the inverse variance-weighted mean value of the deconvolved profiles at each orbital phase. If d_{ij} is the original data value in the time-series of deconvolved profiles, then

$$D_{ij} = d_{ij} - \frac{\sum_i d_{ij}/\sigma_{ij}^2}{1/\sigma_{ij}^2} \tag{4.16}$$

gives the resulting orthogonalised data pixel value, with the matched filter H_{ij} orthogonolised in the same way.

In searching for a match, we exclude all pixels within $\sim$ 30 km s^{-1} of the core of the stellar absorption line. In doing so we hope to eliminate spurious effects arising from the strong "Barber's Pole" pattern of distortions seen at low velocities in the time-series of deconvolved profiles. The pattern appears to be an artefact of high order mismatches in the stellar template subtraction procedure. As they vary too rapidly to be caused by stellar surface features (starspots, faculae), the more likely explanation rests with nightly variations in the orientation of the line profile, possibly as a result of rotation of the stellar image, or sub-pixel shifts across the spectral-axis of the detector due to flexure of the telescope. Fortunately they only affect a range of velocities at which the planet signature would in any case be indistinguishable from that of the star.

4.6.2 Scaling the matched filter

We generate a sequence of models, for different values of K_p, which we use as matched filters to measure the strengths and velocity amplitudes of any weak signals (of the expected form) that appear within the data. For each trial K_p, we construct a model basis function $H(v, \phi, K_p)$, which is scaled to give an optimal fit to the data values D_{ij} in the velocity-phase map. The basis function is normalised prior to scaling such that the scaling factor we return is ϵ_0, i.e. the planet/star flux ratio at $\alpha = 0$ as defined in Eqn. 2.16. Formally we have

$$\epsilon_0(K_p) = \sum_{i,j} \frac{D_{ij} H(v_i, \phi_j, K_p)/\sigma_{ij}^2}{H^2(v_i, \phi_j, K_p)/\sigma_{ij}^2} \tag{4.17}$$

and

$$\mathrm{Var}(\epsilon_0) = \sum_{i,j} \frac{1}{H^2(v_i, \phi_j, K_p)/\sigma_{ij}^2}. \tag{4.18}$$

where $\mathrm{Var}(\epsilon_0)$ represents the uncertainty in the scaling factor.

4.7 Probability Maps

The results of the matched-filter analysis are displayed in greyscale form as a function of the projected orbital velocity K_p, and the relative strength of the reflected signal, i.e. $\log(\epsilon_0) = \log(f_p/f_*) = \log(p(R_p/a)^2)$. The relative probabilities of the fits to the data for different values of the free parameters R_p/a and K_p are given by

$$P(K_p, R_p/a) \propto \exp(-\chi^2/2), \tag{4.19}$$

where

$$\chi^2 = \sum_{i,j} \frac{(D_{ij} - (R_p/a)^2 H(v_i, \phi_j, K_p))^2}{\sigma_{ij}^2}. \tag{4.20}$$

The probabilities are normalised to the most likely value in the map, such that the greyscale denotes the probability relative to the best-fit model, increasing from 0 (white) to 1 (black). A typical probability map is shown at Fig. 4.12, and demonstrates the recovery of a simulated planet signal. The maps are of similar content and form to the prior probability maps generated in Chapter 3.3.

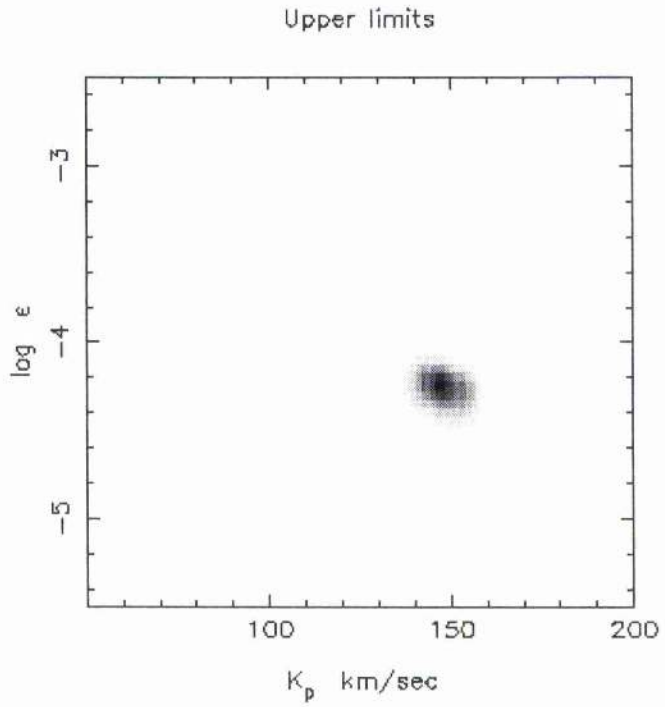

Figure 4.12: Relative probability map of model parameters K_p and $\log(\epsilon_0) = \log(p(R_p/a)^2)$ for a simulated planet signature input into the HD75289 data (Fig. 4.11) so as to return an unambiguous detection. In this case the planet was assigned a grey albedo $p = 0.4$, radius $R_p = 1.6\ R_{Jup}$ and an orbital inclination of 80 °.

The synthetic planet signal appears as a compact, dark feature at $K_p = 147$ km s^{-1} and $\log(\epsilon_0) = -4.22$, i.e. $\epsilon_0 = 6 \times 10^{-5}$. Given the assigned input parameters, we would expect the feature to be recovered at $\log(\epsilon_0) = -4.02$. The fact that it doesn't indicates that the result needs to be calibrated correctly, as detailed later in Chapter 4.8, but before that we must assess how confident we are of the detection.

Confidence of detection

The matched-filter analysis tells us that the most probable combination of orbital velocity and planet radius yields an improvement $\Delta\chi^2 = 40.4$ with respect to the value obtained assuming no planet is present. To set an upper limit on the strength of the planet signal, or to assess the likelihood that a candidate detection is spurious, we need to compute the probability of obtaining such an improvement in χ^2 by chance alone. In principle this

could be done using the χ^2 distribution for 2 degrees of freedom. In practice, however, the distribution of pixel values in the deconvolved residual profiles has extended non-gaussian tails that demand a more cautious approach.

Rather than relying solely on formal variances derived from photon statistics, we use a "bootstrap" procedure to construct empirical distributions for confidence testing, using the data themselves. In each of 3000 trials, we randomize the order in which different nights of observation were secured, we then randomise the order in which the observations were secured within each night. The re-ordered observations are then associated with the original sequence of dates and times. This ensures that any contiguous blocks of spectra containing similar systematic errors remain together, but appear at a new phase. Any genuine planet signal present in the data is, however, completely scrambled in phase. The re-ordered data are therefore as capable as the original data of producing spurious detections through chance alignments of blocks of systematic errors along a single sinusoidal path through the data. We record the least-squares estimates of $\log(\epsilon_0)$ and the associated values of χ^2 as functions of K_p in each trial.

The percentage points of the resulting bootstrap distributions are shown as contours in Fig. 4.13. From bottom to top, these contours give the 68.4% 95.4% 99.0% and 99.9% bootstrap upper limits on the strength of the planet signal, subject to calibration (see below). The 99.9% contour, for example, represents the value of $\log(\epsilon_0)$ that was only exceeded in 3 of the 3000 trials at each K_p.

4.8 Calibrating the matched-filter analysis

The purpose of incorporating a simulated planet signature into our analysis is two-fold. First, it allows us to ensure that any planetary signal, real or simulated, is maintained through the template subtraction and deconvolution procedures and can be recovered during the subsequent matched-filter analysis. In doing so we can measure the degree to which any simulated signal is attenuated and infer that any real planetary signal would suffer a similar fate. Second, by using a suitable calibration factor, we can ensure that the matched-filter detection for the simulated planet, appears at the expected position in the resulting $\log(\epsilon_0)$ vs. K_p probability map. Thus any potential detections within the real data would be suitably compensated for losses imposed by the full extraction and analysis

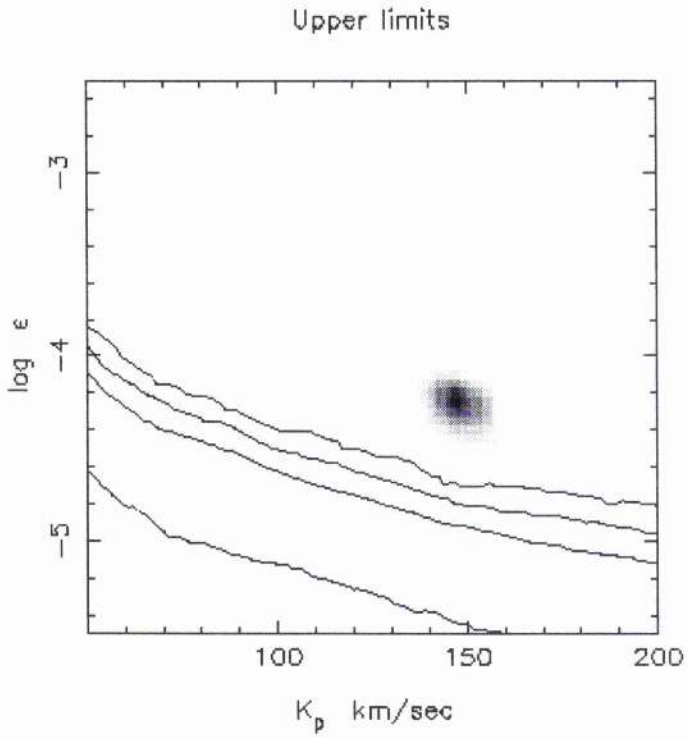

Figure 4.13: As for Fig. 4.12, but with the results of the bootstrap trials expressed as confidence levels at which candidate detections can be ruled out as being caused by spurious alignments of non-Gaussian noise features. From top to bottom, they show the 99.9%, 99.0%, 95.4% and 68.4% confidence limits. The simulated planet signature in this example, is detected well above the 99.9% confidence level.

process. As a consequence, it must be noted that any required correction would reduce the confidence to which we can apply upper limits on the strength of signal, since these are directly linked to any potential loss through the analysis.

Choice of planetary template

The choice of stellar spectrum to mimic the reflected-light signal depends on the orbital parameters of the target system. As the planet is in motion around its host, the spectral line broadening it sees is different to that we would observe. For example, a planet whose orbital period is tidally locked to the rotation of the star would not see that rotation, and broadening of the spectral lines would therefore be dominated by convective motions on the star's surface. As a result, we would need to use a star with a lower $v \sin i$ than

the host star to mimic the reflected component from the surface of the planet. We can however, make an prior estimate of the reflected $v \sin i$, using the known parameters of the target system (Appendix A.1) to conduct Monte Carlo trials similar to those detailed in Chapter 3. Given the stellar $v \sin i$, orbital period, and assuming the stellar rotation axis is perpendicular to the orbital plane, the trials identify the most likely line-width of the reflected spectrum. This prediction is then used to choose an additional stellar target to observe, which has a spectral type similar to that of the planet's host but exhibits a more appropriate $v \sin i$. The spectrum of that star will then be used to construct the planet template, as described in Chapter 4.8.1.

We mentioned earlier that the reflected-light signal is modelled as a time sequence of Gaussians with appropriate velocities and relative amplitudes according to Eqn. 4.14. The variable factor we use to calibrate the strength of the detected signal is the equivalent width (W_*) of the stellar component of the composite line profile. By deconvolving the planet template spectrum with a list of the relative strengths of its spectral lines, we obtain a composite line profile exhibiting a broadening function that is representative of all the lines recorded in the spectrum. By fixing the known $v \sin i$ of the planetary template, W_* controls the effective depth of the Gaussian model and can be varied to match the data. In effect, this allows us to control the relative brightness of any detection and ensure that simulated planet signals appear at the expected level. Any reduction in the strength of the simulated signal during the various processes would manifest itself as a reduction in the $\log(\epsilon_0)$ scaling factor, and appear fainter than expected. In the subsequent analyses of τ Bootis and HD75289, we find a 10 - 15% signal loss, primarily as a result of the PCA noise-reduction. Once the sources of signal loss have been identified and quantified, we can apply the correction to W_* and re-run the matched-filter analysis. We make the assumption that any genuine reflected-light signal would undergo a similar loss, thus in calibrating the simulated planet we can be sure that any genuine detection in the real data will appear at the correct relative brightness.

4.8.1 Construction of the simulated planet signature

The simulation procedure simply consists of shifting and scaling the spectrum of the planet template according to the orbit and phase function, co-multiplying it by an appropriate geometric albedo spectrum, and adding it to the observed data. We try to ensure a strong

signal by adopting geometric albedo and planetary radius values greater than expected by theory, in order to generate an input signal strong enough to return an unambiguous detection. As we found in Fig. 4.11, the synthetic signal appears in the resulting time-series of deconvolved line profiles as a dark sinusoidal feature crossing from right to left between phases 0.25 and 0.75. The feature is detected by the matched-filter analysis and recovered within the relative probability map of model parameters K_p and $\log(\epsilon_0) = \log p(R_p/a)^2$, as shown at Fig. 4.13.

If we combine the recovered K_p with the results of radial velocity studies, we obtain the inclination of the system and hence the true mass of the planet. Furthermore, once calibrated to the correct level, the ϵ_0 of any detection will allow us to constrain the $p\sqrt{R_p}$ measure of the orbiting planet. Given a theoretical radius, we can use the location of any feature or a given confidence level to identify the corresponding grey geometric albedo. Alternatively, given a geometric albedo model, we can identify the corresponding radius.

4.8.2 Calibrating non-grey albedo models

The meaning of ϵ_0 is straight forward with a grey albedo spectrum, however, problems arise when we wish to test how well a given non-grey albedo spectrum fits the data, such as the Sudarsky, Burrows & Pinto (2000) models discussed in Chapter 2.2.4. In this situation, the weighting factors (w_i) used to attenuate the lines in the deconvolution mask (Eqn. 4.7) are modified to reflect the wavelength dependence of the chosen albedo model. As we have now chosen to fix $p(\lambda)$, we can replace ϵ_0 with $(R_p/a)^2$ as the scaling factor in Eqn. 4.17. An accurate calibration also requires that we apply the same wavelength dependence to the spectrum of the fake planet template that is added prior to processing the data. The basis function G is rescaled to become $G' = \hat{p}G$, where $\hat{p}$ is an appropriately weighted geometric albedo, and is attenuated as before, using Eqn. 4.15.

After injecting the desired artificial planet signal into the data, we are then in a position to deconvolve the synthetic data with a modified line-list, weighted by the same albedo model as the planet template. We then conduct a matched-filter analysis on the simulated data, to identify the correct W_* (Eqn. 4.14) that recovers the expected value of R_p/a at the appropriate K_p. With the geometric albedo fixed, the probability maps allow us to place upper limits on the radius of the planet in question.

4.8.3 False alarm probabilities

It is important to note that the bootstrap contours only give the false-alarm probability (FAP) if the value of K_p is known in advance, which is generally not the case. The true false-alarm probability is greater, being the fraction of the 3000 bootstrap trials where spurious peaks at any possible value of K_p can exceed the $\Delta\chi^2$ of the candidate. Typically, the range of K_p investigated spans from 30 km s^{-1} (lower limit to matched-filter analysis) to v_p, where v_p is the orbital velocity of the planet as determined from RV measurements.

In practice, however, we are more likely to believe that a feature detected near the peak of the prior probability distribution for K_p is genuine, than if the feature appeared at a velocity that was physically implausible given our existing knowledge of the system parameters. We are therefore able use our prior estimates of K_p, as determined in Chapter 3, to weight the FAP using the following Bayesian approach.

Once the data are calibrated, the bootstrap contours give the conditional likelihood of obtaining the data D at a given K_P, i.e. $P(D|K_p)$. We use the prior probability distributions for K_p to determine the joint (weighted) probability,

$$P(D, K_P) = P(D|K_p)P(K_p). \tag{4.21}$$

We calculate $P(D, K_P)$, for the 3000 bootstrap trials, by selecting the maximum value from each trial of the quantity

$$\ln P(D, K_p) = \ln P(K_p) + \frac{\Delta\chi^2}{2}, \tag{4.22}$$

with the resulting trial distribution allowing us to calculate the weighted (posterior) FAPs.

4.9 Summary

Spectroscopic refected-light studies offer a unique route to achieving the first direct detection of an extrasolar planet. Due to the small separation and high contrast between the planet and its stellar host, we have had to develop sophisticated routines to carefully extract and identify any reflected-light signature present. In this chapter, we have described in some detail the steps required to help us achieve a successful detection. As this detail has been quite extended, and as many of the ideas are a little complex, we have provided

a graphical overview of the processes involved, Fig. 4.14, in the hope that it might pull together the preceeding discussion.

The survival of simulated planet signals through the process suggests that, in theory, we should be able to detect the reflection of starlight from the surface of a Pegasi planet. That is, assuming the atmosphere surrounding the planet behaves in a similar way to the planets in our own Solar system. The existence of these objects was unexpected by conventional theories of planet formation, and their atmospheric nature may prove equally unexpected. Nevertheless, the results of previous reflected-light studies (Collier Cameron et al. 2002), combined with the following studies of τ Bootis and HD75289, should act to improve our knowledge of these close-orbiting planets, about which very little is currently known.

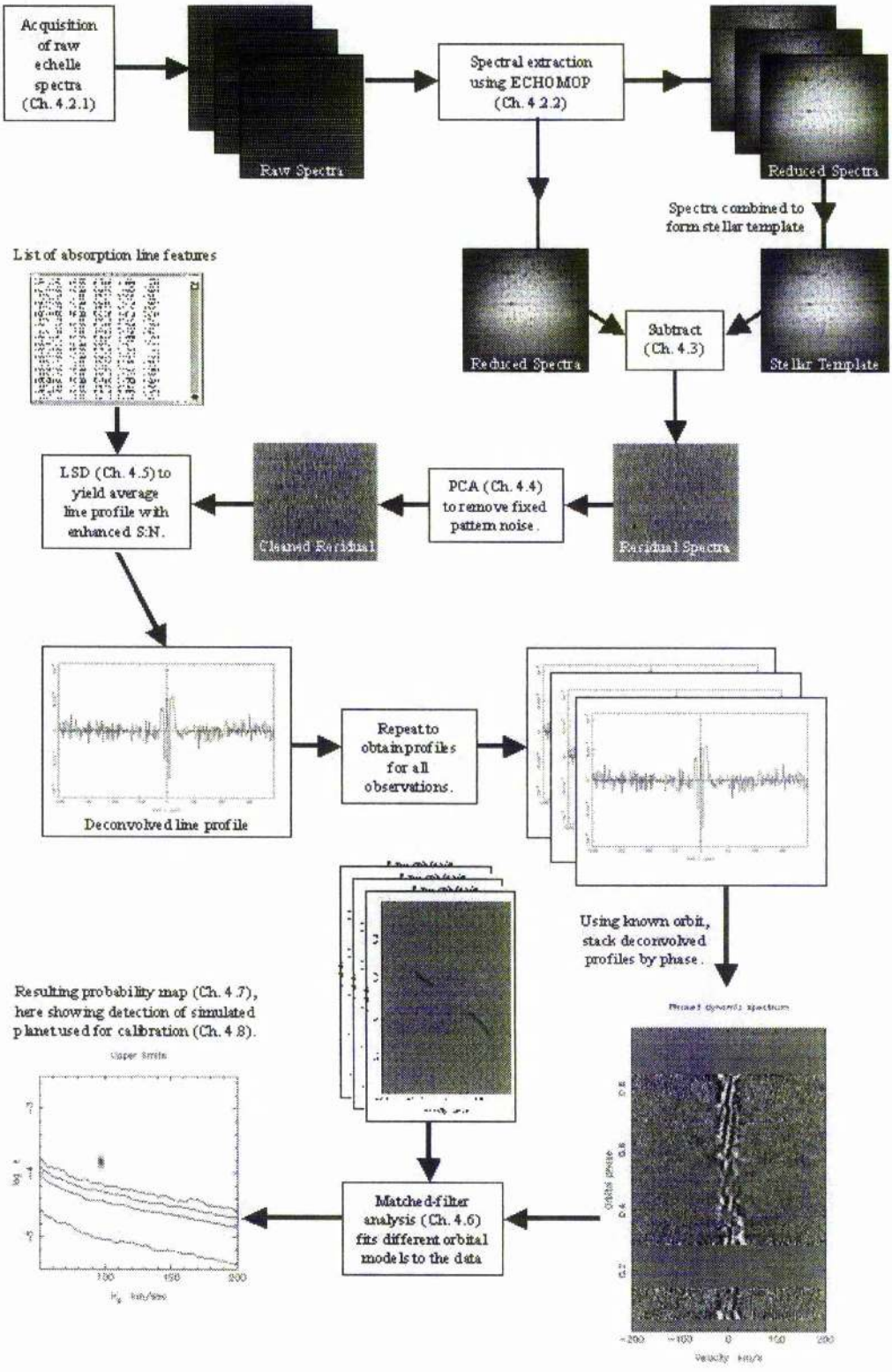

Figure 4.14: Overview of method to extract a reflected-light signature

CHAPTER 5

A new upper limit on the reflected starlight from τ Bootis b

This chapter summarises the contents of a paper, authored by myself and recently published in MNRAS (Leigh et al. 2003a), presenting work carried out in conjunction with Andrew Collier Cameron, Keith Horne, Alan Penny and David James, all of whom were cited as co-authors.

5.1 Introduction

Two years after the discovery of a planetary companion to 51 Pegasi by Mayor & Queloz (1995) came the identification of a similar object orbiting the F7V star τ Bootis (Butler et al. 1997). The discovery of objects with extremely short orbital periods (< 5 days) was wholly unexpected, but with 19 of the 110 known extrasolar planets orbiting at less than 0.1 AU from their parent stars, these Pegasi planets make up a significant proportion of the current sample.

Shortly after the τ Bootis b detection, two teams (Charbonneau et al. 1999; Collier Cameron et al. 1999) initiated a spectroscopic search for the reflected light component of the orbiting planet. Charbonneau et al. (1999) conducted 3 nights observation in March 1997 using the HIRES échelle spectrograph mounted on the KeckI 10m telescope on Mauna Kea, Hawaii. Although the restricted spectral range 465.8 - 498.7 nm provided a non detection, the signal-to-noise ratio (S:N $\sim$ 1500) was sufficient to impose a relative reflected flux limit $f_p/f_* < 8 \times 10^{-5}$ for a planet of inclination $i \geq 10°$, assuming a grey albedo reflection of the stellar spectrum. This implies a geometric albedo limit $p < 0.3$ over the spectral range investigated, assuming a planetary radius of 1.2 R_{Jup}. Collier Cameron et al. (1999) obtained 10 nights of data during 1998 and 1999, with the Utrecht Échelle Spectrograph

(UES) on the 4.2 m William Herschel telescope (WHT). By using a least-squares deconvolution (LSD) technique (Donati et al. 1997) on $\sim$ 2300 spectral lines in the range 385 - 611 nm, they identified a *probable* reflected-light feature with $f_p/f_* \sim 7.8 \times 10^{-5}$. This detection indicated an orbital velocity amplitude $K_p = 74 \pm 3$ km s^{-1} which, when combined with the planet's orbital velocity $V_p = 152$ km s^{-1}, suggested an inclination for the system $i = 29°$ and a radius $R_p = 1.8\ R_{Jup}$, assuming a grey geometric albedo $p = 0.55$. A bootstrap Monte Carlo analysis gave a 5% probability that the feature was an artefact of noise. Subsequent observations over 7 nights in March-May 2000, however, failed to confirm the detection (Collier Cameron et al. 2001).

Here we report the results of a new, deep search for the reflected light signal from τ Bootis b, using the techniques described in Chapter 4 to conduct a full re-analysis of the WHT data, combining all 17 nights of échelle spectra obtained during the 1998, 1999 and 2000 observing seasons.

5.2 System Parameters

τ Bootis (HD 120136, HR 5185) is a late-F main sequence star with parameters as listed in Appendix A.1. High precision radial velocity measurements over a period of 9 years were used to identify a planetary companion (Butler et al. 1997) whose properties (as determined directly from the radial velocity studies or inferred using the estimated stellar parameters) are summarised in Appendix A.2.

5.2.1 Rotational broadening

The rotational broadening of the direct starlight and chromospheric Ca II H & K emission flux suggest that the star's rotation appears to be synchronised with the orbit of the planet (Baliunas et al. 1997; Henry et al. 2000a). In a tidally locked system there is no relative motion between the surface of the planet and the surface of the star, so the planet will reflect a non-rotationally broadened stellar spectrum, with typical line widths dominated by turbulent velocity fields in the stellar photosphere. These motions were estimated by Baliunas et al. (1997) to be of the order $\sim$ 4 km s^{-1}. Any absorption lines attributed to the planet's atmosphere are thus likely to be much narrower than the stellar lines.

5.2.2 Orbital Inclination

In the first instance we can rule out inclinations $i > 80°$ due to the absence of transits in high-precision photometry (Henry et al. 2000b). Furthermore, we found in Chapter 3 that if we assume the star's rotation to be tidally locked to the planet's orbit, and that the stellar rotation axis is perpendicular to the orbital plane, then we can use the projected equatorial rotation speed of the host star $v \sin i = 14.9 \pm 0.5$ km s^{-1} (Henry et al. 2000b) and its rotation period to loosely constrain the orbital inclination to $i \sim 40°$. We would thus expect a projected orbital velocity amplitude close to $K_p \sim 100$ km s^{-1}.

5.3 Observations

We observed τ Bootis during 1998, 1999 and 2000 using the Utrecht Échelle Spectrograph on the 4.2 m William Herschel Telescope at the Roque de los Muchachos Observatory on La Palma. The detector was a single SITe 1 CCD array containing some 2048 × 2048 13.5-μm pixels. The CCD was centred at 459.6 nm in order 124 of the 31 g mm^{-1} échelle grating, giving complete wavelength coverage from 407.4 nm to 649.0 nm with minimal vignetting. The average pixel spacing was close to 3.0 km s^{-1}, and the full width at half maximum intensity of the thorium-argon arc calibration spectra was 3.5 pixels, giving an effective resolving power $R = 53000$.

Table 5.1 lists the journal of observations for the 17 nights of data which contribute to the analysis presented here. In the first year (1998) the stellar spectra were exposed between 100 and 200 seconds. For 1999 and 2000, the stellar spectra were exposed for between 300 and 500 seconds, depending upon seeing, in order to expose the CCD to a peak count of 40000 ADU per pixel in the brightest parts of the image. Following extraction, with a gain of 1.92, a 450s exposure yielded about 1.2×10^6 electrons per pixel step in wavelength in the brightest orders in typical (1 arcsec) seeing. We achieved this with the help of an autoguider procedure, which improves efficiency in good seeing by trailing the stellar image up and down the slit by ±2 arcsec during the exposure to accumulate the maximum S:N per frame attainable without risk of saturation. Note that the 450s exposure time compared favourably with the 53s readout time for the SITe 1 CCD in terms of observing efficiency, with the fraction of the time spent collecting photons above 90%. Following extraction, the S:N in the continuum of the brightest orders was typically

UTC start	Phase	UTC End	Phase	Exposures
1998 Apr 09 22:09:43	0.425	1998 Apr 10 05:37:05	0.519	107
1998 Apr 10 22:04:40	0.726	1998 Apr 11 06:20:54	0.830	113
1998 Apr 11 22:09:28	0.029	1998 Apr 12 05:58:44	0.127	81
1998 Apr 13 23:02:54	0.644	1998 Apr 14 05:37:05	0.733	33
1999 Apr 02 22:06:45	0.493	1999 Apr 03 06:08:47	0.594	25
1999 Apr 25 21:43:17	0.441	1999 Apr 26 05:31:59	0.539	40
1999 May 05 21:56:59	0.463	1999 May 06 04:51:57	0.550	60
1999 May 25 20:59:45	0.488	1999 May 26 03:56:18	0.576	51
1999 May 28 20:52:23	0.390	1999 May 29 03:04:35	0.467	47
1999 Jun 04 20:22:34	0.497	1999 Jun 05 00:07:23	0.548	23
2000 Mar 14 23:14:49	0.271	2000 Mar 15 06:54:52	0.366	48
2000 Mar 15 22:51:55	0.567	2000 Mar 16 06:49:04	0.669	45
2000 Mar 24 22:21:55	0.278	2000 Mar 25 06:47:50	0.385	34
2000 Apr 23 20:38:59	0.311	2000 Apr 24 05:07:31	0.420	45
2000 Apr 24 20:58:32	0.619	2000 Apr 25 05:14:11	0.724	57
2000 May 13 20:47:01	0.349	2000 May 14 03:12:08	0.434	41
2000 May 17 20:24:14	0.557	2000 May 18 03:52:37	0.649	43

Table 5.1: Journal of observations. The UTC mid-times and orbital phases are shown for the first and last spectral exposures secured on each night of observation. The number of exposures is given in the final column.

1000 per pixel step in wavelength.

5.4 Data Analysis

One-dimensional spectra were extracted from the CCD frames using an automated pipeline reduction system built around the Starlink ECHOMOP and FIGARO packages, described in more detail in Chapter 4.2.

The initial tracing of the échelle orders on the CCD frames was performed manually on the spectrum of τ Bootis itself, using exposures taken for this purpose without dithering the star up and down the slit. The automated extraction procedure then subtracted the bias from each frame, cropped the frame, determined the form and location of the stellar profile on each image relative to the trace, subtracted a linear fit to the scattered-light background across the spatial profile, and performed an optimal (profile and inverse variance-weighted) extraction of the orders across the full spatial extent of the object+sky region. Nightly flat-field balance factors were applied in the process using the 50 to 100 frames obtained at the start and end of each night of observations, using an algorithm that identified and rejected cosmic rays and other non-repeatable defects by comparing successive frames. Due to physical movement of the chip mounting between and during observation runs, it was found that the level of noise was reduced by the use of nightly flat-fields rather than master flat-fields for the entire years' observation. In all, 55 orders (orders 88 to 142) were extracted from each exposure, giving full spectral coverage from 407.4 to 649.1 nm with good overlap.

For a bright, cloudy model planet with $p = 0.4$ and $R_p = 1.2\ R_{Jup}$, we expect the flux of starlight scattered from the planet to be no more than one part in 18000 of the flux received directly from τ Bootis itself, even at opposition ($\alpha = 0$). In order to detect the planet signal, we first subtract the direct stellar component from the observed spectrum, leaving the planet signal embedded in the residual noise pattern. A detailed description of this procedure was given in Chapter 4.3. The planet signal consists of faint Doppler-shifted copies of each of the stellar absorption lines. After cleaning up any correlated fixed-pattern noise remaining in the difference spectra (see Chapter 4.4), we then create a composite residual line profile, by fitting to the thousands of lines recorded in each échellogram (Chapter 4.5). Finally we use a matched-filter analysis (Chapter 4.6)

to search for features in the time-series of composite residual profiles whose temporal variations in brightness and radial velocity resemble those of the expected reflected-light signature. For an assumed albedo spectrum $p(\lambda)$ and orbital velocity amplitude K_p, the fit of the matched-filter to the data yields a measure of $(R_p/a)^2$.

5.4.1 Analysis changes

In this new analysis of the τ Bootis data, I have made the following significant changes to the processing undertaken for the original Collier Cameron et al. (1999) paper -

(i) The inclusion of the year 2000 data, which adds seven night's data taken at optimally-illuminated orbital phases to the analysis.

(ii) Full re-extraction of all three year's data, again using optimal methods, and providing an increase in the spectral range by two échelle orders or $\sim$ 15 nm.

(iii) The use of nightly flat-field frames in the extraction routine, rather than the previous whole year flat-fields. Post extraction analysis shows a $\sim$ 4% reduction in noise.

(iv) Increases in computational processing power over the intervening years has allowed the analysis to be conducted on individual échelle frames, rather than having to co-add the spectra into groups of 4 prior to the deconvolution and matched-filter analysis.

(v) The inclusion of a Principal Component Analysis routine (PCA), as detailed in Chapter 4.4, to remove correlated fixed-pattern noise that was appearing in the difference spectra (i.e. the stellar template subtracted frames).

(vi) The use of a more stringent calibration technique, to quantify and correct for the fraction of the planetary signal lost during the stellar subtraction, deconvolution and PCA routines. With this we find shallower but more realistic upper limits than were stated by Collier Cameron et al. (2001), who assumed no loss of signal.

5.5 Calibrating the process

We verified that a faint planetary signal is preserved through the signal extraction process in the presence of realistic noise levels, by adding a simulated planetary signal to the

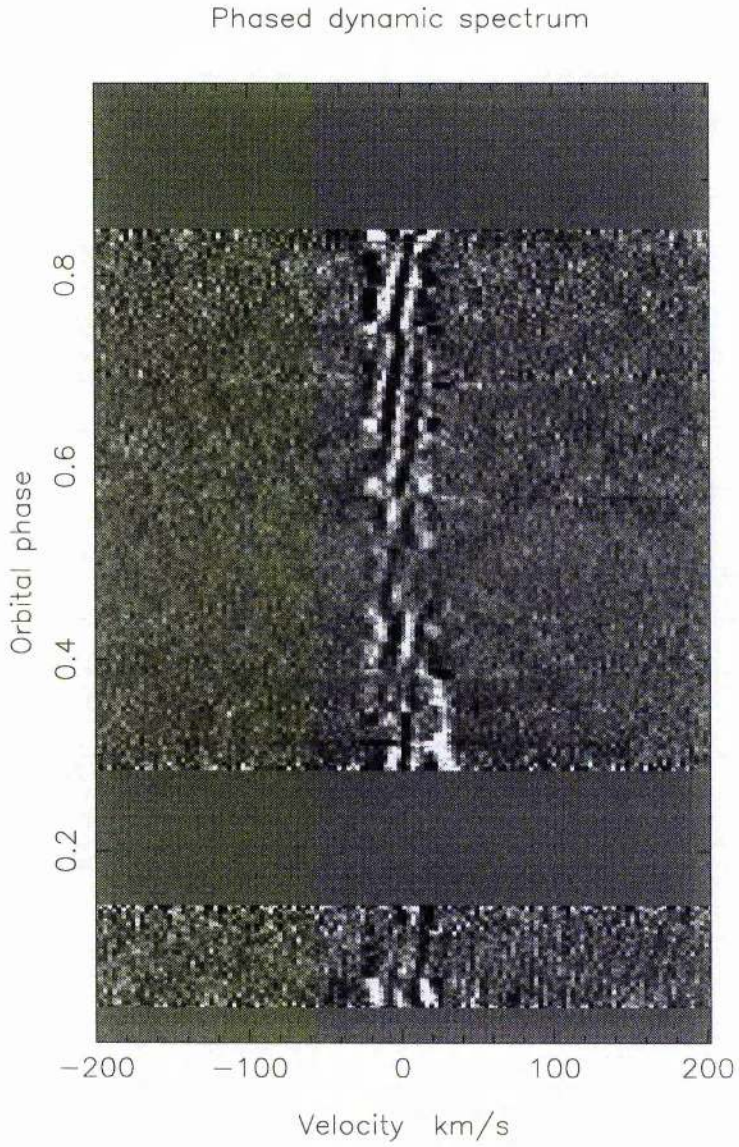

Figure 5.1: Time series of deconvolved profiles derived from the original WHT spectra, and secured over 17 night's observation in 1998, 1999 and 2000, but with the addition of a simulated planet signal at an inclination of 60°. The injected signal is that of a planet with geometric albedo $p = 0.5$, radius 1.4 R_{Jup} and appears as a dark sinusoidal feature crossing from right to left as phase increases and centred on the superior conjunction at phase 0.5.

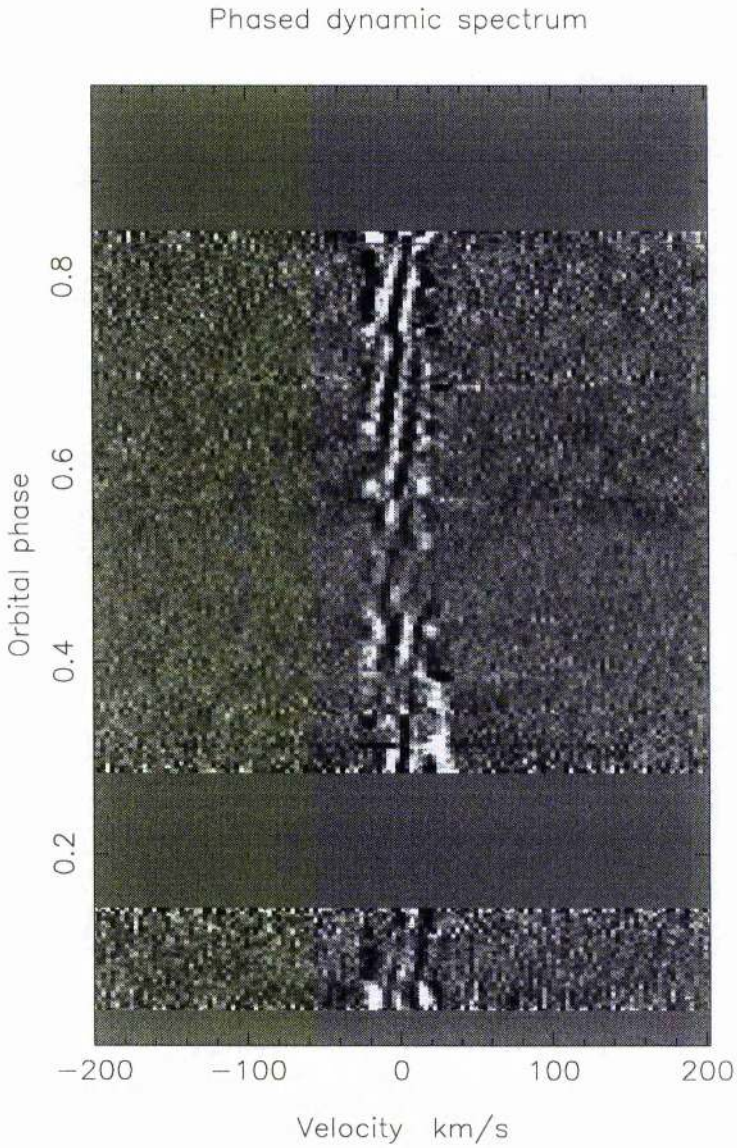

Figure 5.2: Time series of deconvolved profiles derived from the original WHT spectra, and secured over 17 night's observation in 1998, 1999 and 2000. The observations assume a grey albedo spectrum without the addition of a synthetic planet signal. The greyscale runs from black at -10^{-4} times the mean stellar continuum level, to white at $+10^{-4}$. The velocity scale is in the reference frame of the stellar host.

observed spectra. We also use the simulated signal to calibrate the strength of any detected signal in the original data (see Chapter 4.8). The simulations were based on the assumption that the planet's rotation is close to being tidally locked, always keeping the same face towards the star. The resulting broadening of the spectral lines is therefore dominated by convective motions on the star's surface, estimated at $\simeq 4$ km s^{-1} (Baliunas et al. 1997). For our simulations we chose to use the slowly rotating giant star HR5694, observed on several nights in 1999. HR5694 is a F7III spectral type of similar temperature and elemental abundance to τ Bootis, but with an estimated $v \sin i \simeq 6.4 \pm 1$ km s^{-1} (Baliunas et al. 1997), making it well suited to represent the reflected starlight.

For any assumed axial inclination, the phase angle and line-of-sight velocity are known at all times. The simulation procedure simply consists of shifting and scaling the spectrum of HR5694 according to the orbit and phase function, co-multiplying it by an appropriate geometric albedo spectrum, and adding it to the observed data. To ensure a strong signal we used a simulated planet of radius 1.4 R_{Jup} and wavelength-independent geometric albedo $p = 0.5$, which when viewed at zero phase angle should give a planet/star flux ratio $\epsilon_0 = f_p/f_* = 0.98 \times 10^{-4}$. We have chosen a planetary radius greater than that expected by theory so as to provide a simulated input signal strong enough to return an unambiguous detection.

The resulting time series of deconvolved line profiles, shown in Fig. 5.1, demonstrates how the simulated planet signal is recovered after the extraction process, with the planetary signal clearly visible as a dark sinusoidal feature crossing from right to left between phases 0.25 and 0.75. The weakening of the simulated planetary signature near quadrature is caused mainly by the phase function. The signal is further attenuated near quadrature by the way in which the templates are computed: since the planet signature is nearly stationary in this part of the orbit, some of the signal will be removed along with the stellar profile if many observations are made in this part of the orbit.

Figs. 5.1 and 5.2 both show a "barber-pole" pattern of distortions in the residual stellar profiles at low velocities. The phase variation in these undulations appears consistent with sub-pixel shifts in the position of the spectra with respect to the detector over the course of the night. Fortunately they only affect a range of velocities at which the planet signature would in any case be indistinguishable from that of the star.

The signal of the synthetic planet is recovered, as in Fig. 5.3, as a dark compact

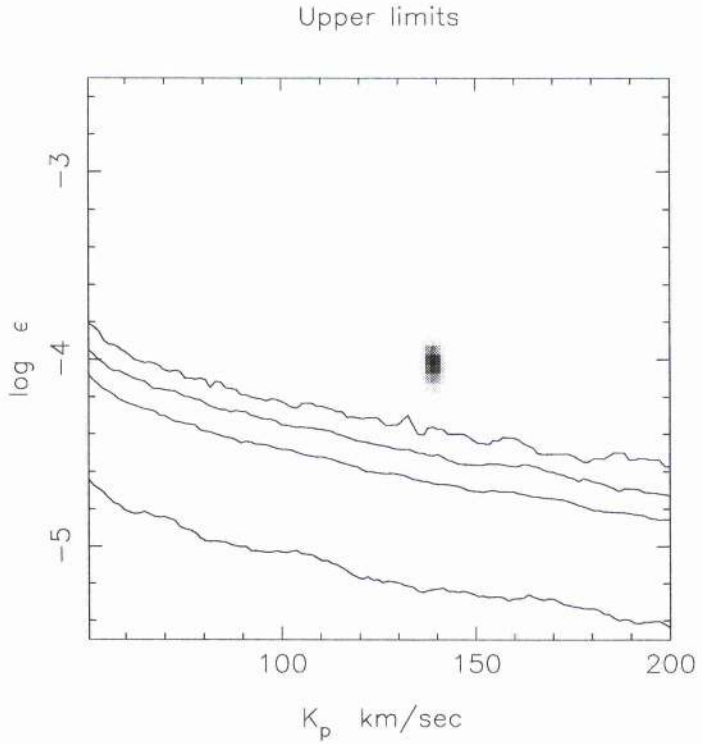

Figure 5.3: Relative probability map of model parameters K_p and $\log(\epsilon_0) = \log p(R_p/a)^2$ for a simulated planet signature with grey albedo $p = 0.5$, $R_p = 1.4\ R_{Jup}$ and orbital inclination of 60 °. The contours show the confidence levels at which candidate detections can be ruled out as being caused by spurious alignments of non-Gaussian noise features. From top to bottom, they show the 99.9%, 99.0%, 95.4% and 68.4% confidence limits. The synthetic planet signature is detected well above the 99.9% confidence limit.

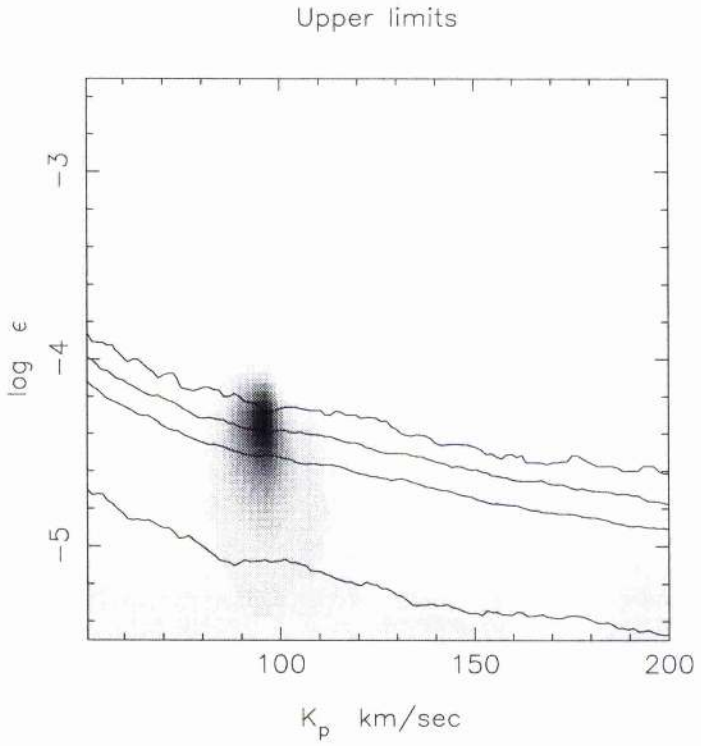

Figure 5.4: Relative probability map of model parameters K_p and $\log(\epsilon_0) = \log p(R_p/a)^2$, derived from the WHT/UES observations of τ Bootis, assuming a grey albedo spectrum. The greyscale denotes the probability relative to the best-fit model, increasing from 0 for white to 1 for black. A broad candidate feature appears close to the 99.0% confidence contour, with projected orbital velocity amplitude $K_p = 97$ km s^{-1}.

feature at $K_p = 139$ km s^{-1} and $\log(\epsilon_0) = -4.01$, i.e. $\epsilon_0 = 0.98 \times 10^{-4}$. This most probable combination of orbital velocity and planet radius yields an improvement $\Delta\chi^2 = 84.6$ with respect to the value obtained assuming no planet is present (Fig. 5.5). We used the "bootstrap" procedure described in Chapter 4.7 to assess the likelihood that the candidate detection was spurious, by computing the probability of obtaining such an improvement in χ^2 by chance alone. In each of 3000 trials, the 893 spectra obtained over 17 nights were randomly re-ordered within the original sequence of dates and times. With any genuine planet signal now completely scrambled in phase, the re-ordered data are therefore as capable as the original data of producing spurious detections through chance alignments of blocks of systematic errors along a single sinusoidal path through the data. We record the least-squares estimates of $\log(\epsilon_0) = \log p(R_p/a)^2$ and the associated values of χ^2 as functions of K_p in each trial.

The percentage points of the resulting bootstrap distribution are shown as contours in Figs. 5.3 and 5.4. The 99.9% contour, for example, represents the value of $\log(\epsilon_0)$ that was only exceeded in 3 of the 3000 trials at each K_p.

5.6 Results

The results of this analysis appear on the relative probability map of model parameters K_p and $\log(\epsilon_0) = \log p(R_p/a)^2$, shown at Fig. 5.4. The calibrated confidence levels allow us to achieve our primary aim of constraining the $p\sqrt{R_p}$ measure of the planet. However, there exists a significant candidate feature close to the 99% level that requires further investigation. In the subsequent discussion, we therefore also explore the possibility that this feature could represent a genuine planetary detection.

If the feature were genuine, its projected orbital velocity amplitude $K_p \simeq 97$ (± 10) km s^{-1} yields an orbital inclination of 37 (± 5)°. This would be consistent with the star's rotation being tidally locked to the planet's orbit and implies a mass for τ Bootis b of $M_p = 7.28(\pm 0.83)\ M_{Jup}$.

We emphasise that, although the feature appears very close to the peak of the prior probability distribution projected onto K_p, shown in Fig. 3.2, there remains a distinct possibility that the candidate detection is a consequence of spurious noise and as such we should proceed with caution.

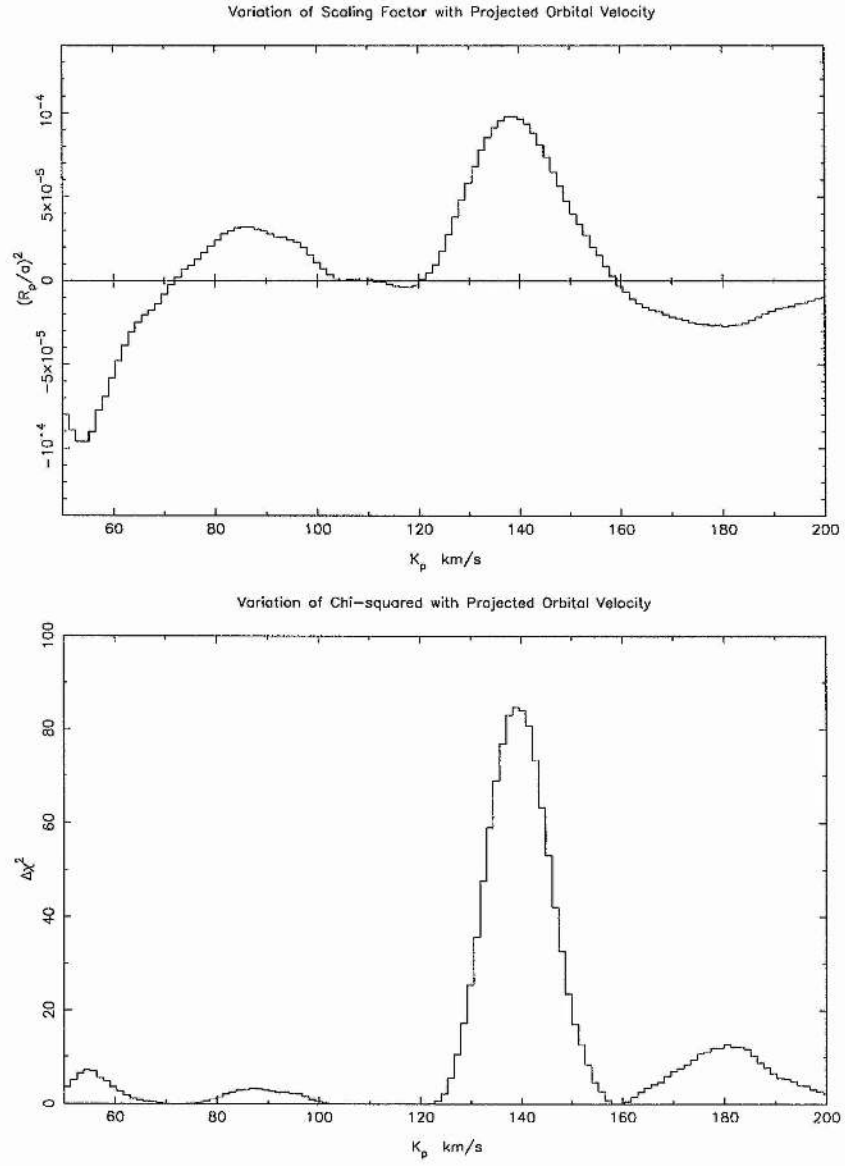

Figure 5.5: The upper panel shows the optimal scaling factor $(R_p/a)^2$ plotted against orbital velocity amplitude K_p, assuming a grey albedo spectrum for the simulated planet data. The lower panel shows the associated reduction $\Delta\chi^2 = 84.6$, measured relative to the fit obtained in the absence of any planet signal i.e. for $(R_p/a)^2 = 0$. Note that only positive values of $(R_p/a)^2$ are physically plausible.

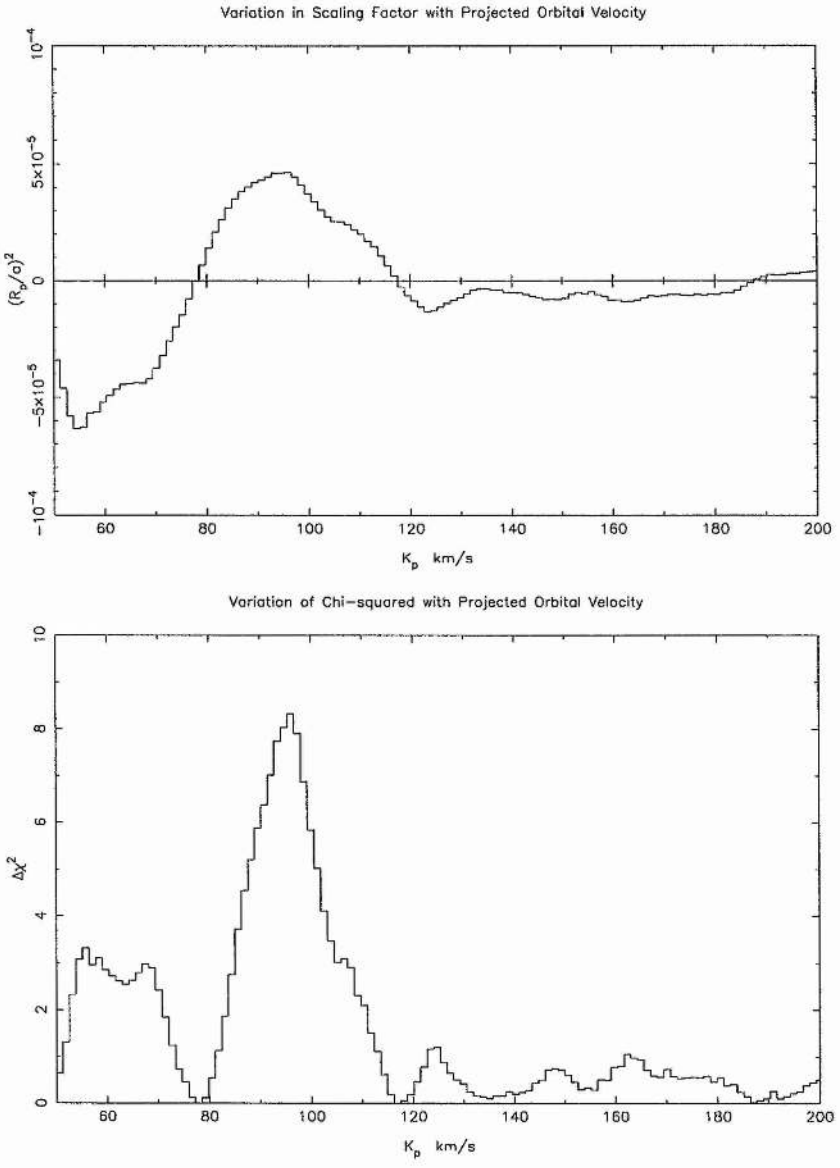

Figure 5.6: As for Fig. 5.5 but assuming a grey albedo spectrum for the original data without a simulated planet signal. The lower panel shows the associated reduction in $\Delta\chi^2 = 8.324$, measured relative to the fit obtained in the absence of any planet signal. The weak improvement in $\Delta\chi^2$ at $K_p = 60$ km s^{-1} corresponds to a negative value of $(R_p/a)^2$ and is therefore physically implausible.

False Alarm Probability	$\epsilon_0 = p\,(R_p/a)^2$	Upper Albedo Limit (p)
0.1 %	0.561 E-04	0.39
1.0 %	0.403 E-04	0.28
4.6 %	0.305 E-04	0.21

Table 5.2: Upper limits on the grey albedo for the atmosphere of τ Bootis b assuming a radius of 1.2 R_{Jup}. The upper limits are quoted for an assumed $K_p \simeq 94$ km s^{-1}, at the peak of the prior probability distribution for K_p determined in Chapter 3.

5.6.1 Upper limits on grey albedo

The grey albedo model assumes that at all times the planet/star flux ratio is independent of wavelength. For an assumed planetary radius we can thus use Eqn. 2.16 to constrain the geometric albedo. Table 5.2 lists the upper limits on the albedo at various levels of significance, for the planetary radius $R_p = 1.2\ R_{Jup}$ predicted by current theoretical models (Guillot et al. 1996; Burrows et al. 2000).

The contours in Fig. 5.4 produced by the bootstrap simulation constrain the maximum reflected flux ratio at opposition to $\epsilon_0 \leq 0.561 \times 10^{-4}$ at the 99.9 % confidence level, assuming a projected orbital velocity K_p at the peak of the prior probability distribution, i.e. $K_p \simeq 94$ km s^{-1}. This would limit the geometric albedo of the planet to $p \leq 0.39$. We note that this is a similar result to that obtained by Charbonneau et al. (1999) at the same inclination. Both studies assume a grey albedo, $R_p = 1.2\ R_{Jup}$, synchronous rotation of the star and hence a reflected version of the stellar spectrum with no rotational broadening. The candidate feature that appears in Fig. 5.4 would, if genuine, yield a grey geometric albedo of $p = 0.32$ (± 0.13) for a planet of this radius.

5.6.2 Upper limits on radius

Here we investigate how atmospheric albedo models can be incorporated into the signal analysis to place upper limits on the size of the planet. A non-grey albedo model is built into the formation of the least-squares deconvolved profile, by scaling the strengths of the lines in the deconvolution mask by a factor equal to the geometric albedo at each line's wavelength. The scale factor produced by the matched-filter analysis is then directly proportional to $(R_p/a)^2$ (see Eqn. 2.16) and is calibrated by injecting the signature of a planet of known radius with the specified albedo spectrum into the data. The method is described in detail in Chapter 4.8.

The theoretical models we consider here are those proposed by Sudarsky, Burrows & Pinto (2000) for a range of extrasolar giant planets, as described in Chapter 2.2.4.

Grey albedo model

At the most probable values in the prior distribution ($K_p \simeq 94$ km s^{-1}), assuming a grey albedo model of $p = 0.3$, the 0.1%, 1.0% and 4.6% upper limits on the planet/star flux ratio ϵ_0 correspond to upper limits on the planet radius, as detailed in Table 5.3. With a higher assumed geometric albedo, the planet's radius is more strongly constrained.

Our candidate planet signal yields an improvement $\Delta\chi^2 = 8.324$ over the model fit obtained assuming no planet signal is present (Fig. 5.6). We used the bootstrap simulations to determine the probability that a spurious feature with $\Delta\chi^2 > 8.324$ could be produced by a chance alignment of noise features in the absence of a genuine planet signal. As we discussed in the last chapter, the bootstrap contours only give the false-alarm probability if the value of K_p is known in advance, which is not the case here. The true false-alarm probability is greater, being the fraction of bootstrap trials where spurious peaks at any plausible value of K_p can exceed the $\Delta\chi^2$ of the candidate. If we assume that all values of K_p are equally likely in the range 50 km s^{-1} $< K_p <$ 162 km s^{-1}, the false-alarm probability is found to be 14.7%.

In practice, however, we are more likely to believe that a feature detected near the peak of the prior probability distribution for K_p is genuine, than if the feature appeared at a velocity that was physically implausible given our existing knowledge of the system

Albedo Model	False Alarm Probability	$(R_p/a)^2$	R_p/R_{Jup} Upper Limit
Grey	0.1%	1.87 E-04	1.37
$(p = 0.3)$	1.0%	1.34 E-04	1.16
	4.6%	1.02 E-04	1.01
Class V	0.1%	1.16 E-04	1.08
	1.0%	0.91 E-04	0.95
	4.6%	0.63 E-04	0.79
Class IV	0.1%	1.50 E-04	1.22
(Isolated)	1.0%	1.13 E-04	1.06
	4.6%	0.87 E-04	0.93

Table 5.3: Upper limits on planet radius for various albedo models. The limits are quoted for an assumed $K_p \simeq 94$ km s^{-1}, at the peak of the prior probability distribution for K_p, as determined in Chapter 3. Note that the results for the grey albedo model are given for a geometric albedo of $p = 0.3$. Radii for other grey model albedos can be obtained by dividing Column 4 by $\sqrt{p/0.3}$.

Albedo Model	K_p (km s^{-1})	R_p/R_{Jup}	$\Delta\chi^2$	FAP (Uniform Weight)	FAP (K_p Prior)
Grey ($p = 0.3$)	97 ($\pm$8)	1.24 ± 0.25	8.324	0.147	0.036
Class V	95 ($\pm$8)	1.08 ± 0.19	12.06	0.032	0.003
Class IV	90 ($\pm$8)	1.18 ± 0.20	9.227	0.092	0.032

Table 5.4: Projected orbital velocity peak, planet radius, $\Delta\chi^2$ and false-alarm probabilities (FAP) for the candidate feature, on the basis that it represents a genuine detection. The second FAP weights K_p in proportion to the prior probability density distribution (Fig. 3.2).

parameters. We can therefore use our prior estimation of K_p (see Chapter 3) to weight the false-alarm probabilty using the Bayesian approach described in Chapter 4.8.3. We find, as detailed in Table 5.4, that the false-alarm probability drops to 3.6% when prior knowledge of K_p is accounted for. For comparison, we find that a matched-filter analysis of the simulated planet data sees an improvement of $\Delta\chi^2 = 84.6$ above the value obtained assuming no planet signal is present. This is far greater than the $\Delta\chi^2 = 42.3$ produced at any K_p in the bootstrap trials. The false-alarm probability is therefore substantially less than one part in 3000, and as such the "detection" of the simulated signal is secure.

Class V model

The "Class V roaster" is the most highly reflective of the models published by Sudarsky, Burrows & Pinto (2000). It is characteristic of planets with $T_{eff} \geq 1500$ K and/or surface gravities lower than ~ 10 m s^{-2}, and as such is associated with lower mass planets, such as υ And b. The model predicts a silicate cloud deck located high enough in the atmosphere that the overlying column density of gaseous alkali metals is low, allowing a substantial

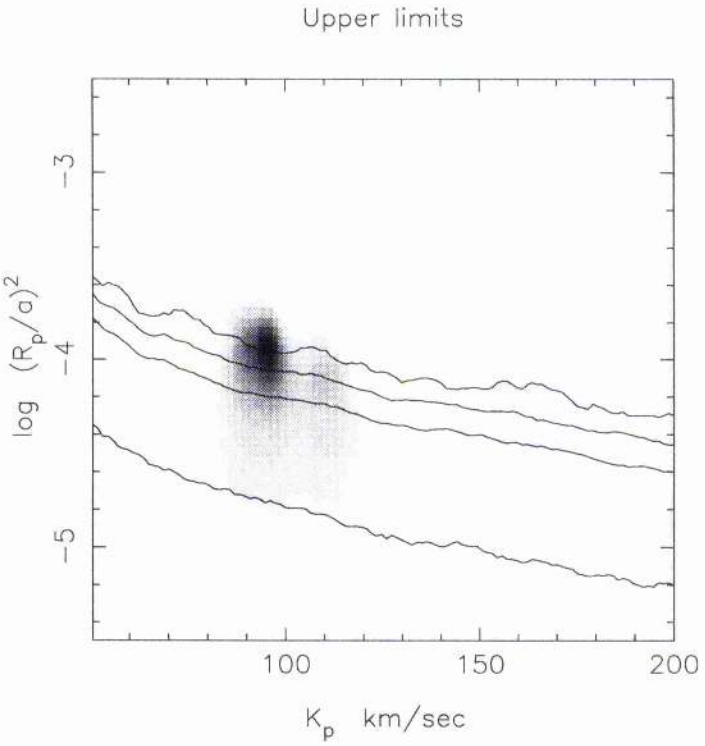

Figure 5.7: Relative probability map of model parameters K_p and $\log(R_p/a)^2$, derived from the WHT/UES observations of τ Bootis, assuming the albedo spectrum to be that of a class V roaster. The greyscale and contours are defined as in Fig. 5.3.

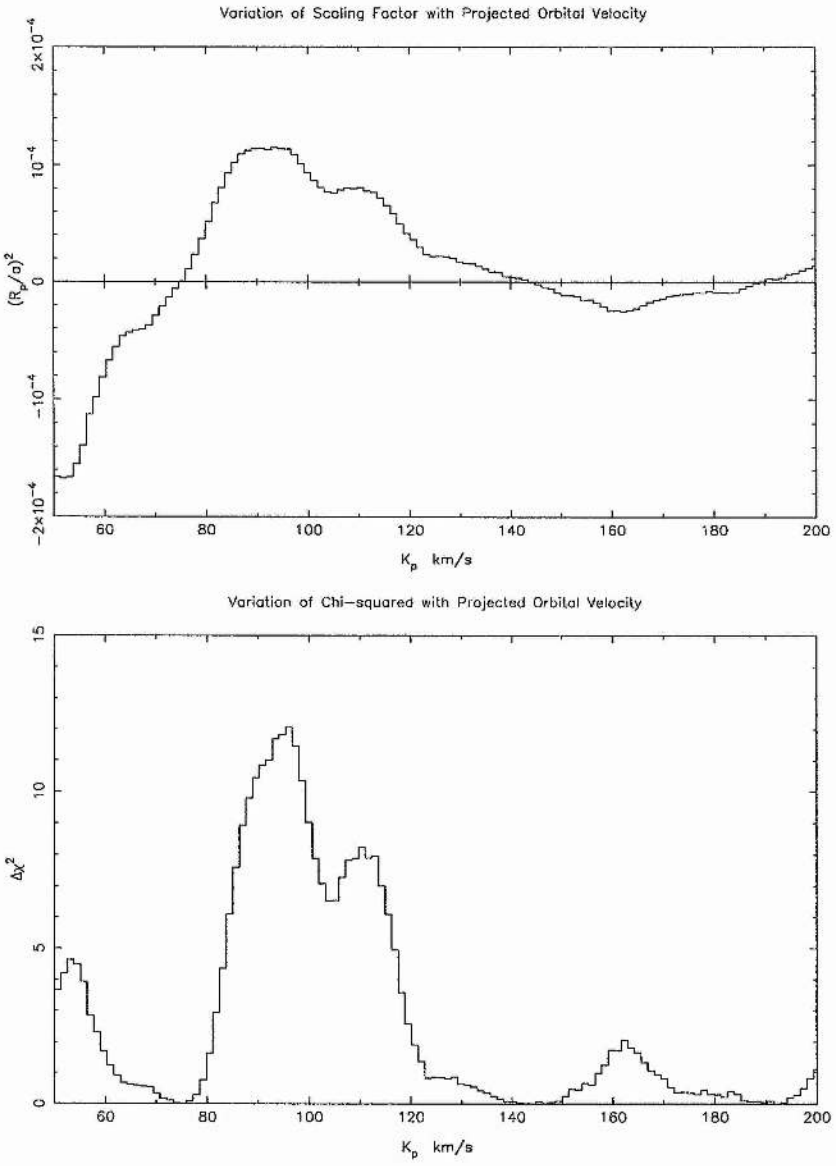

Figure 5.8: As for Fig. 5.5 but assuming a class V spectrum for the original data without a simulated planet signal.The lower panel shows the associated reduction in $\Delta\chi^2$ of 12.06, measured relative to the fit obtained in the absence of any planet signal.

fraction of incoming photons at most optical wavelengths to be scattered back into space. There remains, however, a substantial absorption feature around the Na I D lines, as shown in Fig. 2.14.

We carried out the deconvolution using the same line list as for the grey model, but with the line strengths attenuated using the class V albedo spectrum (see Chapter 4.5). We calibrated the signal strength, as described in Chapter 4.8.2, by injecting an artificial planet signature consisting of the spectrum of HR5694, attenuated by the class V albedo spectrum and scaled to the signal strength expected for a planet with $R_p = 1.4\ R_{Jup}$.

The form of the class V probability map, as shown in Fig. 5.7 is similar to that encountered for the grey albedo spectrum. The resulting upper limits on the planet radius are detailed at Table 5.3, with the corresponding false-alarm probabilities listed in Table 5.4. We find the feature produces a local probability maximum near $K_p = 95$ km s^{-1}, with an improvement in $\Delta\chi^2$ over the grey albedo model of 12.06, as shown in Fig. 5.8. This improvement translates to a reduced FAP (unweighted) of 3.2%, however, the position of the best-fitting K_p matches the prior probability maximum of $K_p = 94$ km s^{-1} so closely that the overall FAP is 0.3%, substantially lower than that obtained for the grey albedo case. This suggests strongly that the features in the data that give rise to this signal originate predominantly at blue wavelengths. If the candidate feature we observe were genuine, it would indicate a class V planet of radius 1.08($\pm$0.19) R_{Jup}, which is in line with current theory (Guillot et al. 1996; Burrows et al. 2000).

Isolated class IV model

The "Class IV" models of Sudarsky, Burrows & Pinto (2000) have a more deeply-buried cloud deck than the class V models and are probably more closely applicable to τ Boo b given its relatively high surface gravity. The resonance lines of Na I and K I are strongly saturated, with broad damping wings due to collisions with H_2 extending over much of the optical spectrum (Fig. 2.14).

We used the procedures described in Chapter 4 to deconvolve and back-project the data assuming an isolated class IV albedo spectrum. Although this model does not take full account of the effects of irradiation on the atmospheric temperature-pressure structure, it is a useful compromise between the class V models and the very low albedos found with

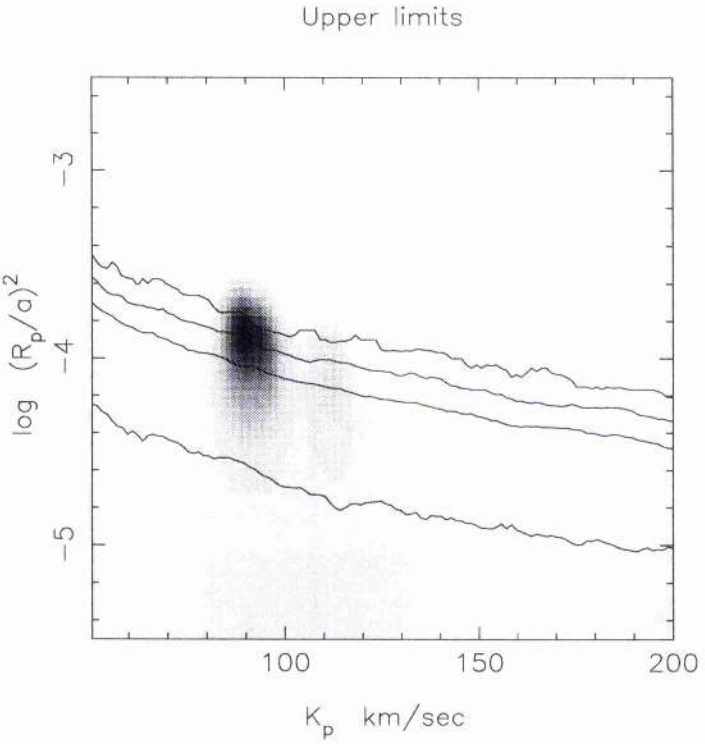

Figure 5.9: Relative probability map of model parameters K_p and $\log(R_p/a)^2$, derived from the WHT/UES observations of τ Bootis, assuming the albedo spectrum to be that of an "isolated" class IV gas giant. The candidate feature, if genuine, corresponds to the detection of a 1.18($\pm$0.20) R_{Jup} planet. The greyscale and contours are defined as in Fig. 5.3.

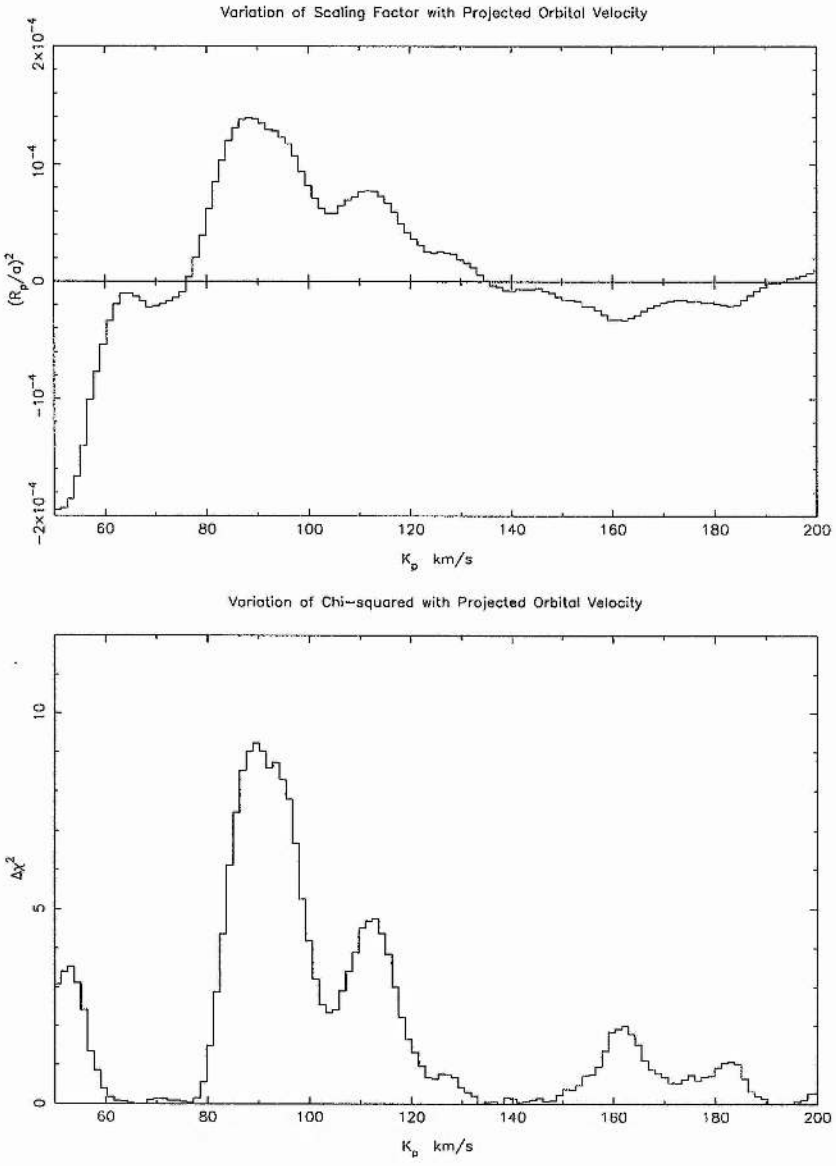

Figure 5.10: As for Fig. 5.5 but assuming a class IV "isolated" spectrum for the original data without a simulated planet signal. The lower panel shows the associated reduction in $\Delta\chi^2$ of 9.227, measured relative to the fit obtained in the absence of any planet signal.

irradiated class IV models. The resulting time-series of deconvolved spectra is noisier than the class V and grey-albedo versions, because lines redward of 500 nm contribute little to the deconvolution.

The probability map (Fig. 5.9) derived from the bootstrap matched-filter analysis again shows a marginally significant candidate reflected-light feature, but for this albedo model the peak of the distribution is shifted to $K_p = 90$ km s^{-1}. The fit to the data is slightly better than in the grey albedo case, giving an improvement of $\Delta\chi^2 = 9.227$ over the no-planet hypothesis (see Fig. 5.10). The bootstrap analysis returns an unweighted false-alarm probability of 9.2%, but the displacement of the most probable value of K_p (90 km s^{-1}) away from the prior probability maximum at $K_p = 94$ km s^{-1}, means the overall Bayesian FAP is 3.2%, slightly lower than in the grey albedo case.

The increase in noise associated with the extraction of the class IV simulation produces more loosely constrained upper limits on the planetary radius, as set out in Table 5.3. We note that if the candidate feature were genuine, it would indicate a class IV planet of radius 1.18($\pm$0.20) R_{Jup}, still in line with current expectations (Guillot et al. 1996; Burrows et al. 2000).

5.7 Conclusion

We have re-analysed the WHT échelle spectra obtained for the F7V star τ Bootis during 1998, 1999 and 2000. By assuming that

(i) the rotation of τ Bootis is tidally locked to the orbit of the planetary companion, suggesting an orbital inclination of $i \sim 40°$, and

(ii) the planet radius $R_p \simeq 1.2\ M_{Jup}$, in accordance with the general theoretical predictions of Guillot et al. (1996) and Burrows et al. (2000), and with observations of the planetary transits across HD209458 (Charbonneau et al. 2000),

we are able to rule out a reflective planet with a grey albedo greater than $p = 0.39$ to the 99.9% confidence level. The alternative approach of adopting the specific grey ($p = 0.3$), class V and class IV albedo models of Sudarsky, Burrows & Pinto (2000) places model-dependent upper limits on the planetary radius. The results indicate to 99.9% confidence that the upper limits are 1.37 R_{Jup}, 1.08 R_{Jup} and 1.22 R_{Jup} respectively for the three

albedo models considered.

Our analysis reveals a candidate signal of marginal significance with a projected orbital velocity amplitude of $K_p = 97$ km s^{-1}, assuming a grey albedo spectrum. If genuine, this would suggest an orbital inclination close to $\sim 37°$, a planet mass $M_p = 7.28$ (± 0.83) M_{Jup} and a grey geometric albedo of $p = 0.32$ (± 0.13), assuming $R_p = 1.2\ R_{Jup}$. If we feign complete ignorance of the value of K_p, our bootstrap Monte Carlo simulations give a probability ranging from 3 to 15% that the detected feature is a consequence of spurious noise from the analysis. When taking into account our prior knowledge of the system these false alarm probabilities drop to below 3%.

In particular, the class V albedo model, in which only the spectrum shortward of 550 nm is unaffected by Na I D absorption, returns a false-alarm probability of only 0.3% when the prior probability distribution for K_p is taken into account using Bayes' theorem. However, we consider there is still too much uncertainty for us to claim a bona fide detection. Our simulations show that a statistically unassailable detection should produce a clearly visible, dark streak along the planet's trajectory in the trailed spectrogram, and no such streak is apparent even for the class V model.

The observations in the 2000 season were conducted at orbital phases optimised to produce the strongest possible signal at a star-planet separation in velocity space sufficient to avoid blending problems. By adopting similar observing strategies on 8m-class telescopes, future reflected light searches of τ Bootis should be able to double the effective planetary signal contained in the WHT data described here, in only a small fraction of the 17 nights devoted to this search. Indeed, 2 optimally-phased clear nights on the KeckI/HIRES combination should be able to reproduce our results, whilst the increased efficiency of the HDS spectrograph would allow Subaru to achieve very close to this depth of search over the same timescale. With this in mind, we believe that τ Bootis remains a suitable target for future reflected light searches on 8m-class telescopes.

CHAPTER 6

A search for the starlight reflected from HD 75289 b

This chapter summarises the contents of a paper, authored by myself and recently published in MNRAS (Leigh et al. 2003b), presenting work carried out in conjunction with Andrew Collier Cameron, Stephane Udry, Jean-François Donati, Keith Horne, David James and Alan Penny, all of whom were cited as co-authors.

6.1 Introduction

The existence of a close planetary companion to the G0V star HD75289 was first reported by Udry et al. (2000), and in common with 19 of the 110 extrasolar planets known, HD75289b is found to orbit within 0.1 AU of the parent star. Confirmation of the gas-giant nature of HD209458b (Charbonneau et al. 2000; Henry et al. 2000b) and OGLE-TR-56b (Konacki et al. 2003) suggests that HD75289b may also be large enough to reflect a detectable amount of starlight. Sudarsky, Burrows & Hubeny (2003) suggest the high effective temperature and relatively low surface gravity of HD75289b may favour the formation of relatively bright, high-altitude silicate cloud decks. As described in Chapter 2.2.3, these clouds act to scatter starlight back into space before it is strongly absorbed by alkali metals in the deeper atmosphere.

In this chapter, we report the results of observations, conducted over 4 nights in January 2003 on VLT(UT2)/UVES échelle spectrograph, aimed at detecting the signature of starlight reflected from the planet orbiting HD75289.

6.2 System Parameters

HD75289 (HIP43177) is an G0 main sequence star with parameters listed in Appendix A.1. High-precision radial-velocity measurements obtained between Nov 1998 and Oct 1999 (Udry et al. 2000) were used to identify a planetary companion, HD75289b, whose properties (as determined directly from radial-velocity studies or inferred using the estimated stellar parameters) are summarised in Appendix A.2. Since the planet publication (Udry et al. 2000), the orbital solution has been updated with new Coralie RV measurements using a weighted cross-correlation scheme (Pepe et al. 2002) with an appropriate template.

6.2.1 Rotational broadening

The rotational broadening of the direct starlight and low chromospheric Ca II H & K emission flux suggest that the orbital period of the planet is much less than the stellar rotation period. As a consequence of the relative motion between the surface of the planet and the surface of the star, the planet will reflect a rotationally broadened stellar spectrum. Using Monte Carlo trials, similar to those conducted in Chapter 3, we estimate from the known stellar parameters that absorption lines attributed to the reflection from the planet's atmosphere are likely to be much broader, with typical line widths approaching 13 km s^{-1}.

6.3 Observations

We observed HD75289 during Jan 2003 using the blue arm of the UV-Visual Échelle Spectrograph (UVES), mounted on the 8.0m VLT/UT2 (Kueyen) telescope at the Paranal Observatory in the Atacama Desert, Chile. The detector was a single EEV CCD-44 array containing some 2048 × 3000 15.0-μm pixels. The CCD was centred at 475.8 nm in order 102 of the 41.6 g mm^{-1} échelle grating, giving complete wavelength coverage from 406.5 nm to 522.0 nm with minimal vignetting. The average pixel spacing was close to 1.5 km s^{-1}, and the full width at half maximum intensity in the centre of the thorium-argon arc calibration spectra was 4.5 pixels, giving an effective resolving power of $R = 43000$.

UTC start	Phase	UTC End	Phase	Exposures
2003 Jan 14 01:00:04	0.318	2003 Jan 14 09:29:44	0.420	188
2003 Jan 15 00:56:42	0.605	2003 Jan 15 09:21:32	0.706	173
2003 Jan 21 02:40:18	0.340	2003 Jan 21 09:34:54	0.422	183
2003 Jan 22 03:35:30	0.597	2003 Jan 22 09:41:01	0.707	140

Table 6.1: Journal of observations. The UTC mid-times and orbital phases are shown for the first and last spectral exposures secured on each night of observation. The number of exposures is given in the final column.

Table 6.1 details the 4 nights of observation that contribute to the analysis presented here. The stellar spectra were each exposed for between 100s and 300s, depending upon the seeing, in order to expose the CCD to a peak count of 40000 ADU per pixel in the brightest parts of the image. A typical exposure in average seeing (0.8 arcsec) yielded $\sim 4 \times 10^5$ electrons per pixel step in wavelength in the brightest orders after extraction. Overall, the CCD's 7s fast-readout time allowed an observing efficiency $> 90\%$, whilst yielding a gain close to 2.4 and readout noise of $\sim 6e^-$. Following extraction, the S:N in the continuum of the brightest orders was typically 650 per pixel.

6.4 Data Analysis

In common with the analysis conducted on τ Bootis in the previous chapter, single dimension spectra were extracted from the raw images using an automated pipeline reduction system built around the Starlink ECHOMOP and FIGARO packages.

As described in Chapter 4.2.2, the initial tracing of the échelle orders on the CCD frames was performed manually using calibration exposures taken specifically for the purpose. The automated extraction procedure then subtracted the bias from each frame, cropped it, determined the form and location of the stellar profile on each image relative to the trace, subtracted a linear fit to the scattered-light+sky background across the spa-

tial profile, and performed an optimal (profile and inverse variance-weighted) extraction of the orders across the full spatial extent of the object+sky region.

Flat-field balance factors were applied prior to the extraction process by way of nightly templates summed from the 50 to 100 flat-field frames taken at the start and end of each observing session. The summation used an algorithm to identify and reject cosmic rays and other non-repeatable defects by comparing successive frames (see Chapter 4.3). Although the UVES instrument was very stable between observations, it was found that the level of noise was slightly reduced ($\sim$ 2%) by the use of nightly flat-fields rather than master flat-fields combining all 4 night's data.

In all, 25 orders (numbers 90 - 114) were extracted from each exposure, giving full spectral coverage from 406.5 to 522.0 nm with good overlap.

6.4.1 Extracting the planet signal

The first step in extracting the reflected component is to subtract the direct stellar component from the observed spectrum (Chapter 4.3). The planet signal should then consist of faint Doppler-shifted copies of each of the stellar absorption lines, at this stage buried deeply in the noise. After cleaning up any correlated fixed-pattern noise remaining in the difference spectra (see Chapter 4.4), we create a composite residual line profile, by deconvolving each residual spectra with a list of stellar absorption line strengths (Chapter 4.5). The composite line profiles are then stacked by phase to display temporal variations in brightness and radial velocity, as at Fig. 6.2. Any planet signal, if present, would appear as a dark sinusoidal feature crossing from right to left as phase increases and centred on the superior conjunction at phase 0.5. Such a trail can be seen with the addition of a simulated planet signal, as Fig. 6.1 demonstrates.

Ideally, we would have aimed to target gibbous phases $0.33 < \phi < 0.47$ and $0.53 < \phi < 0.67$ to give us the best chance of disentangling the planet spectrum from the direct stellar spectrum. However, differences between the most recent ephemeris update (supplied Apr 2003 by Stephane Udry) and the original Udry et al. (2000) values on which we planned our observing proposal, have resulted in our targeting slightly less optimal but still workable phases.

The central pattern of distortions in both Figs. 6.1 and 6.2 is again consistent with

sub-pixel shifts in the position of the stellar spectra with respect to the detector over the course of the night. Fortunately they only affect a range of velocities at which the planet signature would in any case be indistinguishable from that of the star.

6.4.2 Simulated planet signatures

We verified that a planetary signal is preserved through the above sequence of operations, in the presence of realistic noise levels, by adding a simulated planetary signal to the observed spectra. The fake signal also acts to calibrate the strength of any genuine detection, as well as the confidence contours associated with the data. Detailed explanations of the simulated planet calibration can be found in Chapter 4.8.

In order to correctly mimic the reflected starlight, we broadened the spectral lines of the star HD1461 to give typical line widths of ~ 13 km s^{-1}, in line with our estimates, from known stellar parameters, for rotational broadening due to relative motion between the surface of the planet and that of the star. HR1461 is a G0V star of similar temperature and elemental abundance to HD75289, but with a $v \sin i$ we calculate at 8.8 ± 0.3 km s^{-1}. To ensure a strong signal we used a simulated planet of radius 1.6 R_{Jup}, and a wavelength-independent geometric albedo $p = 0.4$, which when viewed at zero phase angle should give a planet/star flux ratio $\epsilon_0 = f_p/f_* = 9.71 \times 10^{-5}$.

6.4.3 Matched Filter Analysis

The next step involved a matched-filter analysis, as described by Chapter 4.6, to search for features in the time-series of composite residual profiles whose temporal variations in brightness and radial velocity resemble those of the expected reflected-light signature.

The relative probabilities of the χ^2 fits to the data for different values of the free parameters R_p/a and K_p are again displayed in greyscale form as a function of K_p and $\log(\epsilon_0) = \log p(R_p/a)^2$. Figs. 6.3 and 6.4 detail the probability maps for the simulated and original observations respectively, normalised to the most probable value.

To set an upper limit on the strength of any planet signal, or to assess the likelihood that any signal detection is spurious, we need to compute the probability of obtaining similar improvements in χ^2 by chance alone. We achieve this using the "bootstrap" procedure

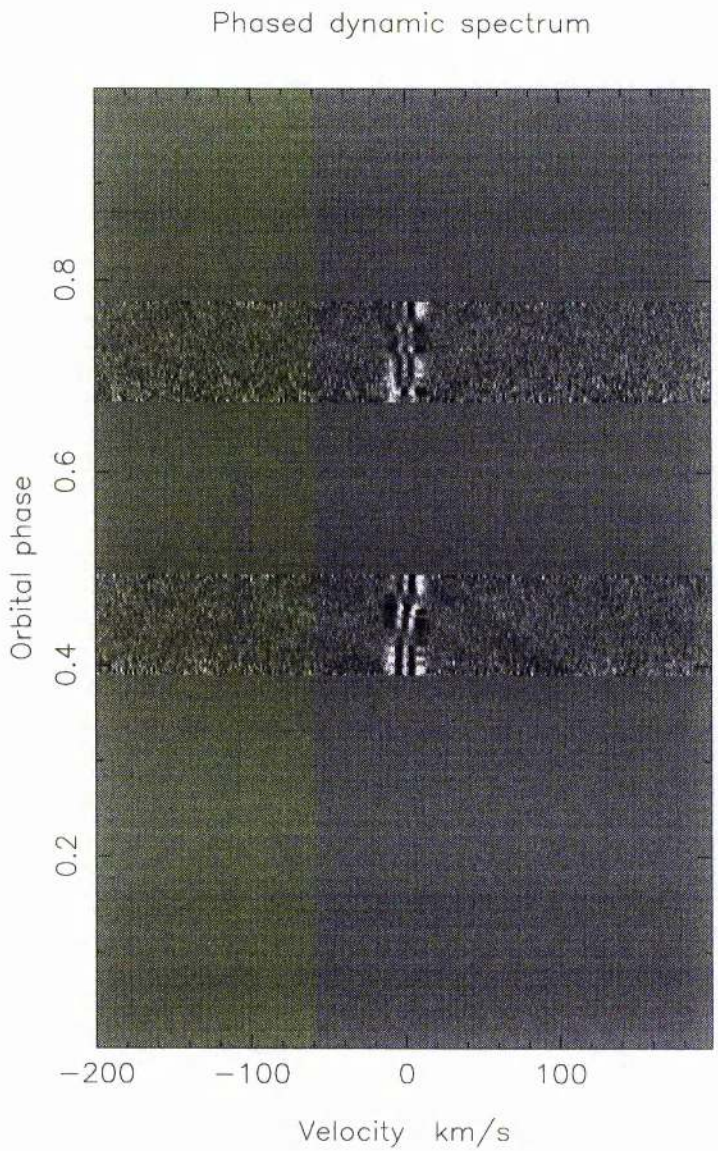

Figure 6.1: Time series of deconvolved profiles derived from the original VLT(UT2)/UVES data secured over 4 nights in Jan 2003, but with the addition of a simulated planet signal at an inclination of 80°. The injected signal is that of a planet with geometric albedo $p = 0.4$ and radius 1.6 R_{Jup} and appears as a dark sinusoidal feature crossing from right to left as phase increases and centred on the superior conjunction at phase 0.5.

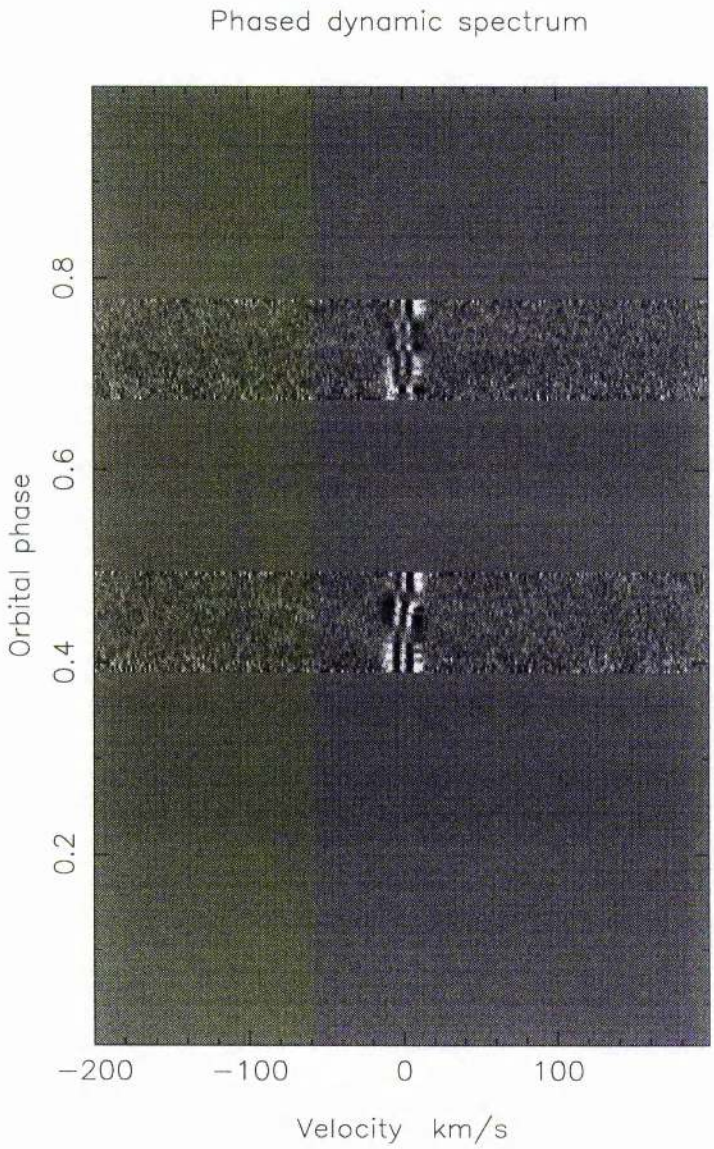

Figure 6.2: Time series of deconvolved profiles derived from the original VLT(UT2)/UVES spectra, secured over 4 nights observation in Jan 2003. The greyscale runs from black at -10^{-4} times the mean stellar continuum level, to white at $+10^{-4}$. The velocity scale is in the reference frame of the star.

described in Chapter 4.8 to construct empirical distributions for confidence testing, using the data themselves. In 3000 trials, we randomized the order in which the 684 observations were secured, but associated them with the original sequence of dates and times. Genuine signals are scrambled in phase, but re-ordered data are as capable as the original data of producing spurious detections through chance alignments of systematic errors along a sinusoidal path through the data. We record the least-squares estimates of $\log(\epsilon_0)$ and the associated χ^2 as functions of K_p in each trial. The percentage points of the resulting bootstrap distribution are shown as contours in Figs. 6.3 and 6.4. From bottom to top, these contours give the 68.4%, 95.4%, 99.0% and 99.9% bootstrap upper limits on the strength of the planet signal.

6.5 Results

The results of this analysis appear in the form of a relative probability map of model parameters K_p and $\log(\epsilon_0) = \log p(R_p/a)^2$, shown at Fig. 6.4. The plot indicates that there is no significant evidence to support the existence of a reflected-light signature, but the calibrated confidence contours do allow us to apply constraints to the geometric albedo of the planet, given certain theoretical assumptions about the system.

6.5.1 Upper limits on grey albedo

The grey albedo model makes the unlikely assumption that the planet/star flux ratio remains independent of wavelength. By adopting a theoretical radius for the planet we can use Eqn. 2.16 to constrain its geometric albedo. Fig. 6.5 details the upper limits on the albedo at the 99.9% level of significance, for a range of possible radii. Each theoretical radius we investigate is represented by an upper confidence contour that spans orbital inclinations from 30° to 80°.

We find that the albedo limits are less strongly constrained with low inclination systems. This is partly a consequence of the matched-filter analysis, where fitting such models incorporate more pixels close to the noisier ripples in the central stellar region of the deconvolved profile. In addition, we find the choice of phase function acts to weaken the signals at low inclination, thus introducing greater uncertainty to the model fitting in

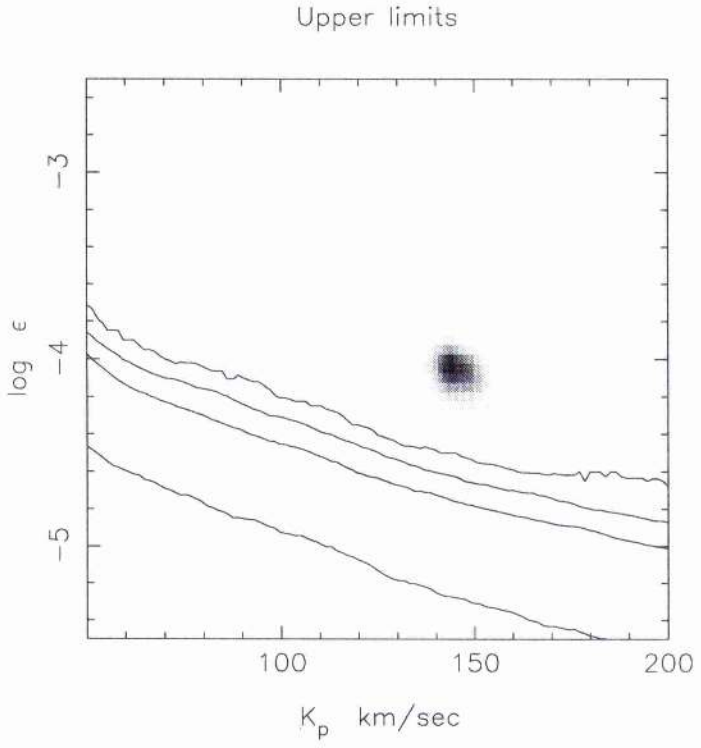

Figure 6.3: Relative probability map of model parameters K_p and $\log(\epsilon_0) = \log p(R_p/a)^2$ for a simulated planet signature with grey albedo $p = 0.4$, $R_p = 1.6\ R_{Jup}$ and orbital inclination of 80°. The contours show the confidence levels at which spurious detections due to non-Gaussian noise can be ruled out. From top to bottom, they show the 99.9%, 99.0%, 95.4% and 68.4% confidence limits. The synthetic planet signature is detected well above the 99.9% confidence limit.

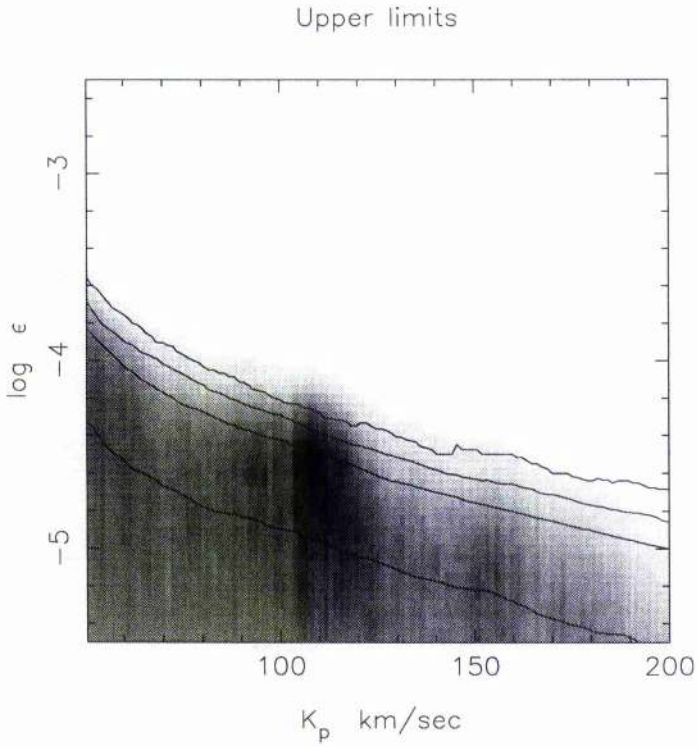

Figure 6.4: Relative probability map of model parameters K_p and $\log(\epsilon_0) = \log p(R_p/a)^2$, derived from the VLT(UT2)/UVES observations of HD75289, assuming a grey albedo spectrum. The greyscale denotes the probability relative to the best-fit model, increasing from 0 for white to 1 for black. Unfortunately, the results of the processing show little evidence to support the existence of a close-orbiting planet. Once again, it is important to note that the contours only give the probability of a false detection if the value of K_p is known in advance, which is not the case here. The slightly increased probability density seen close to $K_p = 110$ km s^{-1} (within the K_p distribution predicted in Chapter 3) returns a large false-alarm probability of 32% when considering all plausible values $35 < K_p < 147$ km s^{-1}, which is far too uncertain to claim as genuine.

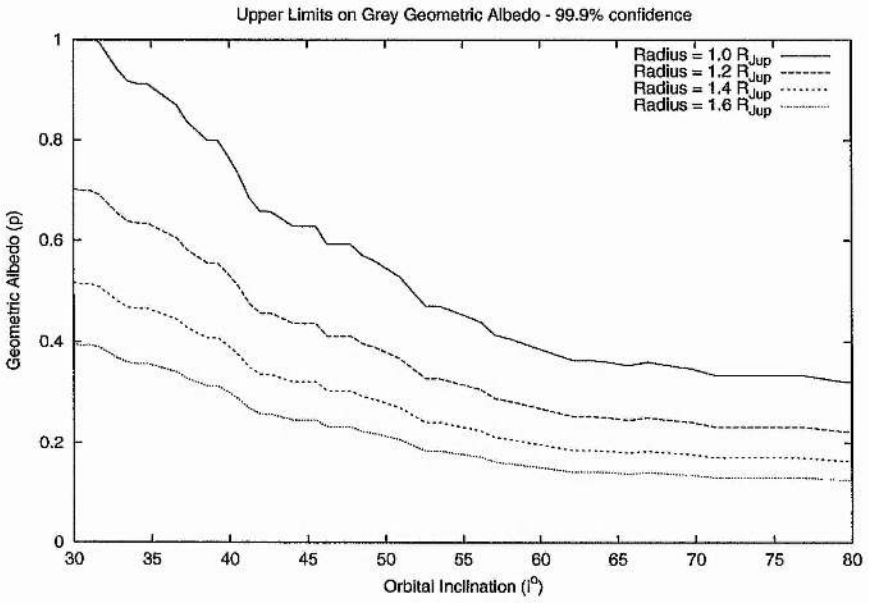

Figure 6.5: Upper geometric albedo limits to the 99.9% confidence level, assuming the atmosphere of the planet imposes no wavelength dependence on reflected light, i.e. a grey albedo model. The contours, from top to bottom, represent upper limits assuming theoretical radii for the orbiting planet of 1.0, 1.2, 1.4 and 1.6 R_{Jup}, covering orbital inclinations of $30° < i < 80°$. Thus, for a predicted radius 1.6 R_{Jup} at the most probable inclination $i = 75°$ (Leigh, Collier Cameron & Guillot 2003), our observations suggest we can be 99.9% confident of a grey geometric albedo $p < 0.12$.

the matched-filter analysis.

If we adopt the theoretical radius for HD75289b, as predicted in Chapter 3, of $R_p = 1.6\ R_{Jup}$, and assume a Venus-like phase function, we find the planet/star flux ratio, at the most probable $K_p \simeq 127$ km s^{-1}, is constrained to $f_p/f_* < 4.18 \times 10^{-5}$ at the 99.9% level, i.e. a geometric albedo less than 0.12. This would strongly rule out albedo models which incorporate high-altitude, reflective cloud decks such as the class V model of Sudarsky, Burrows & Pinto (2000).

6.6 Conclusion

We have observed HD75289 over 4 nights in Jan 2003, using the VLT(UT2)/UVES instrument, in an attempt to detect starlight reflected by the known close-orbiting planetary companion. The excellent stability of the spectrograph, combined with the reasonable conditions encountered, have enabled us to produce deep upper limits on the geometric albedo of the planet. In truth, with our knowledge of the system and current theoretical predictions, we would have expected to detect the planet. However, we find very little evidence to suggest its presence. Possible reasons for the discrepancy are,

(i) The inclination of the system is such ($i < 20°$) that the spectral features of the planet do not cleanly separate from the stellar features. i.e. the maximum Doppler shift is not sufficient to disentangle the planet's signal. However, the work conducted in Chapter 3, suggests an inclination well in excess of 20°.

(ii) Our choice of phase function $g(\alpha, \lambda)$ is wrong. It may be that close-orbiting Pegasi planets are less prone to back-scatter incoming starlight than we see with Jupiter or Venus (Hovenier 1989; Seager, Whitney & Sasselov 2000).

(iii) Although the two transiting planets (Charbonneau et al. 2000; Konacki et al. 2003) have indicated the presence of gas giants, it may be HD75289b is a more compact terrestrial planet reflecting substantially less starlight (see Guillot et al. 1996).

(iv) It could simply be that, as with the Sudarsky, Burrows & Pinto (2000) predictions for a class IV CEGP, the geometric albedo is inherently low, with starlight being absorbed deep in the atmosphere of the planet where no high-level clouds are present to reflect the incident light.

Whatever the cause, these observations provide a strong test for developing theoretical models which aim to predict the atmospheric nature of these objects. This is a field which desperately needs continued observations on the brightest of these Pegasi planets, as were detailed in Chapter 3.

CHAPTER 7

Summary and Conclusions

Since the most significant discovery of an extrasolar planet in 1995 (Mayor & Queloz 1995), astronomers have indirectly identified over 110 planetary objects. These Jovian-mass objects cause the host star to "wobble" slightly about the common centre-of-mass of the system, a wobble detectable as radial motion in high-precision Doppler spectroscopy. Of the known planets, about 20% are found to orbit within 0.1 AU of the star, with the transits of HD209458 (Charbonneau et al. 2000; Henry et al. 2000b) and OGLE-TR-56 by Konacki et al. (2003) tentatively confirming the gas-giant nature of these close-in extrasolar giant planets (CEGPs), or Pegasi planets as they are known.

The discovery of Pegasi planets has produced a wave of speculative theory as to their exact nature, and how they came to exist so close to their parent star. The spectroscopic technique described in this thesis provides a viable method of achieving the direct detection of an EGP atmosphere by searching for the reflected-light signature of the orbiting companion. The results of such observation allow us to test emerging models that aim to predict the atmospheric nature of Pegasi planets, and may also provide information on the orbital inclination and mass of the planet.

In Chapter 1, we provided a historical overview of the important events, in the field of extrasolar planets, which have brought us to where we are today, and the various detection techniques that are being employed to drive the field forward. We also reviewed the general consensus and ideas surrounding the formation of stars and planets, to provide background knowledge for the following chapters. Chapter 2 discusses the physical basis that underpins all aspects of our analysis and examines the knowledge that has been gleaned from the known crop of ESPs. It continues by investigating how theory has stepped in and developed, over the intervening years, to generate models that aim to

predict the evolution and atmospheric nature of EGPs. The chapter finishes by exploring the manner in which light from the stellar host can interact with material in the upper atmosphere of the orbiting planet, and identifies the two main observable quantities which can be extracted from high-resolution spectroscopic studies of the parent star - namely the planet/star flux ratio, ϵ_0, and the projected orbital velocity, K_p. In Chapter 3 we use theoretical predictions and prior knowledge of each system to predict these observable quantities for six nearby Pegasi planets. These predictions allow us to estimate the amount of telescope time typically required to search for the expected reflection.

Chapter 4 provides a detailed description of the technique we have developed, starting from the acquisition of high-resolution échelle spectra, working through the spectral extraction, separation and enhancement of any orbital motion buried in the data, and finishing off with routines to identify and calibrate the strength of any planetary signature present. Chapters 5 and 6 detail the cases of τ Bootis and HD75289, to which we have applied our method, and from which we have obtained very encouraging results, not only for a significant candidate detection around τ Bootis, but also in providing strong tests on emerging theoretical predictions. The results for τ Bootis and HD75289, together with a summary of the results from Chapter 3, are set out in more detail below.

7.1 Prospects for spectroscopic reflected-light studies

In Chapter 3, we use Monte Carlo trials to estimate prior probability distributions for the orbital velocity amplitude and planet/star flux ratio of six bright stars known to harbour giant planets in orbits with periods of less than 5 days. Using these estimates, our primary aim was to assess the viability of these targets for future reflected-light searches using 4m and 8m-class telescopes.

By combining the best data available from past stellar observations with theoretical assumptions about each planet's radius, atmospheric scattering properties, and by adopting a realistic albedo spectrum, we were able to derive prior probability distributions for the observable quantities K_p and ϵ_0. The estimates provide us with a quantifiable method by which we can assess the plausibility of any candidate detection, both in K_p and ϵ_0, and were used for comparison in both the τ Bootis and HD75289 analyses. Although we do not want to be guided too closely by theory, values outside the plausible range would pose

difficulties for current thinking.

The primary finding of Chapter 3 was the suggestion that, in using the search for υ And b (Collier Cameron et al. 2002) as a benchmark to reach the predicted ϵ_0 signal levels, the remaining five targets (τ Boo, 51 Peg, HD75829, HD179949 and HD209468) remained viable and compelling targets for future studies with existing high-throughput spectrographs on 8m or 10m-class telescopes. We have been reasonably fortunate in obtaining telescope time in the past, but if we are to concentrate our efforts towards larger instruments, we will be entering a extremely competitive environment. Having these time predictions available in published form will provide us with a useful reference for any future proposals.

7.2 τ Bootis analysis

τ Bootis was the first dataset I worked on, providing the basis of my understanding and allowing me to recognise potential opportunities and pitfalls inherent in what is a complicated method of data analysis. In being able to closely follow and analyse interactions within the original routines developed by Collier Cameron et al. (1999), and further improved by Collier Cameron et al. (2002), we have been able to overhaul the fundamental driving scripts, and develop a more streamlined and consistant approach to the manner in which we conduct the analysis.

In Chapter 5, we introduced a number of significant changes to the τ Bootis analysis, changes which have both enhanced the quality, and more accurately portrayed the results of our observation. In the first instance, we conducted a complete re-extraction of the 1998 and 1999 data (Collier Cameron et al. 1999), combining it with the 2000 data (Collier Cameron et al. 2001). By increasing the wavelength range of the extracted orders and by changing the way in which we apply flat-field corrections, we were able to make inroads into reducing the amount of noise. Further improvements came from the inclusion of a Principal Component Analysis (PCA) routine to remove correlated fixed-pattern noise. More importantly, however, we recongnised the loss of signal strength through the process, which required the incorporation of a more stringent calibration technique, to quantify and correct for the fraction of the signal (simulated or genuine) lost during the stellar subtraction, deconvolution and PCA routines. This in turn meant our results were

not as optimistic as those introduced at conference by Collier Cameron et al. (2001), who assumed no loss of signal through the process. Nevertheless, our results still provide an important contribution to the development of the ESP field, with the three main aspects returned by the analysis as follows:

1. The appearence of a marginal detection at a projected orbital velocity amplitude $K_p = 97$ km s^{-1}. If genuine, this would suggest the existence of a planet with an orbital inclination close to $\sim 37°$ which, when combined with the results of radial-velocity measurements, indicate a mass $M_p = 7.28$ (± 0.83) M_{Jup}. If we assume atmospheric scattering properties similar to those of Venus, and a planet radius $R_p \simeq 1.2\ M_{Jup}$, in accordance with the general theoretical predictions of Guillot et al. (1996); Burrows et al. (2000), the strength of our candidate feature suggests a grey geometric albedo $p = 0.32$ (± 0.13). Although encouraging, we do not feel ready to claim a bona fide detection, partly as a result of the calculated 3-15% false-alarm probabilties, but more importantly due the absence of any characteristic trail in the phase-series of deconvolved profiles (Fig. 5.2).

2. By assuming a 1.2 R_{Jup} planet, tidally locked to an $i \sim 40°$ orbit around τ Bootis, we were able to rule out a reflective planet with a grey albedo greater than $p = 0.39$ to the 99.9% confidence level.

3. The alternative approach of adopting the specific grey ($p = 0.3$), class V and class IV albedo models of Sudarsky, Burrows & Pinto (2000) places model-dependent upper limits on the planetary radius. The results indicate to 99.9% confidence that the maximum radii of the models are 1.37 R_{Jup}, 1.08 R_{Jup} and 1.22 R_{Jup} respectively.

Notwithstanding the possible detection, these results provide useful constraints to the parameter space that is undoubtedly occupied by these Pegasi planets. This is due, in the main, to the distinct shortage of observational evidence currently available to drive forward theoretical thinking. One important factor that again emerges clearly from the τ Bootis analysis, and backed up by the results of Chapter 3, is that τ Bootis remains a viable target for future reflected light searches on 8m-class telescopes. Whilst we were very fortunate to have 17 nights of WHT/UES data to work with, it would seem clear that 3 optimally-phased nights on a modern 8m-class telescope would easily replicate the depth of the search achieved here.

7.3 HD 75289 analysis

The subsequent application of our technique (Chapter 6) was on the more recent HD75289 dataset, secured over 4 nights in 2003 Jan using the VLT(UT2)/UVES instrument. This step up to an 8m-class telescope represents a significant advance for our observing programme.

Due, primarily, to the improved throughput of the VLT(UT2)/UVES instrument in comparison to WHT/UES, the depth of the HD75289 search was significantly better than predicted in Chapter 3. When combined with prior predictions for the radius and brightness of HD75289, this suggests a good probability of a direct detection. However, we find no significant evidence to indicate such a detection. Despite this, our ability to constrain $f_p/f_* < 4.18 \times 10^{-5}$ to 99.9% confidence, assuming $i = 75°$, $R_p = 1.6\ R_{Jup}$ and a Venus-like phase function, provides a strong test for developing theoretical models, which we hope will be picked up for future work by others in the field. It is, perhaps, another sign that all is not as predicted - an increasingly common statement when it comes to ESPs.

We identified a number of reasons in Chapter 6.6, which may have resulted in the non-detection. From the recovery of simulated planet signatures through the process, we are confident that if the atmosphere of a planet reflects a scaled down copy of the host spectrum, we would detect it. This leaves us with three obvious alternatives -

1. The scattering properties in the atmosphere of HD75289b differ substantially from the planets in our own Solar System. In this respect it would be useful to investigate how the scattering properties of atmospheric condensates change with variations in temperature and pressure. The recent launch of MOST (Green et al. 2003) should allow 'ultraprecise' photometric observations that, given time, should be able to shed some light on this issue.

2. The atmosphere of HD75289b is more absorbing than predicted for a Pegasi planet (Sudarsky, Burrows & Hubeny 2003), although, as yet, it is too early to say whether this is also the case for τ Bootis and υ And. Either the expected silicate and iron clouds do not appear, or alkali metal absorption may act to absorb more incident light than predicted. The latter case may be somewhat contradicted by the discovery (Charbonneau et al. 2002) that Na produces a weaker absorption feature in trans-

mission, during transits of HD209458, than is predicted by theory. The existence and level of cloud layers, however, is going to be a tougher nut to crack, with complexities being introduced due to non-equilibrium chemical compositions, thermal mixing, zonal winds (Showman & Guillot 2002), and possible temporal variations (Cho et al. 2003). In all cases, the best we can hope for will be a general idea of the prevailing atmospheric nature. In the case of HD75289b, assuming the phase function and size are as predicted, the general view here (at the wavelengths we investigated) would be of an object with an albedo close to that of the Moon, i.e. $p \sim 0.11$ (NASA 2003).

3. The size of HD75289b is substantially smaller than predicted in Chapter 3, in which case we need to think again carefully about the validity of the evolutionary models we use. It is important, however, that we do not lose sight of the fact that at least some of these planets may be massive terrestrial objects and will thus reflect substantially less starlight.

Once piece of comfort we can take from the better than expected depth of the HD75289 analysis, is the greater optimism we can hold in future observations using modern instrumentation. Once again, the suggestion is that we need to focus our efforts towards securing time on the larger, more efficient instruments such as Subaru/HDS, KeckI/HIRES and VLT(UT2)/UVES.

7.4 Future work

These and past observations have so far provided us with very encouraging results, but with regard to our knowledge of the atmospheric nature of Pegasi planets, we are only just scratching the surface. If we are to gain a better understanding of these unusual objects, it is vital that we continue to strive for direct detections. Due to magnitude, orbital period and mass considerations, we estimate that with current technology, there are six main stars with CEGPs, for which observations could yield valuable information (Leigh, Collier Cameron & Guillot 2003). Of these, we have observed τ Bootis most comprehensively (Collier Cameron et al. 1999; Collier Cameron et al. 2001; Leigh et al. 2003a), and conducted initial investigations on both υ And (Collier Cameron et al. 2002) and HD75289 (Leigh et al. 2003b). Fig. 7.1 compares the prior probability distributions,

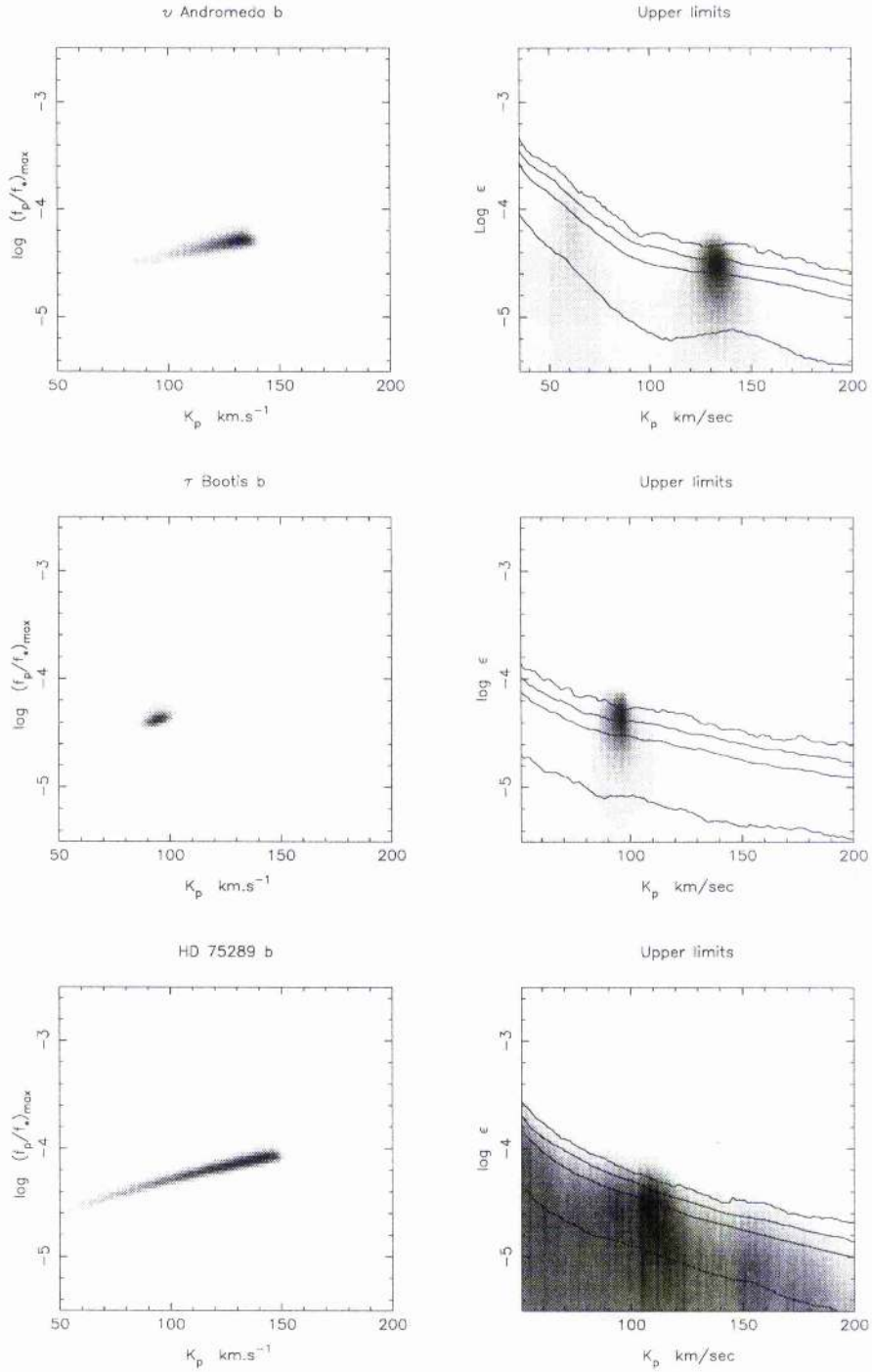

Figure 7.1: Comparison of prior probability distributions, as determined in Chapter 3, with the results of (top) the previous analysis of υ And (Collier Cameron et al. 2002), together with the two analyses presented here, namely (centre) τ Bootis (Leigh et al. 2003a) and (lower) HD75289 (Leigh et al. 2003b).

as determined in Chapter 3, with the results of our analysis in each case. It is interesting to note that for both υ And and τ Bootis, there are clearly defined features appearing very close to the respective peaks in the prior K_p distibutions. Although we are not yet confident enough to claim bona fide detections, the existence of these candidate features may give us great cause for optimism.

For future work, we would therefore like to revisit υ And and τ Bootis, using larger instruments than were previously used, whilst also seeking to broaden observations to include the remaining three objects, HD179949, HD209458 and 51 Pegasi. In addition, we see exciting possibilities from seeking to extend our technique on two further fronts.

1. The first involves conducting standard single-order spectroscopy toward the blue end of the optical spectrum, where dominant Rayleigh scattering in the planet's atmosphere is predicted to reflect a substantial fraction of the incident stellar light (see Chapter 2.2). We believe the signal-to-noise (S:N) gain that is lost by having fewer absorption lines for the deconvolution process, will be offset, not only by increased reflection in the blue, but also from better instrumental and observing efficiencies available with standard spectrographs, such as ISIS(WHT) and STIS(HST)
2. The second front involves observing more towards the near-IR, where thermal emission from Pegasi planets is expected to make a much greater contribution toward the total flux received from the star-planet system. Instruments such as CRIRES(VLT), PHOENIX(Gemini-S), VISIR(VLT) and NIRSPEC(Keck) would prove useful in this respect.

With regard to the current software, we believe it now offers an effective and stable platform on which to conduct future analyses. Once the initial difficulties with new datasets have been ironed out, the driving scripts appear to work well. The underlying processing routines could, however, possibly benefit from a few revisions, (1) to improve their efficiency and (2) to address potential compatibility issues with future incarnations of the STARLINK software collection, which plays such a major role in our full analysis.

In this thesis, we have made an important contribution towards establishing the nature of extrasolar planets, a field for which there is very little direct observational data available. Hopefully with the advent of the MOST (Matthews, Kuschnig & Shkolnik 2001) and COROT (Bordé, Rouan & Léger 2003) space-based platforms, this deficiency will soon

be addressed, but even then it is vital to continue with ground-based observations, such as those detailed here. From our perspective, there is a great deal still yet to do, and, given the observing time, we can continue to make a valuable contribution with the ongoing debate as to the true atmospheric nature of close-orbiting Pegasi planets.

REFERENCES

AAO, 2003, http://www.aao.gov.au/astro/ucles.html

Armitage P., Livio M., Lubow S., Pringle J., 2002, MNRAS, 334, 248

Armitage P., 2003, ApJ, 582, L47

Baliunas S., Henry G., Donahue R., Fekel F., Soon W., 1997, ApJ, 474, 119

Baraffe I., Chabrier G., Barman T., Allard F., Hauschildt P., 2003, Astronomy and Astrophysics, 402, 701

Barman T., Hauschildt P., Allard F., 2001, ApJ, 556, 885

Barman T., Hauschildt P., Schweitzer A., Stancil P., Baron E., Allard F., 2002, ApJ, 569, 51

Barnes J., Collier Cameron A., Unruh Y., Donati J., Hussain G., 1998, MNRAS, 299, 904

Barnes J., 1999, PhD thesis, University of St Andrews

Barnes S., 2001, ApJ, 561, 1095

Benedict G. F., McArthur B., Chappell D. W., Nelan E., 1999, AJ, 118, 1086

Benz W., Mayor M., 1984, Astronomy and Astrophysics, 138, 183

Black D., 1980, Icarus, 43, 293

Bodenheimer P., Hubickyi O., Lissauer J., 2000, Icarus, 143, 2

Bodenheimer P., Lin D., Mardling R., 2001, ApJ, 548, 466

Bordé P., Rouan D., Léger A., 2003, Astronomy and Astrophysics, 405, 1137

Borucki W., Koch D., Dunham E., Jenkins J., 1997, PASPC, 119, 153

Borucki W., Caldwell D., Koch D., Webster L., Jenkins J., Ninkov Z., Showen R., 2001, PASP, 113, 439

Boss A., 1988, ApJ, 331, 370

Boss A., 1995, Sci, 267, 360

Brown T., Charbonneau D., 1999, BAAS, 31, 1534

Brown T., Charbonneau D., Gilliland R., Noyes R., Burrows A., 2001, ApJ, 552, 699

Burrows A., Saumon D., Guillot T., Hubbard W., Lunine J., 1995, Nat, 375, 299

Burrows A., Marley M., Hubbard W., Sudarsky D., Guillot T., 1997, ApJ, 491, 856

Burrows A., Guillot T., Hubbard W., M. M., Saumon D., Lunine J., Sudarsky D., 2000, ApJ, 534, 97

Burrows A., Sudarsky D., Hubbard W., 2003, ApJ, 594, 545

Butler P., Marcy G., 1996, ApJ, 464, 153

Butler P., Marcy G., Williams E., Hauser H., Shirts P., 1997, ApJ, 474, 115

Butler P., Marcy G., Fischer D., Brown T., Contos A., 1999, ApJ, 526, 916

CCPS, 2003, http://exoplanets.org/almanacframe.html

Charbonneau C., Noyes D., Jha S., Vogt S., 1999, ApJ, 522, 145

Charbonneau D., Brown T., Latham D., Mayor M., 2000, ApJ, 529, 45

Charbonneau D., Brown T., Noyes R., Gilliland R., 2002, ApJ, 568, 377

Cho J., Menou K., Hansen B., Seager S., 2003, ApJ, 587, L117

Clampin M., Ford H. C., Illingworth G., Petro L., JPF Science Team, 2001, American Astronomical Society Meeting, 199

Cody A., Sasselov D., 2002, ApJ, 569, 451

Collier Cameron A., Horne K., Penny A., James D., 1999, Nat, 402, 751

Collier Cameron A., Horne K., James D. J., Penny A. J., Semel M., 2001, in IAU Symp. 202: Planetary systems in the Universe. ASP Conference Series, San Francisco, In press: astro-ph0012186

Collier Cameron A., Horne K., Penny A., Leigh C., 2002, MNRAS, 330, 187

Cooper C., Sudarsky D., Milsom J., Lunine J., Burrows A., 2003, ApJ, 586, 1320

Del Popolo A., Yeşilyurt S., Ercan E., 2003, MNRAS, 339, 556

Donati J. F., Semel M., Carter B., Rees D. E., Collier Cameron A., 1997, MNRAS, 291, 658

Einstein A., 1936, Sci, 84, 506

ESO, 2003, http://www.eso.org/instruments/uves

Fischer D., Valenti J., 2003, in IAU Symp. 219: Stars as Suns - Activity, Evolution & Planets. ASP Conference Series, San Francisco

Fortney J., Sudarsky D., Hubeny I., Cooper C., Hubbard W., Burrows A., Lunine J., 2003, ApJ, 589, 615

Fuhrmann K., Pfeiffer J., Bernkopf J., 1997, Astronomy and Astrophysics, 326, 1081

Fuhrmann K., Pfeiffer J., Bernkopf J., 1998, Astronomy and Astrophysics, 336, 942

Gatewood G., Eichhorn H., 1973, AJ, 78, 769

Gaudi B., Burke C., DePoy D., Marshall J., Pogge R., STEPSS Collaboration, 2002, BAAS, 34, 1264

Geballe T., Kulkarni S., Woodward C., Sloan G., 1996, ApJ, 467, 101

Goldreich P., Tremaine S., 1980, ApJ, 241, 425

Gonzalez G., Laws C., 2000, AJ, 119, 390

Gonzalez G., Laws C., Tyagi S., Reddy B., 2001, AJ, 121, 432

Gonzalez G., 1998, Astronomy and Astrophysics, 334, 221

Goukenleuque C., Bézard B., Joguet B., Lellouch E., Freedman R., 2000, Icarus, 143, 308

Gould A., Loeb A., 1992, ApJ, 396, 104

Graboske H., Olness R., Pollack J., Grossman A., 1975, ApJ, 199, 265

Gratton R., Focardi P., Bandiera R., 1989, MNRAS, 237, 1085

Gray R., Napier M., Winkler L., 2001, AJ, 121, 2148

Gray D., 1992, The Observation and Analysis of Stellar Photospheres. Cambridge University Press, Cambridge, U.K

Green D., Matthews J., Seager S., Kuschnig R., 2003, ApJ, 597, 590

Groot P., Piters A., van Paradijs J., 1996, A&AS, 118, 545

Grossman A., Graboske H., 1973, ApJ, 180, 195

Guillot T., Showman P., 2002, Astronomy and Astrophysics, 385, 156

Guillot T., Burrows A., Hubbard W., Lunine J., Saumon D., 1996, ApJ, 459, 35

Guillot T., 1999, Sci, 286, 72

Harrington R. S., Harrington B. J., 1987, Mercury, 16, 77

Harris D. L., 1961, Photometry and Colorimetry of Planets and Satellites. University of Chicago Press, Chicago, IL

Henry G., Baliunas S., Donahue R., Fekel F., Soon W., 2000a, ApJ, 531, 415

Henry G., Marcy G., Butler P., Vogt S., 2000b, ApJ, 529, 41

Hershey J., 1973, AJ, 78, 421

Hilton J., 1992, Expanatory supplement to Astronomical Almanac. University Science Books, Mill Valley, CA

Hole K., Sasselov D., Kondratko P., Heinke C., Schnee S., Bonanos A., Ball G., 2001, American Astronomical Society Meeting, 199

Houk N., Smith-Moore M., 1988, MSS, C04, 0H

Hovenier J., 1989, Astronomy and Astrophysics, 214, 391

Hubbard W., Fortney J., Lunine J., Burrows A., Sudarsky D., Pinto P., 2001, ApJ, 560, 413

Hubbard W., 1977, Icarus, 30, 305

IAC, 2003, http://www.tng.iac.es/instruments/sarg/sarg.html

Karkoschka E., 1994, Icarus, 111, 174

Keck, 2003, http://www2.keck.hawaii.edu/inst/hires/hires.html

Konacki M., Torres G., Jha S., Sasselov D., 2003, Nat, 421, 507

Kuerster M., Endl M., Rouesnel F., S. E., A. K., 2003, Astronomy and Astrophysics, 403, 1077

Kurucz R., 1993, CDROM # 13 (ATLAS9 atmospheric models) and # 18 (ATLAS9 and SYNTHE routines, spectral line database), Cambridge MA

Laughlin G., Adams F., 1997, ApJ, 491, L51

Laughlin G., 2000, ApJ, 545, 1064

Leigh C., Collier Cameron A., Guillot T., 2003, MNRAS, 346, L16

Leigh C., Collier Cameron A., Horne K., Penny A., James D., 2003a, MNRAS, 344, 1271

Leigh C., Collier Cameron A., Udry S., Donati J.-F., Horne K., James D., Penny A., 2003b, MNRAS, 346, 890

Lin D., Papaloizou J., 1986, ApJ, 309, 846

Lin D., Bodenheimer P., Richardson D., 1996, Nat, 380, 606

Lissauer J., 1993, ARA&A, 31, 129

Lissauer J., 1995, Icarus, 114, 217

Mallén-Ornelas G., Seager S., Yee H., Minniti D., Gladders M., Mallén-Fullerton G., Brown T., 2003, ApJ, 582, 1123

Mao S., Paczynski B., 1991, ApJ, 374, 37

Marcy G., Butler P., 1993, BAAS, 25, 916

Marcy G., Butler P., 1995, BAAS, 27, 1379

Marcy G. W., Butler R. P., 1996, ApJ, 464, 147

Marcy G., Butler P., Williams E., Bildsten L., Graham J., Ghez A., Jernigan G., 1997, ApJ, 481, 926

Marcy G., Butler R., Vogt S., Liu M., 2001, ApJ, 555, 418

Marley M., Gelino C., Stephens D., 1999, ApJ, 513, 879

Matthews J., Kuschnig R., Shkolnik E., 2001, in ESA SP-464: SOHO 10/GONG 2000 Workshop: Helio- and Asteroseismology at the Dawn of the Millennium. p. 385

Mayor M., Queloz D., 1995, Nat, 378, 355

Mazeh T., Naef D., Torres G., Latham D., Mayor M., 2000, ApJ, 532, 55

McCaughrean M., O'dell C., 1996, AJ, 111, 1977

Milsom J. A., Burrows A., 2002, American Astronomical Society Meeting, 200

Mouillet D., Lagrange A.-M., Beuzit J.-L., Renaud N., 1997, Astronomy and Astrophysics, 324, 1083

Murray N., Hansen B., Holman M., Tremaine S., 1998, Sci, 279, 69

NASA, 2003, http://nssdc.gsfc.nasa.gov/planetary/factsheet/moonfact.html

Nelson A., Benz W., Adams F., D. A., 1992, ApJ, 502, 342

Nelson R., Papaloizou J., Masset F., Kley W., 2000, MNRAS, 318, 18

Papaloizou J., Terquem C., 1999, ApJ, 521, 823

Pepe F., Mayor M., Benz W., Bertaux J.-L., Sivan J.-P., Queloz D., Udry S., 2000, in Proceedings of the ESO Symposium - Antofagasta, Chile, 1-4 March 1999. p. 572

Pepe F., Mayor M., Galland F., Naef D., Queloz D., Santos N., Udry S., 2002, Astronomy and Astrophysics, 388, 632

Pollock J., 1984, ARA&A, 22, 389

Press W., B. F., Teukolsky S., Vetterling W., 1992, Numerical Recipes: The Art of Scientific Computing. Cambridge University Press, Cambridge

Queloz D., Eggenberger A., Mayor M., Perrier C., Beuzit J., 2000a, Astronomy and Astrophysics, 359, 13

Queloz D., Mayor M., Naef D., Santos N., Udry S., Burnet M., Confino B., 2000b, in Proceedings of the ESO Symposium - Antofagasta, Chile, 1-4 March 1999. p. 548

Rasio F., Ford E., 1996, Sci, 274, 954

Reuyl D., Holmberg E., 1943, ApJ, 97, 41

Roxburgh I., Christensen-Dalsgarrd J., Favata F., 2000, Technical Report, ESA

Safronov V., 1969, Evolution of the Protoplanetary Cloud and the Formation of Solar System. Nauka Press, Moscow

Sandquist E., Taam R., Lin D., Burkert A., 1998, ApJ, 506, L65

Sandquist E., Dokter J., Lin D., Mardling R., 2002, ApJ, 572, 1012

Santos N., Israelian G., Mayor M., 2000, Astronomy and Astrophysics, 363, 228

Santos N., Israelian G., Mayor M., 2001, Astronomy and Astrophysics, 373, 1019

Saumon D., Hubbard W., Burrows A., Guillot T., 1996a, ApJ, 460, 993

Saumon D., Marley M., Guillot T., Freedman R., 1996, BAAS, 28, 1114

Schneider J., 2003, http://cfa-www.harvard.edu/planets

Seager S., Sasselov D., 1998, ApJ, 502, 157

Seager S., Whitney A., Sasselov D., 2000, ApJ, 540, 504

Showman P., Guillot T., 2002, Astronomy and Astrophysics, 385, 166

Shu F., Adams F., Lizano S., 1987, ARA&A, 25, 23

Smith B. A., Terrile R. J., 1984, Sci, 226, 1421

Sobolev V. V., 1975, Light scattering in planetary atmospheres. Oxford and New York, Pergamon Press (International Series of Monographs in Natural Philosophy. Volume 76)

Strand K. A., 1943, PASPC, 55, 28

Street R. et al., 2003, in Scientific Frontiers in Research on Extrasolar Planets. ASP Conference Series, 294, p. 405

Sudarsky D., Burrows A., Hubeny I., 2003, ApJ, 588, 1121

Sudarsky D., Burrows A., Pinto P., 2000, ApJ, 538, 885

Tamura M., Suto H., Murakawa K., Hayashi S., Kaifu N., Itoh Y., 2001, American Astronomical Society Meeting, 198

Tinney C., Butler R., Marcy G., Jones H., Penny A., Vogt S., 2001, ApJ, 551, 507

Trilling D., Lunine J., Benz W., 2002, Astronomy and Astrophysics, 394, 241

Trilling D., Benz W., Guillot T., Lunine J., Hubbard W., Burrows A., 1998, ApJ, 500, 428

Trilling D., Koerner D., Ftaclas C., Brown R., Donovan J., 2001, American Astronomical Society Meeting, 199

Udry S., Mayor M., Naef D., Pepe F., Queloz D., Santos N., 2000, Astronomy and Astrophysics, 356, 590

van de Kamp P., 1969, AJ, 74, 757

van de Kamp P., 1982, Vistas in Astronomy, 26, 141

Walsh D., Carswell R., Weymann R., 1979, Nat, 279, 381

Ward W., Hourigan K., 1989, ApJ, 347, 490

Ward W., 1997, ApJ, 482, L211

Wetherill G., 1990, Ann Rev Earth Planet Sci, 18, 205

Wolszczan A., Frail D., 1992, Nat, 355, 145

Zucker S., Mazeh T., 2002, ApJ, 568, L113

APPENDIX A

System parameters for six known Pegasi planets

Stellar parameters for six bright stars known to harbour close-orbiting Pegasi planets are detailed at Table A.1. Radial velocity measurements of the stellar host allow us to calculate the orbital distance, period and minimum mass of the planet. The results of these calculations, as described in Chapter 2.1.1, are detailed at Table A.2 alongside theoretical estimates for the effective temperature and evolutionary radius (upper limit) of the planet, as determined in Chapter 3.2.2.

Star	Spectral Type	m_V (Mags)	$T_{\rm Eff}$ (K)	P_{rot} (Days)	$v \sin i$ (km s^{-1})	[Fe/H]	Age (Gyrs)	$M_*/M_\odot$	$R_*/R_\odot$
υ And	F8V [1]	4.09	6107±80 [4]	12.2±2 [6]	9.3±0.4 [4]	0.09±0.06 [4]	3.8±1.0 [4]	1.27±0.06 [14]	1.67±0.06 [14]
τ Boo	F7V [1]	4.50	6360±80 [4]	3.3±0.1 [7]	14.8±0.3 [4]	0.27±0.08 [4]	1.0±0.6 [4]	1.37±0.05 [14]	1.46±0.06 [14]
51 Peg	G2V [1]	5.46	5793±70 [4]	29±7 [6]	2.1±0.7 [4]	0.20±0.07 [4]	4.0±2.5 [4]	1.10±0.06 [14]	1.20±0.07 [14]
HD 179949	F8V [2]	6.25	6115±50 [5]	9±2 [8]	6.3±0.9 [9]	0.22±0.07 [11]	3.5±2.5 [13]	1.24±0.10 [14]	1.24±0.10 [14]
HD 75289	G0V [3]	6.35	6000±50 [3]	16±3 [8]	4.4±1.0 [10]	0.29±0.08 [12]	5.6±1.0 [12]	1.22±0.05 [14]	1.25±0.05 [14]
HD 209458	F9V [1]	7.65	6000±50 [8]	16.5±3 [18]	3.7±1.3 [17]	0.00±0.07 [15]	5.7±1.0 [16]	1.10±0.10 [15]	1.20±0.10 [15]

Table A.1: Stellar parameters for bright stars known to harbour Pegasi planets. [1] Gray, Napier & Winkler (2001), [2] Houk & Smith-Moore (1988), [3] Gratton, Focardi & Bandiera (1989), [4]Fuhrmann, Pfeiffer & Bernkopf (1998), [5] Gray (1992), [6] Henry et al. (2000a), [7] Synchronised rotation assumed from Baliunas et al. (1997); Henry et al. (2000a), [8] Mazeh et al. (2000), [9] Groot, Piters & van Paradijs (1996), [10] Benz & Mayor (1984), [11] Tinney et al. (2001), [12] Udry et al. (2000), [13] Estimate based on spectral type [14] Average of Spectroscopic studies by Fuhrmann, Pfeiffer & Bernkopf (1997); Fuhrmann, Pfeiffer & Bernkopf (1998); Gonzalez (1998); Gonzalez & Laws (2000); Gonzalez et al. (2001) [15] Estimated from Tinney et al. (2001); Udry et al. (2000), [16] Cody & Sasselov (2002) [17] Queloz et al. (2000a), [18] Average from Barnes (2001); Queloz et al. (2000a)

Planet	K_* (m s^{-1})	P_{orb} (Days)	Orbital Radius (AU)	M_p/M_{Jup} sin i	$T_{\rm Eff}$ (K)	R_p/R_{Jup} Hot model	R_p/R_{Jup} Cold Model
υ And b	74.5±2.3 [1]	4.6171±0.0001 [1]	0.0588±0.0020	0.716±0.053	1570	1.49	1.32
τ Boo b	469±5 [2]	3.3125±0.0002 [1]	0.0483±0.0018	4.242±0.224	1680	1.37	1.16
51 Peg b	56±1 [3]	4.2306±0.0005 [3]	0.0528±0.0029	0.475±0.038	1330	1.53	1.48
HD 179949 b	102±3 [4]	3.0930±0.0001 [4]	0.0446±0.0036	0.838±0.109	1550	1.40	1.31
HD 75289 b	54±1 [5]	3.5098±0.0007 [5]	0.0483±0.0020	0.461±0.028	1470	1.58	1.70
HD 209458 b	81±6 [6]	3.5239±0.0001 [6]	0.0470±0.0018	0.620±0.050	1460	1.38	1.36

Table A.2: System parameters for known Pegasi planets around bright stars. [1] Private Communication - Geoff Marcy, [2] Butler et al. (1997), [3] Mayor & Queloz (1995); Marcy et al. (1997), [4] Tinney et al. (2001), [5] Udry et al. (2000), [6] Henry et al. (2000b). The results in columns 4 and 5 are calculated from stellar and planetary parameters using the equations detailed in Chapter 2.1.1. Effective planetary temperature and radius estimates are given for the estimated age of the system, assuming an edge-on inclination $i = 90$ (i.e. upper limit).